Computer Simulation of Complex Fluids using Dissipative Particle Dynamics

Simon Ian Jury

A thesis submitted in fulfilment of the requirements
for the degree of Doctor of Philosophy
to the
University of Edinburgh
1999

Abstract

A parallel code has been developed to implement the Dissipative Particle Dynamics (DPD) simulation algorithm. DPD is a particle based method which simulates the fluid at a mesoscopic scale. Since the DPD interactions are both soft (compared to the potentials used in molecular dynamics) and momentum conserving, DPD offers the possibility of reproducing hydrodynamic behaviour at large length and time scales. Other techniques for hydrodynamic flow simulation are reviewed before the DPD algorithm is presented together with some of the coding issues arising from using a parallel implementation.

Equilibrium thermodynamics, as pertaining to phase separation, is presented, together with the scaling arguments used to derive growth laws for domain size. An in depth study of domain size scaling in three dimensional binary fluid phase separation has been completed. For an appropriate choice of parameters, domain growth is shown to enter a regime dominated by capillary and viscous forces. Qualitative analysis of interface maps and velocity fields reveal the Siggia mechanism for domain coarsening in operation. By performing simulations over two orders of magnitude in reduced length and reduced time units, a small yet significant breakdown of scaling is observed in the domain growth rate. Possible explanations for this breakdown are considered.

By extending the code, we study a dense solution of an amphiphilic species focusing on the smectic mesophase. Results are presented for the formation of monodomain, bidomain and polydomain lamellar phases. Shearing is performed, using Lees Edwards boundary conditions, the effect of shear on the lamellar phase is examined. It is shown how, for certain concentrations and shear rates, a lamellar structure will tend to fold in upon itself, this is a possible first stage in onion formation.

Declaration

This thesis has been composed by myself and it has not been submitted in any previous application for a degree. The work reported within was executed by me, unless otherwise stated.

Simon Ian Jury

Parts of this thesis appear in:

[1] *Tests of Dynamical Scaling in 3-D Spinodal Decomposition.* Phys. Rev. E. volume **59**, page R2535 (1999).

[2]*Simulation of amphiphilic mesophases using dissipative particle dynamics.* P.C.C.P., volume **1**, no. 9 (1999).

Contents

Chapter 1

Introduction

A complex fluid, at base level, is an ordinary fluid with something in it. In this chapter this definition will be extended and clarified; attention is focused on phase separating fluids and surfactant solutions. A review is undertaken of the state of the art in simulating complex fluids. The chapter concludes with a description of the Dissipative Particle Dynamics simulation technique, and a discussion on temperature convergence and compressibility of the DPD fluid.

1.1 Complex and Simple Fluids

Let's first decide what is meant by a simple fluid. Consider water, a typical fluid in many ways its properties are well documented and, for the most part, well understood. Water has a freezing point, below which it becomes a hard crystalline solid which retains its shape indefinitely; above the freezing point water is a low viscosity fluid which will flow to mould itself to the shape of the containing vessel. This simple behaviour marks water out to be a classical fluid. Many substances are not so well-behaved, mayonnaise or ice cream, for example exhibit liquid-like and solid like properties: they have a *yield stress*, which means they are solid below a certain stress and become liquid-like above that stress.

This sort of non-simple behaviour is typical of complex fluids.

Other examples include nail polish, which must be thick enough to cling to the bristles of the applicator, yet fluid enough to form a glassy smooth surface on finger nails. Thermotropic liquid crystals, used in the manufacture of computer displays are another example, they are composed of small semi-rigid molecules that are elliptical in shape and spontaneously orient, forming anisotropic fluids. Even blood is a complex fluid, red blood cells orient themselves in a manner dependent on the rate at which the blood is flowing, the result is a fluid whose viscosity decreases with increasing shear rate, a phenomenon seen in many colloidal systems and known as *shear thinning.*

All these examples share a common feature: the bulk properties of the fluid are defined by the behaviour of smaller bodies suspended within the bulk. Perhaps a better definition of complex fluid is, a fluid whose macroscopic properties are controlled by mesoscale physics within the fluid. In many cases, the mesoscale dependency enters through the behaviour of bodies within the fluid. For example, colloidal suspensions and polymer solutions both contain mesoscale objects; the properties of these objects (volume fraction, charge, size distribution etc...) are responsible for the bulk characteristics of the entire fluid [3].

For the purposes of the present work two types of complex fluid will be considered, binary solutions and surfactant solutions.

In a homogeneous binary solution, a phase transition may be induced, into a separated state, upon lowering the temperature. As part of the separation process a network of interlocking domains is formed. Separation proceeds, and the network coarsens via the flow-induced topological disconnection and reconnection of these domains. Within the domains, viscous, inertial and capillary forces interact in a non-trivial way to determine the rate at which the separation will occur. Analysis of domain structure and growth, in phase separating binary systems, clarifies the relationship between the fundamental forces operating in complex fluids.

Surfactant molecule are amphiphilic; that is, they consist of a *hydrophilic* (water loving) group joined to a *hydrophobic* (water hating) group. Typically, the hydrophobic (or tail) group is a hydrocarbon chain of length $8-20$ carbon atoms, the hydrophilic (or head) group is often ionic. In solution, tails tend to group together to minimize their exposure to water, figure 1.1 shows a schematic view of surfactant packing in the lamellar phase .

Thus, amphiphiles *self-assemble* into aggregates such as spheroidal and worm-like micelles, vesicles and bilayers. At high concentrations, such aggregates can form ordered phases of nematic, hexagonal, cubic or other symmetry [4,5]; in all cases, the driving force behind the packing is to minimise the exposure of tail groups to water. Amphiphiles are not only of great interest scientifically, but are of immense practical value as detergents, emulsifiers, encapsulants, lubricants and so on. Surfactants are *polymorphic*; that is, they form many different structures depending on concentration, temperature, salinity and external flow. This gives a rich and diverse phase behaviour which one would like to be able to predict; it also offers the possibility for more exotic structures to be formed in the presence of an external flow.

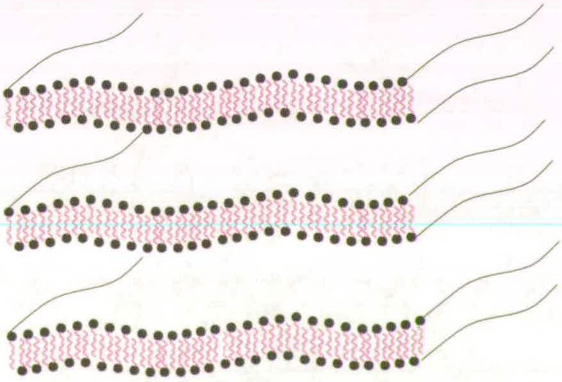

Figure 1.1: Surfactant packing in the lamellar phase.

The remainder of this chapter looks at the main simulation techniques used to examine the behaviour of binary fluids and surfactant solutions. A large section is devoted to explaining the Dissipative Particle Dynamics simulation technique which will be employed in the studies which comprise the rest of the thesis. Chapter 2 looks at how the DPD algorithm is implemented on a massively parallel computing platform.

Chapter 3 contains a review of equilibrium thermodynamics as applied to phase separation in binary fluids, specifically a Landau free energy approach is used to derive the thermodynamic *equations of motion* which drive the separation. In the second half of Chapter 3, scaling arguments are applied to domain coarsening. It is shown that three growth laws are, in principle possible; which one is seen is dependent upon the terms in the relevant dynamical equation (Navier-Stokes plus a term coupling the chemical potential and velocity fields) which are dominant. Approximate forms for the structure factor $S(\mathbf{k})$ are presented.

Building upon Chapter 3, Chapter 4 comprises a qualitative look at the dynamics of the separation through analysis of interface and velocity maps. Domain coarsening is contingent upon the topological breaking and reconnecting of domains; careful examination of velocity maps clearly show Siggia's *necking down* mechanism operating in the pinch-off process.

In Chapter 5, a detailed numerical examination of the coarsening rates is made. By extracting a lengthscale from the first moment of $S(\mathbf{k})$, the rate of domain coarsening can be measured. This coarsening rate is compared to the predictions, based on scaling arguments, made in Chapter 3. A small, yet significant deviation from the scaling predictions is seen; this manifests itself as a systematic drift in the coarsening rate, with changing viscosity.

Chapter 6 is devoted to surfactants. Results are presented for the phase diagram of a DPD dimer[1] (perhaps the simplest model of a surfactant within the DPD framework). Plotted with temperature against concentration, the boundaries between three distinct phases are identified. Introducing a shear flow into the simulation, further examinations are made on the effect of shear-rate on

---

[1] The phase diagram work was carried out by Maarten Hagen in collaboration with the present author.

monodomain, bi-domain and poly-domain lamellar phases. A tendency for the lamellar structure to fold in upon itself is identified and the effect of a shear flow on the position of the lamellar-isotropic phase boundary is examined.

1.2 Simulation Methodologies

Many of the interesting properties of complex fluids arise due to *hydrodynamic* interactions. The presence of hydrodynamic interactions is a manifestation of momentum conservation. Consider a solid particle moving through a fluid, as it moves it is slowed down by the effects of viscosity; as it slows, momentum is transferred into the surrounding fluid, this momentum will spread into the fluid. This spread of momentum may be described as a field diffusing away from the moving body, this field will affect the motion of any further body which it passes. The strength of these hydrodynamic flow fields decreases slowly with distance, typically the associated force will decay as $\sim 1/r$, so they cannot be ignored. The domains formed in phase separation and the structures formed by concentrated surfactant solutions are heavily influenced by hydrodynamic interactions.

Correctly modelling the hydrodynamics is crucial to observing correct flow behaviour; this rules out any simulation technique which does not conserve momentum. Also ruled out are techniques which cannot study flow dynamically such as Monte-Carlo methods.

1.2.1 Integration of the Cahn-Hilliard equation

For a phase separating binary fluid, an equation may be written down that describes the time evolution of the concentration field. This is the Cahn Hilliard equation, it will be discussed at length in Chapter 3.

Some authors have looked at phase separation by direct numerical integration of the Cahn Hilliard equation. For example, Ref. [6] has studied phase separation in two dimensions in the presence of a concentration dependent glass transition. Some interesting results emerge for the coarsening dynamics of droplets of liquid phase caught in the glass phase, in these circumstances the behaviour of the liquid drops is quite different from that seen in usual two fluid separations. Ref. [7] applied the same method to look at simple two fluid phase separation in three dimensions. Some interesting early time diffusive behaviour, was observed; however a hydrodynamic regime was not accessed due to system size constraints.

Many authors [8–12] have used essentially the same model under the guise of a Langevin equation. Again, there has been good progress made in two dimensions, but little in the three dimensional case. The problem of small system size is the main limiting factor to simulations of this kind; to ensure stability in the integration scheme, small time steps and a small grid size are needed, thus only the small scale, early times regimes have been accessed.

1.2.2 Lattice Gas Automaton

In the Lattice Gas Automaton method (L.G.A.), point-particles move between discrete lattice nodes, each particle has a discrete velocity which points between nearest neighbour nodes. There are two steps to the algorithm, a collision step whereby all particles arriving at the same node collide and move away with a velocity given by a pre-ordained set of collision rules, and a propagation step in which the particles move freely along the links. The simulator is free to choose any set of collision rules as long as mass and momentum conservation are satisfied.

Two phase flows are introduced via boolean variables $r_i(\mathbf{x})$ and $b_i(\mathbf{x})$, which take the value 1 or 0 depending on whether a particle, which can be one of two types (red or blue), is present at $\mathbf{x}$ with velocity $\mathbf{c}_i$. Collisions proceed as before with the added restriction that the total number of red and blue particles is conserved. An additional step is performed, wherein the results of the collision step are altered to induce a surface tension by creating a repulsion between red and blue type particles. A full description of the three dimensional lattice gas model is given in [13].

Such simulations are extremely fast due to the simplicity of the collision rules, there is evidence that hydrodynamic domain growth has been seen in three dimensional phase separation [14][2] A two dimensional study of phase separation, using a similar model as in three dimensions, has shown excellent agreement with both theory and experiment [15].

Lattice gas methods have been extended to model surfactants [16] in oil/water mixtures; the surfactant molecules are characterised by a dipole vector. In 2 dimensions the model exhibits the commonly formed equilibrium microemulsion phases including droplets and lamellae, as well as verifying the existence of a shear induced isotropic to lamellar phase transition [17]. The same model was used to study the kinetics of droplet self-assembly [18]; it was found that the presence of amphiphilic molecules affects the self-assembly kinetics very dramatically.

1.2.3 Lattice Boltzmann

Here, the point-particles of LGA are replaced with average distribution functions (f_i), similar to the molecular distribution functions used in kinetic theory [19]. Each f_i is associated with a lattice vector $\mathbf{e}_i$, rather than a lattice node as in LGA. The evolution equation for a given f_i takes the form,

$$f_i(\mathbf{x} + \mathbf{e}_i \Delta t, t + \Delta t) - f_i(\mathbf{x}, t) = -\Omega_i^c (f_i - f_i^0) \tag{1.1}$$

where Δt is the time step and Ω_i^c is a collision operator. Here f_i^0 is an equilibrium distribution function, the choice of which determines what kind of system is being simulated.

---

[2] In this work, growth is clearly being influenced by hydrodynamic forces, however finite size cutoff precludes any firm conclusions being drawn, regarding the nature of the hydrodynamic regime accessed.

Lattice Boltzmann schemes are easily extended to include multi-component flows and have been applied to both two and three dimensions. A preliminary investigation of the two dimensional model [20], verified the model's stability and reproduced the predicted values of surface tension. An extensive study of phase separation in two dimensions [21–24] quickly followed. It has revealed an interesting breakdown in traditional scaling ideas during phase separation; under certain circumstances domains of a single fluid may become *trapped* within larger domains. When this happens, the usual hydrodynamic modes of fluid transport cease to operate, the trapped domain may only escape through the much slower process of diffusion. Such ideas had not been seen in any of previous analysis using LGA or Cahn Hilliard integration. Preliminary results for separation in a shear flow, are also in press [22].

In three dimensions, hydrodynamic effects in phase separation have been conclusively seen [25, 26]. Only in recent work has a thorough study been attempted, preliminary results are encouraging both in the quality of the data and the scope of lengths and times explored. [26, 27]

Despite its undoubted success in studying phase separation, there are shortcomings with the Lattice Boltzmann technique. As with all lattice based methods, isotropy is a major problem, directions along lattice vectors are favoured. For systems with interfaces, the interfaces may line up along the lattice vectors. Empirical evidence suggest that to prevent this occurring, at the expense of relaxing apparent efficiency of LB schemes, having an interface about three times larger than the lattice size is sufficient [26]. Careful choice of lattice connections will reproduce isotropic hydrodynamics; however so far, no one has been able to reproduce isotropic thermodynamics. Incorporating new model features, such as surfactants, colloids or polymers into the LB scheme is not easy. A LB scheme for studying surfactant solutions has provided good results for the emulsification of oil and water after a quench, so far this work has been limited to 2 dimensions [28].

1.2.4 Boundary Integral Methods

For systems in which the interesting physics enters through the motion of interfaces alone, boundary integral methods may significantly reduce computational costs. Implementation is possible whenever the flow is governed by a linear equation for which the Greens function is known. This is the case for flows in which inertial effects are ignored (highly viscous or Stokes flow) and also for flows in which viscous effects are ignored (inviscid flows).

One is relieved from having to incorporate the coupling of interior flow and interface motion, both highly nontrivial problems in themselves. Instead, dynamical equations are set up and numerically integrated for the position and velocity of the interface, thus drastically reducing the number of variables to be monitored [29]. Many studies have been carried out using boundary integral methods to look at drop deformation and breakup in the case of highly viscous fluid in an extensional flow field. The studies reveal an excellent agreement with experiment [30].

Since the physics of phase separation involves both viscous and inertial forces, the applicability of this method to the problem of domain growth is limited. Problems also arise when domains reach pinchoff, how to incorporate a topological disconnection is not obvious. So far a study of phase separation using boundary integral methods has not been attempted.

1.2.5 Molecular Dynamics

In this approach individual fluid particles are modelled as discrete elements within the simulation. For a simple system containing N particles, the potential energy may be divided into terms involving single molecules, pairs, triplets etc,

$$V = \sum_i v_1(\mathbf{r}_i) + \sum_i \sum_{j>i} v_2(\mathbf{r}_i, \mathbf{r}_j) + \sum_i \sum_{j>i} \sum_{k>j>i} v_3(\mathbf{r}_i, \mathbf{r}_j, \mathbf{r}_k) + \dots \tag{1.2}$$

this potential may be used to derive the force acting on a particle at a given time. Evaluating every term in a sum over particle triplets is a *very* time consuming business, however it has been shown that for real molecules at typical fluid densities the v_3 term is significant [31]. To circumvent this problem, an *effective* pairwise potential is used, which includes an approximation to the three body interaction. The forces generated are summed to give the total force acting on a single particle at a given time which is, in turn, integrated to give a new velocity and position. The potential commonly used is the Lennard-Jones 12-6 potential,

$$v^{LJ} = 4\epsilon\left[\left(\frac{\sigma}{r}\right)^{12} - \left(\frac{\sigma}{r}\right)^{6}\right] \tag{1.3}$$

which provides a reasonable description of the properties of argon via simulation, if the parameters ϵ which represents an energy and σ which sets the lengthscale are chosen appropriately.

In two dimensions, MD simulations of phase separation have successfully reproduced scaling and growth exponents for critical and off critical quenches [32]. In three dimensions, two groups have presented results, in one case [33], finite size effects become evident before hydrodynamic behaviour is seen, the other case [34] claims to see hydrodynamic behaviour. Results from [34] are discussed in Chapter 5.

Molecular dynamics provides a reliable and accurate method of simulating fluids, it does however suffer from a few drawbacks. Using a molecular dynamics algorithm current supercomputers can probe lengthscales $\sim 10^{-8}$m and timescales of a few nano-seconds; this is many orders of magnitude short of the length and time scales of interest in most complex fluids. So far molecular dynamics has only been really successful when looking at short scale, small time properties.

1.3 The DPD algorithm

DPD is a relatively new technique for simulating hydrodynamic behaviour at the mesoscopic level. In DPD, a set of particles in a continuum act as momentum carriers whose behaviour is governed by a set of stochastic differential equations [35].

Each particle interacts isotropically with other particles in its local environment with conservative, random and dissipative forces that conserve mass (i.e. particle number) and momentum. The emergence of isothermal Navier-Stokes hydrodynamics is thus guaranteed at large length and timescales. Note that momentum is exchanged in an isotropic and Galilean invariant fashion. Modification of the conservative forces that act between fluid particles allows many different meso-scale models to be defined at the thermodynamic level.

The set of stochastic differential equations describing particle motion are [36]

$$\frac{d\mathbf{r}_i}{dt} = \mathbf{p}_i, \quad \frac{d\mathbf{p}_i}{dt} = \sum_{ij} \Omega_{ij}\hat{\mathbf{r}}_{ij} \tag{1.4}$$

where the sum runs over all pairs of particles. The quantity Ω, which can be viewed as a force, is given by

$$\Omega_{ij} = w(r_{ij})\left(\alpha_{ij} + \sigma\theta_{ij} - w(r_{ij})\gamma(\mathbf{v}_{ij}\cdot\hat{\mathbf{r}}_{ij})\right) \tag{1.5}$$

The particle separation vector is denoted by $\mathbf{r}_{ij} = \mathbf{r}_i - \mathbf{r}_j$, $r_{ij} = |\mathbf{r}_{ij}|$, $\hat{\mathbf{r}}_{ij} = \mathbf{r}_{ij}/r_{ij}$, with the relative velocity $\mathbf{v}_{ij}$ defined similarly. Dissipation is controlled by the value of γ; a higher γ means an increased dissipation. Here $w(r)$ is a weight function chosen to be [35]

$$w(r) = \begin{cases} \alpha_{ij}(1 - r/r_c) & (r < r_c) \\ 0 & (r \geq r_c) \end{cases} \tag{1.6}$$

where r_c is a cutoff distance, which defines the DPD unit of length. The first term in Ω acts as a conservative force, with maximum repulsion given by α_{ij}, which may be different for different pairs of particles. The second term corresponds to a random force acting between pairs of particles, with properties

$$\langle\theta_{ij}(t)\rangle = 0, \quad \langle\theta_{ij}(t)\theta_{kl}(t')\rangle = (\delta_{ij}\delta_{kl} + \delta_{il}\delta_{jk})\delta(t - t'). \tag{1.7}$$

σ controls the amount of energy input to the system. The term involving γ describes a dissipative force that acts to decrease the relative velocity of the two particles. The random and dissipative forces act to drive the system towards an equilibrium state, with a temperature defined by

$$\sigma^2 = 2\gamma k_B T. \tag{1.8}$$

The stationary distribution of DPD, $f(\mathbf{r}_i, \mathbf{v}_i)$ is the canonical ensemble

$$f(\mathbf{r}_i, \mathbf{v}_i) \propto \exp\left(-H/k_B T\right) \tag{1.9}$$

$$H = \sum_i \frac{\mathbf{p}_i^2}{2m_i} + \sum_{ij} U(r_{ij}) \tag{1.10}$$

where $U(r)$ is the pair potential that generates the conservative forces. The function $f(\mathbf{r}_i, \mathbf{v}_i)$ is the probability density and representrs the probability of finding a particle at position $\mathbf{r}_i$ with velocity $\mathbf{v}_i$, k_B is the Boltzmann constant..

The formulation of DPD in this manner allows any thermodynamic model, defined via the conservative forces, to be simulated with the correct canonical distribution. However, a key advantage of DPD over molecular dynamics techniques which simulate the canonical ensemble is that the viscosity, and hence the hydrodynamics, can be varied *independently* of the thermodynamics. An estimate of the shear viscosity is [37],

$$\eta = \frac{\gamma n^2}{30} \int r^2 \omega(r)^2 dr + \frac{3mk_B T}{2\gamma} \left(\int \omega(r)^2 dr \right)^{-1} \tag{1.11}$$

where n is the number density of particles. Note, this estimate ignores contributions to η from the conservative forces, as such it must be treated as an approximation. Altering γ, while keeping the thermodynamic parameters fixed, increases the relative importance of the dissipative contribution to the viscosity (the first term in equation (1.11)). For the parameters used in this thesis, the kinetic term (second term in equation (1.11)) is swamped by the dissipative term, and the viscosity is entirely controlled by changes in the value of γ. The thermodynamics, determined by the conservative forces are unaffected, provided constant temperature is maintained.

Multiphase flows may be modelled by allowing α to vary depending on the type (type A or type B) of particles in the interaction. For two fluid phase separation, where the types of fluid are thermodynamically symmetric, $\alpha_{AB} > \alpha_{AA} = \alpha_{BB}$ [38]. In two dimensions, the two component DPD model has been successful in reproducing the correct growth laws for domain coarsening [39, 40]. In the same work a bubble of a single phase inside a solution of a second phase was used to verify the existence of a Laplace pressure and surface tension.

Other uses of the DPD method include colloidal suspensions. By sharing the momentum of a group of DPD particles equally among themselves, these particles will remain at fixed relative separation. If the group is initialised as a sphere, this forms a simple model of a colloid [41–43].

1.3.1 Validation

Various parameters may be calculated to check the integrity of a DPD code. Firstly, equation (1.8) provides an expression for the theoretical value of the temperature in the limit of continuous time. For almost all of the work presented here, the integration of the force, equation (1.5), is carried out by a simple Euler scheme;

$$\mathbf{v}_i(t+\delta t) = \mathbf{v}_i(t) + \frac{\delta t}{m}\mathbf{f}_i(t) \tag{1.12}$$

$$\mathbf{r}_i(t+\delta t) = \mathbf{r}_i(t) + \frac{\delta t^2}{2m}\mathbf{f}_i(t) \tag{1.13}$$

where m is the particle mass. At each timestep the Euler scheme will introduce an error $\mathcal{O}(\delta t^2)$ into the velocities [44]. This error will manifest in the actual value of the temperature, as measured from the kinetic energy of the particles, differing from that given by equation (1.8). Figure 1.2 shows the variation of temperature with the dissipative coefficient γ for two values of the timestep.

These simulations were performed on a small system: $N = 1000$, $\rho = 3$ and $\sigma = 15$.[3] For these parameters, the algorithm becomes unstable at large γ for $\delta t = 0.1$, for $\delta t = 0.01$ the algorithm remains stable and the measured temperature is always within 2% of the theoretical value. A timestep of 0.01 was used in the remainder of this work (unless explicitly stated otherwise). Errors in k_BT were routinely monitored as a consistency check.

---

[3] The units of density are defined from the mass of a single particle, which is set to one and the lengthscale set by the interparticle interaction r_c.

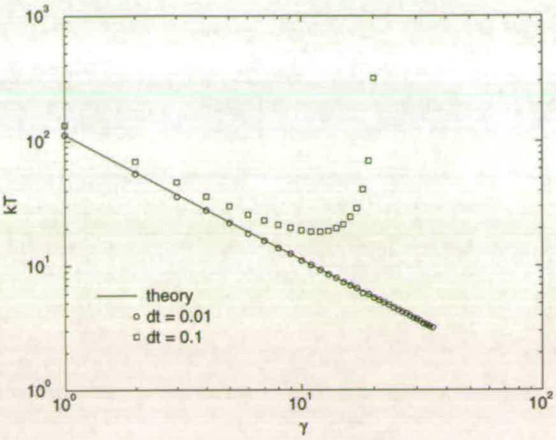

Figure 1.2: Temperature variation against the dissipative coefficient γ. The fluctuation-dissipation theorem gives a theoretical value for k_BT, the kinetic energy gives the actual value measured in a simulation. Two timesteps have been used, for $\delta t = 0.1$ the algorithm becomes unstable at large γ, whilst $\delta t = 0.01$ gives good temperature convergence.

A second test was performed in which the density was varied and the pressure measured. Appendix B gives a mean field theory for the free energy of the DPD fluid, from this an expression for the pressure may be deduced since $P = -\partial F/\partial V = (\rho^2/N)(\partial F/\partial \rho)$:

$$\frac{F}{Nk_BT} = \ln\rho + \frac{N\alpha\pi}{30\rho} \tag{1.14}$$

$$\Rightarrow \quad P_T = \rho k_BT + \frac{\alpha\pi}{30}\rho^2. \tag{1.15}$$

The actual pressure of the fluid may be measured directly from the simulation as a combination of kinetic and interaction terms. The details of this calculation are given in [31], the result is,

$$P_A = \rho\langle k_BT\rangle + \frac{1}{V}\langle \mathcal{W}\rangle \tag{1.16}$$

the average is over uncorrelated equilibrium configurations. $\mathcal{W}$ is the *internal virial* defined by $\mathcal{W} = 1/3\sum_{i=1}^{N}\mathbf{r}_i\cdot\mathbf{f}_i$.

Figure (1.3) shows excellent agreement between theory and measurement, this is expected since the soft potentials used by DPD make the mean field theory a

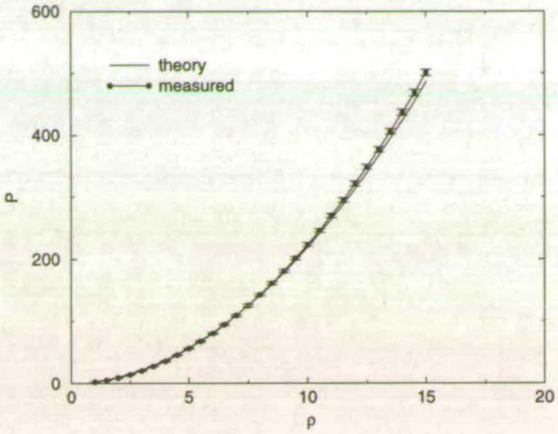

Figure 1.3: Pressure as a function of density. Units of r_c for length, δt for time and m for mass, define the units of pressure. Agreement between simulation and theory is extremely good.

good approximation. This graph gives increased confidence in both the accuracy of the code and the validity of the mean field treatment for free energy.

An important variable is the compressibility of the fluid. Most theoretical models are based on having an incompressible fluid; since the interactions in DPD (equation 1.5) are specifically designed to be *soft*, the compressibility of the DPD fluid could be relevant and should be tested. Isothermal compressibility κ_T is definied by, $\kappa_T \equiv -1/V(\partial V/\partial P)_T$, and represents the fractional change in volume for a given change of pressure at constant temperature. The derivative may be expressed as

$$\kappa_T = \frac{1}{\rho}\left(\frac{\partial \rho}{\partial P}\right)_T. \tag{1.17}$$

Using the mean field expression, equation (1.15), which relates pressure and density, the isothermal compressibility becomes

$$\kappa_T = \frac{1}{k_B T\rho + (\pi\alpha/15)\,\rho^2}.$$

Typical parameters for phase separation are $\rho = 10$, $k_B T = 1$ and $\alpha = 20$, for which $\kappa_T = 0.002$. This constitutes good evidence that the DPD fluid is incompressible[4].

---

[4] To model a binary fluid two values of α are used in the same simulation, depending upon the

Further evidence comes from considering the Mach number, Ma, defined as the ratio between the average flow velocity and the speed of sound within the fluid; $Ma = \langle v \rangle / c$. The speed of sound is related to the isothermal compressibility by $c = 1/(\rho \kappa_T)^{1/2}$, using this as an estimation for c gives $Ma^2 \sim 10^{-4}$ for the parameters quoted above. A condition for incompressibility is [45] $\mathrm{Ma}^2 < 1$, or at low Reynolds number $\mathrm{Ma}^2 \ll \mathrm{Re}$. These conditions may be derived by considering the variation of a local density about a mean density, such variations must be small for the fluid to remain incompressible. For the flows considered in this thesis the lowest Reynolds number is ~ 1, so both conditions are well satisfied, and the fluid is incompressible.

---

types of the particles in the interaction. When two like particles interact $\alpha = 20$, compared to the number of like particle interactions, the number of unlike particle interactions is negligible, therefore $\kappa_T = 0.002$ remains a reliable value in the two fluid case.

Chapter 2

Program Design

The results presented in this thesis would have been impossible to generate without the huge processing power and memory of modern parallel computers: a fact which is highlighted by the discussion of the finite size errors which arise in the scaling laws in late stage spinodal decomposition (see Chapter 5). The use of random numbers within DPD, combined with the added complexities arising from the presence of rigid dimers in a sheared geometry, made the design and coding a significant task. In this chapter, the solution to these problems is outlined.

2.1 Basic code structure and parallelisation

We start by considering the DPD code for quiescent binary fluids. Coding the DPD algorithm onto a serial machine is trivial, and many such codes exist. In writing the parallel code, an existing MD code provided the basic framework [1].

The code uses traditional spatial domain decomposition, wherein each processor in the parallel machine is allocated it own region of space. Particle information is stored on whichever processor is assigned to the region of space in which the

---

[1] The MD code was written by Sujata Krishna and Alan Simpson with the aim of studying colloidal systems.

particle finds itself. This processor calculates the force acting on all particles within its domain, then integrates this force to give the new set of positions and velocities. If the new position lies on a different processor, then particle information is passed to that processor. The code may be divided into the following steps:

- Specification of the domain decomposition. Each processor is assigned a rectangular subvolume of the simulation space, the dimensions of the subvolume are decided by the size of the simulation space and the number of processors being used.
- Generation of the initial positions and velocities. Positions and velocities are assigned at random, the velocities are then scaled such that the average r.m.s. velocity is equal to $\sqrt{3k_bT/m}$.
- Calculation of the forces. Pairwise forces are calculated from equation (1.5), linked lists are used to speed up the force calculation.
- Updating of the particle positions. Forces are integrated to give new velocities and positions. A simple Euler integration scheme is used, see equation (1.13).
- Calculation of desired observables and return to force calculation or continue. Certain quantities require an average over all particles, *e.g.* kinetic energy, pressure; for these quantities, the average is first performed on individual processors, this result is then passed to a single processor where a global sum takes place and the value is written to file.

At the beginning of each timestep, neighbouring processors exchange information about particles a distance r_c from their boundaries. This creates a halo around each processor, giving the processor enough information to perform the force calculation for all the particles within its domain. An extra complication arises due to the stochastic term in the DPD force calculation. In molecular dynamics, the forces F_{ij} and F_{ji} may be calculated on different processors, and since they depend only on position they will be guaranteed to be equal and opposite. This will not be the case with DPD since the random component will be different on the different processors. To overcome this difficulty a unique integer label is assigned to every particle, which we denote `particle-ident`, the interaction between particles `i` and `j` is only considered if `particle-ident(i)` is greater than `particle-ident(j)`. This is sufficient to ensure interactions are considered once on a single processor. The `particle-ident` label becomes a unique identifier which must remain with the particle at all times. An extra round of communication is required to pass the random forces back to the correct processor. The force calculation thus involves the following steps:

- Boundary-swapping of particle positions, velocities, particle-ident.
- Create link lists and calculate force.
- Boundary swapping of random force component.
- Addition of random force component to other components.

2.1.1 Outputs

In addition to the temperature and pressure, several local properties of the fluid are required for analysis. In both of the studies undertaken (phase separation and surfactant mesophases), much insight can be gained from direct visualisation of the relevant interface; for phase separation this is the interface between the phases, for surfactants it is the interface between surfactant and solvent. To facilitate such visualisations, an order parameter is defined on a regular grid in the fluid; see Appendix A for details on how to define suitable order parameters. Since the order parameter involves a sum over particles in the surrounding lattice box, it is essential that each box of the order parameter lattice does not straddle a processor boundary. The dimensions of the order parameter lattice are set by the user at compile time, prior knowledge of the domain decomposition is then necessary to ensure the order parameter lattice is initialised correctly. Although this appears cumbersome, it obviates the use of a further round of communication. In an identical fashion, the local velocity and local density, averaged over a lattice box, are also output; these may be further averaged over time [2].

Finally, the user may output the entire configuration (the complete set of particle positions, velocities, types, identifiers and partners) at regular intervals. This option is useful when simulations are performed without prior knowledge of the observables which will be of interest. It is also a safety precaution against machine failure since it allows runs to be restarted from the most recently saved configuration. A separate file is created for each processor, these files are then collated at the end of a run to give the entire configuration. The alternatives are each processor writing to the same file or every processor sending information to a single processor which then writes to a single file; both of these would greatly increase the run time.

2.2 Imposing Shear — Lees Edwards boundary conditions

Lees Edwards boundary conditions [46] are designed to create the flow field which occurs when a fluid is placed within a sliding plate or Couette shear cell. Since periodic boundary conditions are employed, the simulation space may be viewed as an infinity of repeating units. Only one of these units—the one in the centre—is monitored by the code, the others are identical periodic images of this central box.

Lees Edwards boundary conditions introduce shear by sliding the images directly

---

[2] In fact the random element to the DPD interaction means that averaging over time is essential to obtain a meaningful velocity field.

above and directly below the central box, at a constant velocity in opposite directions. Through the action of viscosity, this sliding motion will, over time, induce a velocity gradient within the central box. In the notation of figure 2.1, the simulation box and its images centred at $(x, y) = (\pm L, 0)$,$(\pm 2L, 0)$, etc. are taken to be stationary. Boxes in the layer above, $(x, y) = (0, L)$,$(\pm L, L)$,$(\pm 2L, L)$,etc. are moving at a speed $(dv_x/dr_y)\,L$ in the positive x direction. Boxes in the layer below, $(x, y) = (0, -L)$,$(\pm L, -L)$,$(\pm 2L, -L)$,etc. are moving at a speed $(dv_x/dr_y)\,L$ in the negative x direction. This will set up and maintain a steady linear velocity profile, with gradient dv_x/dr_y. Other methods do exist for introducing shear. Parrinello and Rahman [47], developed a method of altering the shape of the simulation box whilst maintaining a constant pressure. For a steady shear, this method has the adverse effect of making the box extremely long and

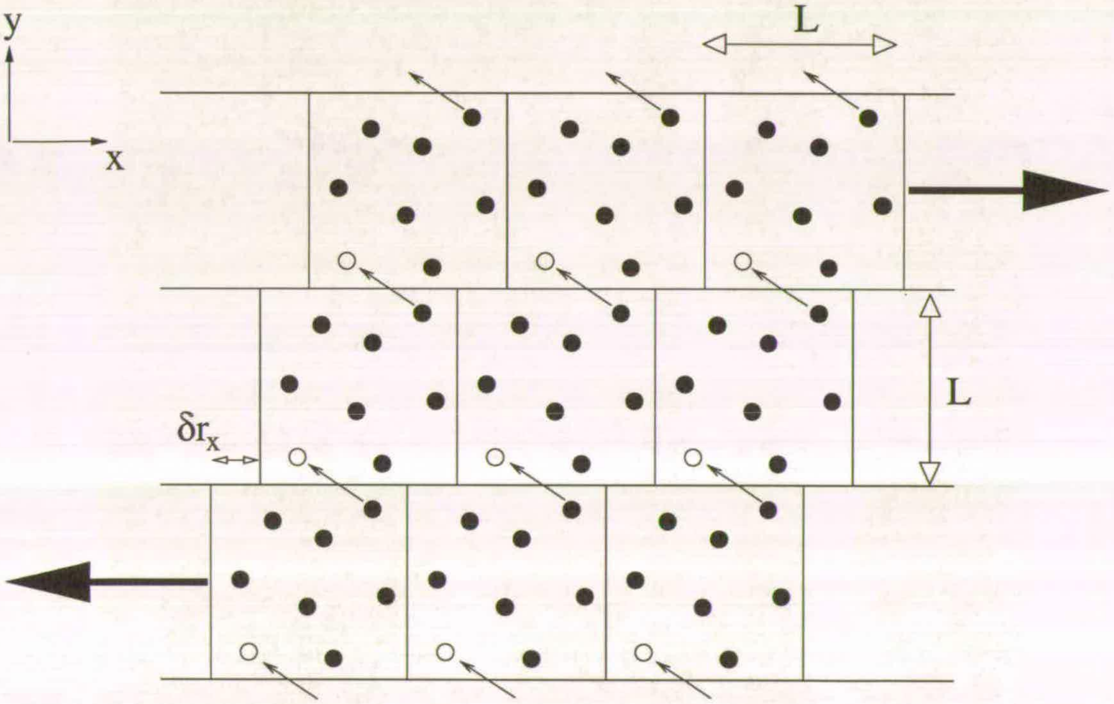

Figure 2.1: Two dimensional schematic of the Lees-Edwards sliding boundary conditions. The central row is kept stationary, whilst the rows above and below are given equal and opposite velocities. Through the transfer of particles between periodic images, a linear velocity gradient builds up within the central box. The strain on the central box is equal to δr_x

thin. Perhaps the simplest method is to add an extra component to v_x, the extra component being proportional to the particles' displacement in the y direction. However Lees Edwards has the advantage, in that it does not force the fluid to adopt the shear flow, rather it allows the fluid to respond to an external shearing force in a natural way.

2.2.1 Implementation

The first variation from the quiescent DPD code occurs during the boundary swapping between neighbouring processors, carried out before the force calculation. The velocity gradient exists in the y-direction and it is the x-component of velocity which is modified by the shear. Previously, boundary swapping in the y-direction occurred between one processor and the two fixed processors directly above and directly below in the processor map. In Lees-Edwards code, the processors are sliding over each other; a calculation is required to obtain the correct processors to communicate with. Note that this is only a problem for processors whose allocated subvolume contains the sheared boundaries; for such processors, boundary exchanges now involve communicating with two processors. Finding the correct processor to communicate with is a simple matter of adding or subtracting (depending on the direction in which the boundaries are being crossed) the total strain (δr_x) from a particle's position. The particle is then sent to the processor in charge of the subvolume containing the modified position.

After the force calculation, the random forces must be passed back to the correct processor. Once again, for processors on the sheared boundaries, the strain has to be removed before sending.

Debugging the communication routines can be difficult: if care is not taken, particles may be sent to the wrong processor; or particles may be sent to the right processor by two different routes, and be counted twice (Appendix D elaborates on these issues).

2.3 Code Validation

2.3.1 Compressibility

In Chapter 1 the compressibility of the DPD fluid was calculated, for the serial code, by measuring the rate of change of pressure with increasing density. In addition for the parallel code, a measure of compressibility was extracted directly from the momentum field. If a fluid is incompressible then $\nabla \cdot (\rho \mathbf{v}(\mathbf{r})) = 0$. Since the velocity we extract is averaged over a finite volume (see section 2.1.1) and this volume is constant, we may express the continuity equation in terms of the coarse grained momenta $\mathbf{p}(\mathbf{r})$: $\nabla . \mathbf{p}(\mathbf{r}) = 0$. In Fourier space this transforms to $\mathbf{k} \cdot \tilde{\mathbf{p}}(\mathbf{k}) = 0$, where $\tilde{\mathbf{p}}(\mathbf{k})$ is the Fourier transform of $\mathbf{p}(\mathbf{r})$. So, for an incompressible fluid, the radial component of $\tilde{\mathbf{p}}(\mathbf{k})$ will be zero. We have checked this for our simulations; figure 2.2 shows the transverse and radial components of $\tilde{\mathbf{p}}(\mathbf{k})$ together with the ratio for a time series which spans one of the large scale phase separation runs (for the parameters used, this data is taken from run p30 in the notation of Chapter 5).

Radial components are calculated from $\mathbf{k} \cdot \tilde{\mathbf{p}}(\mathbf{k})$, transverse components from $(\mathbf{k} \times \tilde{\mathbf{p}}(\mathbf{k}))$; both are normalised by dividing by $|\mathbf{k}||\mathbf{p}(\mathbf{k})|$. Due to the soft nature of the DPD interaction a non-zero value of the radial component is expected, continuity will only be recovered over lengthscales which incorporate many DPD interaction radii. This is exactly what figure 2.2 shows, as the lengthscale grows (moving from right to left in figure 2.2), the radial component of $\tilde{\mathbf{v}}(\mathbf{k})$ decreases; at the largest lengthscales the difference is approximately one order of magnitude.

2.3.2 Viscosity

Adding Lees Edwards boundary conditions to the code represents a substantial change, after implementation the code underwent a period of testing. Upon removal of the shear velocity, the temperature was converging to within 2% of

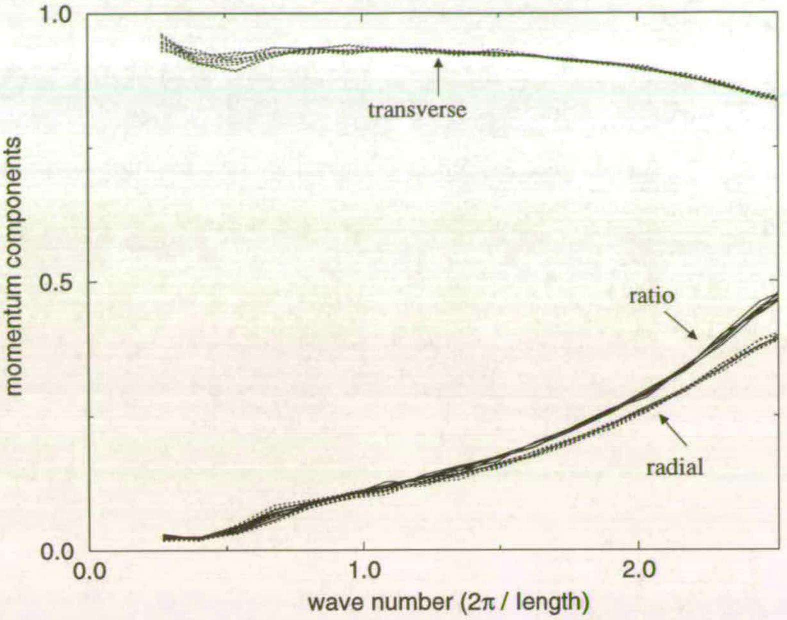

Figure 2.2: Test of the compressibility of the DPD fluid. The radial component of the k-space velocity field is consistently lower than the transverse component. This constitutes direct evidence that the velocity field has a low compressibility.

the nominal temperature set by fluctuation dissipation, equation (1.8). A more stringent test is to measure the viscosity η and compare this with both the equivalent measurement on the serial code and the theoretical prediction from equation (1.11). Shear viscosity η is related to the off diagonal elements of the pressure tensor $\mathcal{P}_{\alpha\beta}$ [31],

$$-\eta = \frac{\langle \mathcal{P}_{\alpha\beta} \rangle}{\dot{\gamma}} \tag{2.1}$$

here $\dot{\gamma}$ is the shear rate. Similar to section 1.3.1, $\mathcal{P}_{\alpha\beta}$ is calculated using the virial. A system size of $N = 10000$ with $\rho = 10$ and $kT = 1.0$ was used to generate figure 2.3 which shows agreement, to within statistical error, between the serial and parallel code. The theoretical predictions of Marsh [37, 48, 49], equation (1.11), are some way off, especially at low γ; this is thought to be a consequence of the high density used here, the work of Marsh assumes $\rho < 1$.

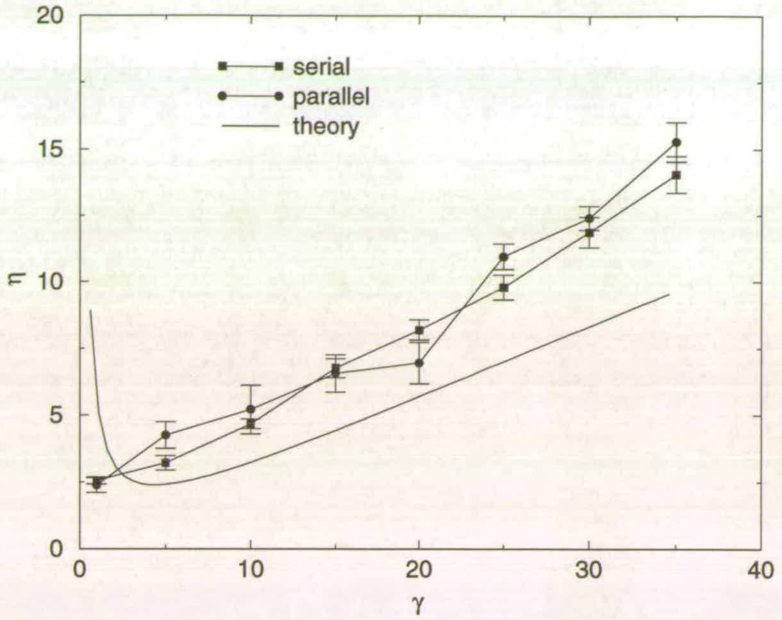

Figure 2.3: Theoretical value of η shows good agreement with both the serial and the parallel codes, this provides good evidence that the shear has been correctly implemented.

2.4 Model Surfactants

In an effort to reproduce the behaviour seen in real surfactant systems, a simple model of a surfactant was studied (the results are presented in Chapter 6). Each individual surfactant is formed from two DPD particles rigidly linked together at fixed separation. The conservative interaction between the particles is chosen to make one end of the surfactant more soluble than the other; such a model incorporates many of the important features of real surfactants. One of the advantages of the DPD technique over lattice based methods is revealed here; namely, the simplicity with which new model features may be added. The ease with which surfactants may be incorporated into an existing code is a prime example of the versatility of DPD.

Having decided upon dimers, the next question is how to impose the dimerization constraint. Given the soft forces, a natural idea is to use a soft constraint, such as a harmonic spring. However, for this work a rigid dimer model is used instead: the AB dimer consists of two DPD particles with a bond of fixed length connecting them. This length is chosen as $r_c/2$, r_c is the cutoff to the DPD interaction. Although somewhat arbitrary this makes the "size" of the dimer comparable to the interaction range which is appropriate to a model in which both the solvent and the surfactant are already coarse grained. The rigid dimer model avoids a specific difficulty that can otherwise arise in implementing a dimer model on parallel computers, namely that under some conditions (such as extreme flows) a soft constraint could in principle allow the two members of a dimer to become separated by a large distance in space. Because of the domain decomposition techniques used to partition particles among different processors according to their spatial location, it is much better if all interactions are of strictly finite range; a rigid linkage ensures this.

2.4.1 Calculation of the forces of constraint

The following treatment is an extension of the discussion to be found in reference [31]. For the case of two particles, joined by an inextensible rod, the equations of motion may be written as,

$$m_i \frac{d^2\mathbf{r}_i}{dt^2} = \mathbf{f}_i + \mathbf{g}_i \quad , \quad m_j \frac{d^2\mathbf{r}_j}{dt^2} = \mathbf{f}_j + \mathbf{g}_j \tag{2.2}$$

$\mathbf{f}_i$ is the usual force felt by particle i, due to the DPD interaction, $\mathbf{g}_i$ is an initially unknown constraint force, the only purpose of which is to keep the desired bond lengths constant. The force $\mathbf{g}_i$ is directed along the initial bond vector. Integrating (2.2) twice gives the positions of the dimers at the completion of a timestep,

$$\mathbf{r}_i^c(t+\delta t) = \mathbf{r}_i^u(t+\delta t) + \frac{\delta t^2}{m}\mathbf{g}_i(t) \tag{2.3}$$

$$\mathbf{r}_j^c(t+\delta t) = \mathbf{r}_j^u(t+\delta t) - \frac{\delta t^2}{m}\mathbf{g}_i(t) \tag{2.4}$$

where $\mathbf{r}_i^u$ would be the position of particle i in the absence of constraints and $\mathbf{r}_i^c$ is the constrained position.

The value of $\mathbf{g}(t)_i$ may be found by subtracting (2.4) from (2.3), squaring the result gives

$$\left[\mathbf{r}^c_{ij}(t+\delta t)\right]^2 = \left[\mathbf{r}^u_{ij}(t+\delta t)\right]^2 + 2\left[\frac{\delta t^2}{m}\mathbf{g}_i(t)\right]\cdot\mathbf{r}^u_{ij}(t+\delta t) + \left[\frac{\delta t^2}{m}\mathbf{g}_i(t)\right]^2 . \quad (2.5)$$

For the constraints to work the left hand side must be equal to the square of the dimer length. Equation (2.5) is a quadratic equation for $[(\delta t^2/m)\,\mathbf{g}_i(t)]$, it may be solved to give $\mathbf{g}_i(t)$.

After the correct positions have been found, the velocities need to be re-calculated to ensure there is no relative motion of the dimer ends along the bond vector. This is achieved by altering the velocities according to,

$$\mathbf{v}^c_i(t+\delta t) = \mathbf{v}^u_i(t+\delta t) - \frac{1}{2}\left[\mathbf{v}^u_{ij}(t+\delta t)\cdot\mathbf{e}^c_{ij}(t+\delta t)\right]\mathbf{e}^c_{ij}(t+\delta t) \quad (2.6)$$

$\mathbf{e}^c_{ij}$ is the unit bond vector, $\mathbf{e}^c_{ij} = \mathbf{r}^c_{ij}/|\mathbf{r}^c_{ij}|$. Equation (2.6) ensures that $(\mathbf{v}_i - \mathbf{v}_j)\cdot\mathbf{e}_{ij} = 0$.

Coding the constraint algorithm presents little additional complications; an extra round of communications is required to ensure that both ends of a single dimer lie on the same processor before calculating the constraint forces.

Chapter 3

Theory of Phase Separation

This chapter will review the physical concepts underpinning phase separating fluids. To begin, the equilibrium thermodynamics of systems which undergo a phase transition is reviewed. Developing upon this, stable, meta-stable and unstable regions of the free energy curve are discussed. The dynamics of the separation process are introduced through a Cahn-Hilliard model which is extended to include the effects of a velocity field and shown, using scaling arguments and dimensional analysis, to yield three growth regimes. Predicted forms for the static structure factor are discussed.

3.1 Phase Transitions

When water boils, the phase of the system changes from liquid to gas: this is one example of a *phase transition.* Equilibrium thermodynamics describes such transitions using a function known as the *free energy*, which reaches a global minimum when a system is in equilibrium. A phase transition occurs when there is a discontinuity in a derivative of the free energy, this is usually reflected by a sharp change in a parameter describing the system: for example, boiling water is marked by a sharp decrease in the density.

As a function of temperature and pressure, water can exist as a solid, a liquid or a gas. On a temperature against pressure graph it is possible to plot the boundaries which separate each of these regions; the diagram which results is called a phase diagram, figure 3.1(a). Crossing any of the lines in figure 3.1(a) results in a phase transition. The lines themselves are called coexistence lines, since, for a system exactly on a coexistence line both phases can exist, separated by an interface. For $T < T_c$, increasing the pressure through the gas/liquid coexistence curve results in a phase transition, manifest in a discontinuous change in density. The gas/liquid transition, at $T \neq T_c$, and the liquid/solid transition are examples of *first order* phase transitions. The order of a transition is determined by the lowest order derivative of the free energy which is discontinuous; if it is a first derivative the transition is first order, if it is a higher order then the transition is said to be continuous. The gas/liquid coexistence curve then represents a line of first order transitions, beginning at the triple point T_p (where all three phases coexist in equilibrium), and ending in a critical point T_c. Beyond T_c, it is possible to

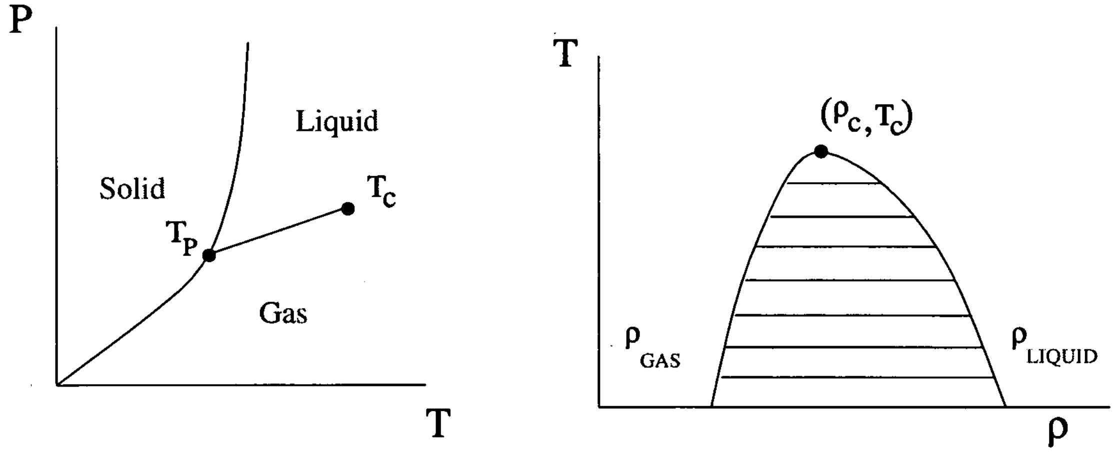

Figure 3.1: Phase diagram for a simple liquid. (a)As a function of the intensive variables, pressure and temperature, and showing the three different phases separated by coexistence lines. (b)Shows the region surrounding T_c, as a function of the extensive variable ρ. The density difference between the two phases decreases with increasing T, becoming zero at T_c. Horizontal tie lines show the value of ρ in the two separated phases for a system prepared under the binodal curve.

move from a liquid, to a gas phase with no discontinuities in density. Since no higher order derivatives of the free energy are discontinuous, there is no phase transition.

The region surrounding the critical point itself contains a wealth of interesting physics; derivatives of the free energy may become infinite, spatial correlations develop over all lengthscales, universality manifests in numerous scaling relations. Discussion of such *critical phenomena* lies outside the scope of the present work.

3.1.1 Free Energy

For nearly all systems which undergo a phase transition, it is possible to find a macroscopic observable, the value of which reflects the state in which the system finds itself: such a quantity is known as an order parameter and will be denoted ϕ. Typically ϕ is a macroscopic observable that is zero in a disordered phase and greater than zero in an ordered phase. How to define a suitable order parameter depends on the system under consideration. For example in a ferromagnet, the order parameter is the magnetisation, for the gas/liquid transition it becomes $\rho - \rho_c$, the deviation of the actual density from the critical density, in a binary fluid, the composition is a suitable choice.

Let's consider a system of fixed T, with volume V and particle number N also fixed. For this set of constraints the appropriate form of the free energy is given by Helmholtz, and is defined macroscopically by

$$F = F(T, V, N) = E - TS \tag{3.1}$$

where E is the internal energy and S is the entropy. The Helmholtz free energy provides a link between thermodynamics and statistical mechanics via the bridge equation:

$$e^{-\beta F} = \sum_{\vec{\mu}} e^{-\beta H_{\vec{\mu}}} \tag{3.2}$$

where $\beta = 1/k_B T$, H is the Hamiltonian for the system which will be a function of the microscopic degrees of freedom denoted $\vec{\mu}$, for example in a fluid $\vec{\mu}$ is the complete set of particle positions and velocities. The sum is implicitly over all the microstates of the system. It will be advantageous to express F as a function of the order parameter ϕ. This is equivalent to summing the right hand side of (3.2) over values of $\vec{\mu}$ consistent with a given ϕ.

$$e^{-\beta F(\phi)} = \sum_{\vec{\mu} \in \phi} e^{-\beta H_{\vec{\mu}}} \tag{3.3}$$

$F(\phi)$ can be used to predict when transitions will occur and what the value(s) of ϕ will be in the final state. Calculating $F(\phi)$ using (3.3) is generally impossible: however one can determine the generic shape of the free energy by appealing to a symmetry argument. To proceed it will be useful to work in terms of the free energy per unit volume $f(\phi) = F(\phi)/V$ and to assume that $f(\phi)$ may be expressed as a power series in ϕ. It is possible to write down the functional form

$$f(\phi) = a_1(T) + a_2(T)\phi^2 + a_3(T)\phi^3 + a_4(T)\phi^4 + a_5(T)\phi^5 + a_6(T)\phi^6 + ... \tag{3.4}$$

where the temperature dependence has been absorbed into the coefficients. For a symmetric system, under the transformation $\phi \rightarrow -\phi$, $f(\phi)$ must be unchanged, thus $f(\phi)$ can contain no odd powers of ϕ and the coefficients $a_1, a_3, a_5, ...$ may be set to zero. To describe a second order transition, it is sufficient to stop at order ϕ^4. This implies that $a_4 > 0$ to stabilise the system. Commonly, one sets $a_4(T)$ to be a constant and absorbs the T dependence into a_2, using $a_2 = (T - T_c)/T_c$. Using this simple model it is possible to explore the phase behaviour as a function of T. The free energy density, $f(\phi)$, is sometimes referred to as a Landau free energy.

For $T > T_c$ the equilibrium value of ϕ is zero, thus $f(\phi)$ must have a global minimum at $\phi = 0$. For $T < T_c$ the equilibrium value of ϕ is non-zero so the global minimum must shift. The form of the coefficients results in a double well structure for $T < T_c$. The depths of these wells will be equal unless there is an applied external field. If a ferromagnet finds itself in a state described by the $T < T_c$ curve in figure 3.2 the magnetisation will choose one of the wells; an

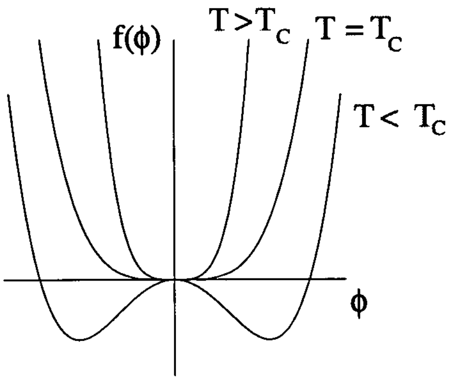

Figure 3.2: Landau free energy. Above T_c there is only one global minimum at $\phi = 0$, below T_c there are two minima which allow for the existence of two equilibrium phases having different ϕ. Shown here is the case for zero external field where the two wells have equal depth. For non-zero external field one of the wells will be lower.

example of spontaneous symmetry breaking. The magnet can do this since it has a non-conserved order parameter, a down spin may flip to being an up spin with impunity. In the case of a binary fluid the order parameter is conserved, since both the total mass and the total particle number of the constituent species is constant.

The simplest model of a binary fluid is a 50:50 mixture of thermodynamically symmetric species (two type A particles interact in the same way that two type B particles interact, the AB interaction is different). For such a system $f(\phi)$ is exactly as discussed above (figure 3.2) so long as ϕ, the order parameter, is taken as $\phi_A - \phi_B$, where ϕ_A and ϕ_B are the volume fractions of the two species.

3.1.2 Conserved order parameters—the symmetric, binary fluid

Systems with conserved order parameter may separate into two regions, each with a different value of ϕ, coexisting as the equilibrium state (as on the gas/liquid coexistence line). The transition is then between a high T state consisting of a single phase of uniform ϕ, and a low T state consisting of two coexisting phases of different ϕ separated by an interface. Note that for a binary fluid, ϕ [$= \phi_A - \phi_B$], need not vanish in the *disordered* (high T) phase, and in general $f(\phi)$ need not be symmetric (although that remains the simplest case).

In such a system the total free energy is the sum of the free energies of the two phases; the condition for separation becomes that this sum is less than the free energy of the homogeneous system (with uniform ϕ).

$$F^{TOT} = F(T, V_1, V_2, N_1, N_2) + F(T, V_2, V_1, N_2, N_1) \tag{3.5}$$

The volumes of the different domains are V_1 and V_2, N_1 and N_2 are the number of particles of a single component in each phase. The system is free to find its own values of V_1,V_2,N_1 and N_2, that minimise the total free energy. The equilibrium state can be found by minimising F^{TOT} subject to constraints $V_1 + V_2 = V$; $N_1 + N_2 = N$.[1]

Lagrange multipliers may be used to minimise equation (3.5) subject to the given constraints. Assuming the free energy per unit volume a function of ϕ only, then:

$$F^{TOT} = V_1 f(\phi_1) + V_2 f(\phi_2) \tag{3.6}$$

where ϕ_i is the volume fraction of domain i occupied by a single component; for a binary system the choice of component is arbitrary (i.e. $\phi_i = N_i/V_i$). Proceeding with the minimisation, a new function Ψ is defined, $\Psi = F^{TOT} + \alpha V + \beta N$, where α and β are Lagrange multipliers. It then remains to find the minimum of Ψ with respect to V_1, V_2, N_1 and N_2. It is sufficient to set the first derivative of Ψ, with respect to each of the variables, equal to zero.

Taking the derivative with respect to N_1 and N_2 gives:

$$\left.\frac{\partial f}{\partial \phi}\right|_{\phi=\phi_1} = \left.\frac{\partial f}{\partial \phi}\right|_{\phi=\phi_2} = -\beta \tag{3.7}$$

---

[1] Strictly speaking F^{TOT} will have a contribution from the interface between the domains, the contribution from this interface will be small compared to the contribution coming from the bulk.

similarly for V_1 and V_2:

$$f(\phi_1) - \phi_1 \left.\frac{\partial f}{\partial \phi}\right|_{\phi=\phi_1} = f(\phi_2) - \phi_2 \left.\frac{\partial f}{\partial \phi}\right|_{\phi=\phi_2} = -\alpha \qquad (3.8)$$

The Lagrange multipliers may be identified with pressure and chemical potential; $\alpha = -P$, $\beta = -\mu$. Taken together, equations (3.7) and (3.8), show that constructing a common tangent between the two free energy wells satisfies the conditions for equilibrium, see figure 3.3.

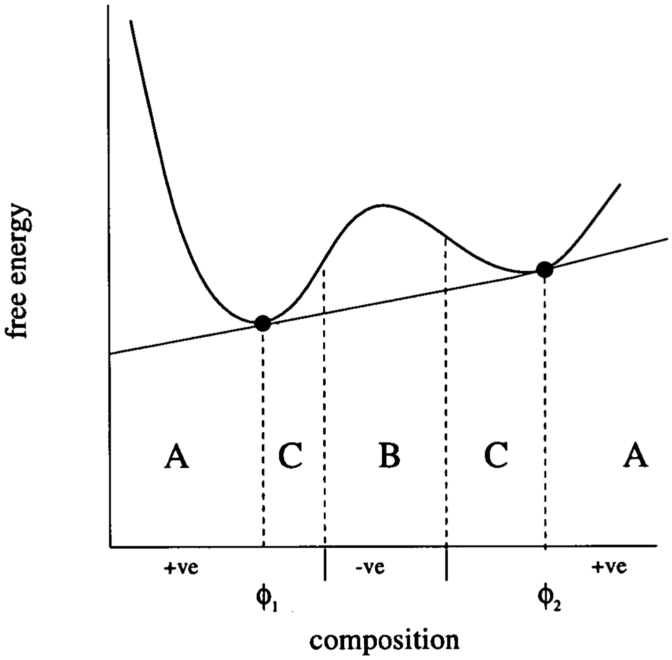

Figure 3.3: Typical free energy for a binary fluid, to allow for asymmetric mixtures the wells have been given unequal depths. The three possibilities for separation are marked together with regions of positive and negative curvature.

If a system, initially at ϕ, can find values of ϕ_1 and ϕ_2 which satisfy $\phi_1 + \phi_2 = \phi$, and represent a lowering of total free energy, then the system will separate. This process continues until two phases are formed which have order parameters with a common tangent.

A negative local curvature means any two values of ϕ either side of the initial ϕ lower the total free energy. In this case the system is unstable to any fluctuations in ϕ and will spontaneously begin separating, this is known as spinodal decomposition. The only other possibility for separation occurs when the local curvature is positive, but the system can find compositions which lower the free energy by traversing the barrier between the wells, this is known as nucleation. In summary, there are three possibilities for a homogeneous binary mixture.

A: The system is stable and the composition remains uniform.

B: The system is locally unstable, separation proceeds until two phases of composition ϕ_1 and ϕ_2 are reached; ϕ_1 and ϕ_2 are given by a common tangent construction.

C: Although the system is locally stable it will separate if perturbations (thermal or external) are great enough to overcome a nucleation (free energy) barrier. Physically, this means that only domains greater than a critical size will be stable and once formed they will continue to grow.

3.2 Dynamics

For a mixed system cooled below the spinodal, equilibrium states are completely described by the preceding thermodynamic arguments. Initially the system is homogeneous, in the final state it comprises two domains, separated by a flat interface. This section defines a framework for describing what happens in between, when ϕ is a function of position and time.

3.2.1 Cahn-Hilliard Theory

Up to now, discussion of the free energy has been limited to regions of space which have a uniform value of ϕ. For the binary fluid above T_c, the region is the entire system, below T_c there are two regions separated by an interface.

While the system is undergoing separation, ϕ must vary over time, and over length scales small compared to the system size. The question of dynamics, becomes a matter of finding an evolution equation for $\phi(\mathbf{r},t)$ or for its probability distribution. This equation must depend on whether ϕ is conserved or nonconserved; the following discussion assumes ϕ is conserved and the total volume fraction of a single phase is $\phi_0 = 0.5$. For ease of notation, $\phi(\mathbf{r},t)$ will simply be denoted ϕ unless stated otherwise. Consider a binary system in which the component particles lie on the nodes of a lattice and can exchange positions (so there is no momentum transfer); such systems exist in the form of binary alloys [50].[2] It is clear, physically, that only through the local exchange of particle types can ϕ evolve. This leads to a diffusive transport mechanism, and a thermodynamic equation of motion

$$\frac{\partial \phi}{\partial t} = -\nabla \cdot \mathbf{j} \tag{3.9}$$

where $\mathbf{j} = \mathbf{j}_A - \mathbf{j}_B$ is the difference in the local flux of unlike particles, caused by gradients in the chemical potential: $\mathbf{j} = -M\nabla\mu$, M is a transport coefficient which is usually assumed not to be a function of ϕ.[3] Here μ is an *exchange* chemical potential given by $\mu = \mu_A - \mu_B$, it may be expressed as a functional derivative of a *local free energy*: $\mu = \delta F[\phi]/\delta\phi$. This gives an equation of motion for ϕ,

$$\frac{\partial \phi}{\partial t} = \nabla \cdot M\nabla \left(\frac{\delta F}{\delta \phi}\right) \tag{3.10}$$

It is important to clarify what is meant by $F[\phi]$, in the previous section the free energy was a function of ϕ, and ϕ was constant over the region considered. Now ϕ is allowed to vary and the form of the free energy must allow for this. To construct $F[\phi]$, consider partitioning space into regions with volume Λ^3. If Λ is sufficiently small ϕ may be considered uniform over the subvolume, thus $F[\phi]$ will have a contribution from a local Landau free energy. There must also be a term

---

[2] Although these models cannot describe a fluid, since they have no velocity field, it will be shown that the early time behaviour of a binary fluid is closely related to that of a binary alloy.

[3] Note that in reference [6], M is a function of ϕ, this is used to induce a transition into a glassy phase at high ϕ.

which penalises gradients in ϕ and so drives the system toward a uniform state. Putting these together gives:

$$F[\phi(\mathbf{r},t)] = \int d\mathbf{r} \left(\frac{1}{2}\kappa \left(\nabla\phi\right)^2 + f(\phi) \right) \tag{3.11}$$

where $(\nabla\phi)^2$ is the first non-trivial gradient term in ϕ, consistent with the symmetries of the system, κ is a phenomenological constant related to surface tension and $f(\phi)$ is the usual Landau free energy discussed in the previous section.

Combining (3.10), with the form of $F[\phi]$ given by (3.11), gives the celebrated Cahn-Hilliard equation,

$$\frac{\partial\phi}{\partial t} = \nabla \cdot \left[M\nabla \left(-\kappa\nabla^2\phi + \frac{\partial f}{\partial\phi} \right) \right]. \tag{3.12}$$

The Cahn-Hilliard equation describes only relaxation behaviour, thus it cannot be used to describe nucleation which would require a noise term capable of putting energy into the system.

A solution of (3.12) may be found by linearising about the mean initial volume fraction ϕ_0. Expressing the order parameter as $\phi = \phi_0 + u(\mathbf{r},t)$, with $u(\mathbf{r},t)$ representing fluctuations about ϕ_0, the Fourier transform of (3.12) yields: (setting $M = \text{const} = \lambda$)

$$\frac{d\tilde{u}(\mathbf{k},t)}{dt} = \omega(k)\tilde{u}(\mathbf{k},t) \tag{3.13}$$

where

$$\omega(k) = -\lambda k^2 \left[\kappa k^2 + \frac{\partial^2 f}{\partial\phi_0^2} \right] \tag{3.14}$$

where $k = |\mathbf{k}|$. If the initial state has a volume fraction ϕ_0 such that $\partial^2 f/\partial\phi_0^2 > 0$, the amplitude of any fluctuation will decrease in time ($\omega(k) < 0$), and the system is stable. If $\partial^2 f/\partial\phi_0^2 < 0$, fluctuations are unstable ($\omega(k) > 0$) for wave vectors in the range $0 < k < k_0$ where $k_0 = \left[-\left(\partial^2 f/\partial\phi_0^2\right)/\kappa \right]^{1/2}$. Figure 3.4(a) shows the two behaviours. A key prediction of linearised Cahn-Hilliard theory is the behaviour of the *structure factor* $S(\mathbf{k},t)$, defined by $S(\mathbf{k},t) = \langle |\tilde{u}(\mathbf{k},t)|^2 \rangle$ (for a discussion on the meaning $S(\mathbf{k},t)$ refer to appendix A). According to (3.13) there should be

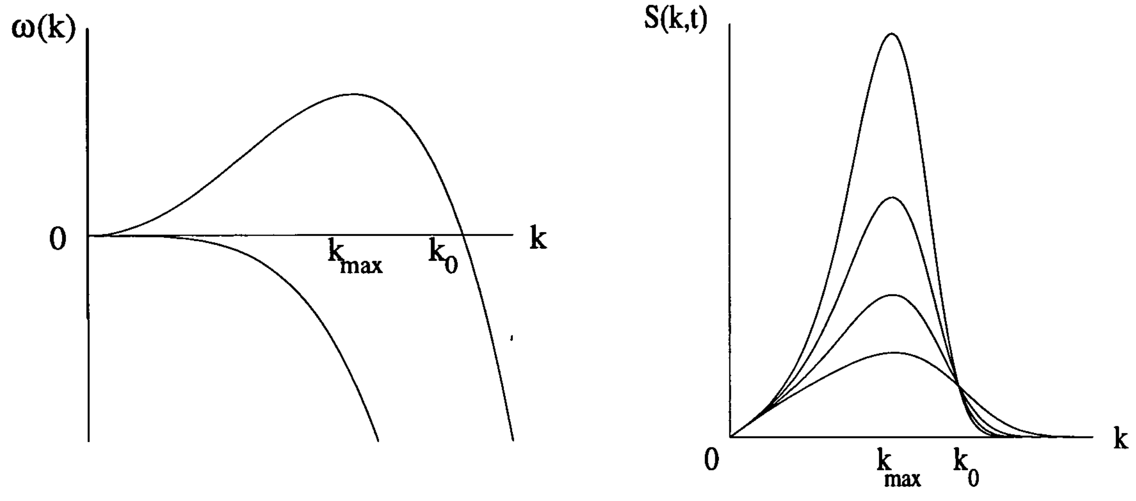

Figure 3.4: Linearised Cahn-Hilliard predictions for the stability of a binary alloy. (a) For negative curvature the system is unstable for $0 < k < k_0$ (upper curve), and there is a dominant wavenumber at k_{max}. For positive curvature the system is everywhere stable (lower curve). (b) The structure factor has a single peak which grows with time.

a peak in $S(k,t)$, located at k_{max}, whose height increases exponentially in time, and whose position is stationary, see figure 3.4(b). Since the fluctuations are growing exponentially, it is not long before non-linear effects become important, thus linearised Cahn-Hilliard is only useful in describing the earliest stages of the separation.

3.2.2 Non-linear theories

It is possible to account for fluctuations by adding a Langevin force to the right hand side of (3.10), this describes the effect of Brownian motion on composition variations. A master equation may be derived for the distribution functional $\rho[\phi]$, which expresses the probability of any particular ϕ being realised. The equation of motion for $S(\mathrm{k},t)$ is then obtained by multiplying the master equation by $\phi\phi_0$ and integrating over ϕ. It takes the form,

$$\frac{\partial S}{\partial t} = -2Mk^2\left[\left(\kappa k^2 + \frac{\partial^2 f}{\partial \phi_0^2}\right)S + \frac{1}{2}\frac{\partial^3 f}{\partial \phi_0^3}S_3 + \frac{1}{6}\frac{\partial^4 f}{\partial \phi_0^4}S_4 + \ldots\right] + 2Mk_BTk^2 \tag{3.15}$$

where the notion of higher order two point correlation functions S_n has been introduced (defined by the Fourier transform of $\langle u^{n-1}(\mathbf{r})u(\mathbf{r}_0)\rangle$). Equation (3.15) is the first of a hierarchy of equations for higher order S_n, the problem becomes one of how to close this hierarchy.

A simple approach would be to neglect all higher order terms (first performed by Cook [51]), equation (3.15) then reduces to the prediction of linearised Cahn-Hilliard theory with added noise.

In a more sophisticated approach, Langer, Bar-on and Miller [52] developed an approximate closure which allowed higher order multi-point correlation functions to be expressed as simple functions of S. The resulting form for $S(\mathbf{k}, t)$ predicts a well defined maximum which moves to smaller values of k, with increasing time, in qualitative agreement with experiment and simulation. It also satisfies dynamic scaling; this will become important in the following section. The theory cannot describe nucleation and subsequent growth; also predictions for the later stages of spinodal decomposition do not agree with observation. Several authors have extended the Langer, Bar-on and Miller method: the Kawasaki-Ohta [53] theory incorporates hydrodynamics but is based around the same approximations made by LBM and so fails at late times. Furukawa [54] has extended (3.15) based on asymptotes of S at low and high k and the form S must take around the peak. Other approaches include the cluster diffusion model of Binder and Stauffer [55], which assumes a purely diffusive process and thus is limited to early times.

All of these approaches, and others [56–58], involve an ad-hoc approximation of some sort. However some idea of the late time behaviour of $S(k)$ can be gleaned from scaling arguments which will be introduced in the next section.

3.2.3 Scaling

During the spinodal decomposition process, regions of predominantly one type of fluid form. These regions create an interlocking domain network, figure 3.5, and have long been observed in experiment and more recently in simulations. The self-similarity of the pattern over time has led to the proposal that there is one, and only one, lengthscale involved. This lengthscale would be a measure of the average domain size. For this to be valid the interfacial width ξ, which constitutes a second lengthscale, must not contribute to the physics. At late times L can become much larger than ξ and so the assumption that ξ is not important would appear to be valid.

Such ideas lead to the scaling hypothesis proposed for spinodal decomposition: *a single characteristic lengthscale $L(t)$ exists, such that, the domain structure is, in a statistical sense, independent of time when lengths are scaled by $L(t)$.*

Applying the scaling hypothesis to the pair correlation function $p(\mathbf{r},t)$, [4] gives $p(\mathbf{r},t) = f(r/L)$ where f is some function of r/L only, the structure function can now be written in the scaling form,

$$S(\mathbf{k},t) = L^d F(kL) \tag{3.16}$$

where d is the dimension and $F(x)$ is the Fourier transform of $f(x)$. Equation (3.16) implies that when plotted appropriately, the data at different times and wavenumber should collapse onto a single curve.

3.2.4 Symmetric Binary Fluids: Dynamic Scaling for $L(t)$

A full treatment of the separation process in binary fluids must account for the velocity field, lacking in the Cahn-Hilliard model. When the constituent particles are free to move, the order parameter will be convected by the velocity field and, in turn, gradients in the order parameter will drive the velocity field. An appropriate model, which combines these effects together with the usual Navier-Stokes equation is [59] (M = const = λ for simplicity):

$$\frac{\partial\phi(\mathbf{r},t)}{\partial t} + \mathbf{v}(\mathbf{r},t)\cdot\nabla\phi(\mathbf{r},y) = \lambda\nabla^2\mu(\mathbf{r},t) \tag{3.17}$$

---

[4] $p(\mathbf{r},t)$ expresses the probability of finding two like particles separated by $\mathbf{r}$ at time t, it is given by the Fourier transform of $S(\mathbf{k},t)$

$$\rho\left(\frac{\partial \mathbf{v}(\mathbf{r},t)}{\partial t}+(\mathbf{v}(\mathbf{r},t)\cdot\nabla)\mathbf{v}(\mathbf{r},t)\right) = \eta\nabla^2\mathbf{v}(\mathbf{r},t)-\nabla p-\phi(\mathbf{r},t)\nabla\mu(\mathbf{r},t) \quad (3.18)$$

$\mathbf{v}$ is the local fluid velocity, p is the pressure, η is the viscosity, and the density ρ is assumed constant i.e. the system is incompressible. The final term in (3.18) arises from the free energy change $\phi\delta\mu$ per unit volume that accompanies the transport of a fluid region with order parameter ϕ over a distance for which the change in the chemical potential is $\delta\mu$: that is, chemical potential gradients act as a driving force on the fluid. This model is highly non-linear and, at the time of writing, impossible to solve analytically. Progress can be made through simple dimensional analysis.

Consider the symmetric binary mixture at high T ($T > T_c$); the fluid types are completely mixed and the phase is homogeneous. The instant following a deep quench, to well below T_c, the system will remain mixed. At this point there are no interfaces: ordering will be governed by single particle diffusion, when like particles come close enough the molecular interactions tend to keep them together. This is the essential mechanism for the evolution of ϕ in the early stages of spinodal decomposition. The order parameter may be taken as uniform throughout the fluid, therefore the advection term on the left hand side of (3.17) may be set to zero to leading order. Assuming the scaling hypothesis is valid, spatial derivatives can be approximated by $1/L$: if L is the only lengthscale any spatial variations must be over distances of order L. Approximating ∇^2 with $1/L^2$ and μ with σ/L (a quantity with the same dimensions as μ) gives $L \sim (\lambda\sigma)^{1/3}t^{1/3}$.[5]

In this way interfaces will form; at first they will be diffuse and indistinct, but by the time domains are two or three times the equilibrium interfacial width, the interfaces will be crisp. Now interfacial tension, and fluid motion caused by moving interfaces becomes dominant regarding the coarsening process, and the role of single particle diffusion is negligible. A two dimensional cross-section

---

[5] In off critical mixtures the hydrodynamic coalescence of droplets, driven by Brownian motion, gives an unrelated $t^{\frac{1}{3}}$ growth law. This mechanism will be discussed further in Chapter 3.

though the system is shown in figure 3.5. Interfaces are well formed and the domains of separated fluid exist at volume fractions very close to equilibrium. Evolution of ϕ now proceeds through a coarsening process, which entails the bulk flow of fluid in such a way as to increase the average size of the domains. The driving force for this flow is the interfacial tension; separation has entered a regime governed by interfacial tension and hydrodynamic response.

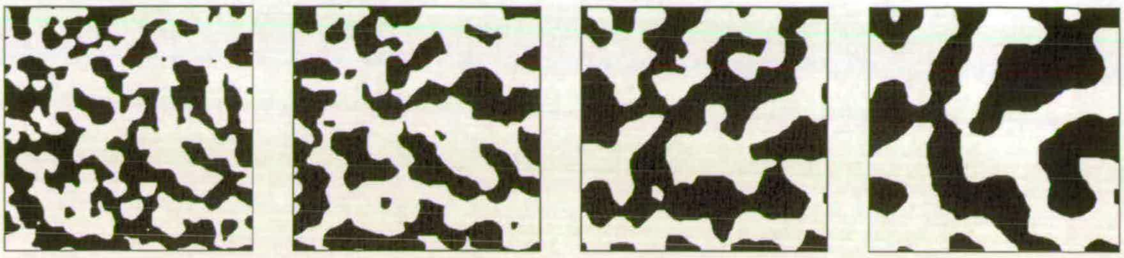

Figure 3.5: Two dimensional cross-section through three dimensional domain coarsening.

Inside a domain, the chemical potential will be constant since gradients can only enter at the interfaces, so the final term in (3.18) may be set to zero. Surface tension will create a capillary pressure $\sim \sigma/L$; this pressure must be balanced by an internal pressure set up within the bulk. It is the source of the internal pressure which will determine the rate of domain coarsening. Inspection of eq. 3.18 immediately shows that there can only be two sources for this internal pressure; viscosity or inertia.

An estimation the magnitude of each of the terms in equation (3.18), using $1/L$ for spatial derivatives gives:

$$\rho(\frac{\partial \mathbf{v}(\mathbf{r},t)}{\partial t}) + (\mathbf{v}(\mathbf{r},t)\cdot\nabla)\mathbf{v}(\mathbf{r},t) \sim \rho\frac{L}{t^2} \tag{3.19}$$

$$\eta\nabla^2\mathbf{v}(\mathbf{r},t) \sim \eta/Lt \tag{3.20}$$

To avoid confusion, note that t in the above equations refers to time. Equating the viscous term to the driving term, σ/L and rearranging for L gives $L \sim (\sigma/\eta)\,t$. Doing the same except substituting the inertial term for the viscous term gives

$L \sim (\sigma/\rho)^{1/3} t^{2/3}$. Comparing the sizes of the viscous to inertial terms, they are of the same order when $L \sim \eta^2/(\sigma\rho)$ and $t \sim \eta^3/(\sigma^2\rho)$. At earlier times, and smaller lengths than this the viscous term dominates over the inertial.

To summarise, scaling arguments predict three power laws for the growth of the domain size $L(t)$, after a deep quench into the spinodal region:

$$L(t) \sim \begin{cases} (\lambda\sigma t)^{1/3}, & L \ll (\lambda\eta)^{1/2}, \quad \text{(diffusive)} \quad (3.21) \\ \sigma t/\eta, & (\lambda\eta)^{1/2} \ll L \ll \eta^2/(\rho\sigma), \quad \text{(viscous hydrodynamic)} \quad (3.22) \\ (\sigma t^2/\rho)^{1/3} & L \gg \eta^2/(\rho\sigma), \quad \text{(inertial hydrodynamic)} \quad (3.23) \end{cases}$$

Diffusion controlled growth dominates until well defined interfaces form, this happens when the domains are of the order of the capillary length $L \sim (k_B T/\sigma)^{\frac{1}{2}}$. Then surface tension effects drive fluid flow, the rate determining factor is first internal fluid viscosity, then a crossover takes place into a late time regime wherein inertial effects dominate the coarsening. Although dimensional analysis has given expressions for how quickly the network coarsens, it cannot be used to elicit a full expression for the structure factor.

Most of the analysis within Chapters 4 and 5 is devoted to testing the validity of the scaling hypothesis and the growth laws it predicts. Since the DPD algorithm includes hydrodynamics, the emphasis will be on studying the two hydrodynamic regimes.

Chapter 4

Qualitative Physics: coarsening mechanisms

In this chapter we investigate the three power law growth regimes using interface and velocity maps taken from large scale D.P.D. simulations. Three separate mechanisms, all of which give rise to $t^{1/3}$ growth, are identified and explained. The Siggia *necking down* mechanism, predicted to operate in the viscous hydrodynamic regime, is explicitly tested. A qualitative discussion is presented, highlighting the differences in domain structure between inertial and viscous growth. These were large scale simulations, using 10^6 particles. A selection of data sets has been used; the choice of parameters and units for these sets is explained in Chapter 5.

4.1 Coarsening

Figure 4.1 shows the evolution, with time, of a 50/50 mixture of two (symmetric) fluids. The drawn surface separates fluid of different types. In order to use this visualisation technique, interfaces must be present, therefore the very early stages (where linear Cahn-Hilliard theory would be applicable) are excluded. Within a

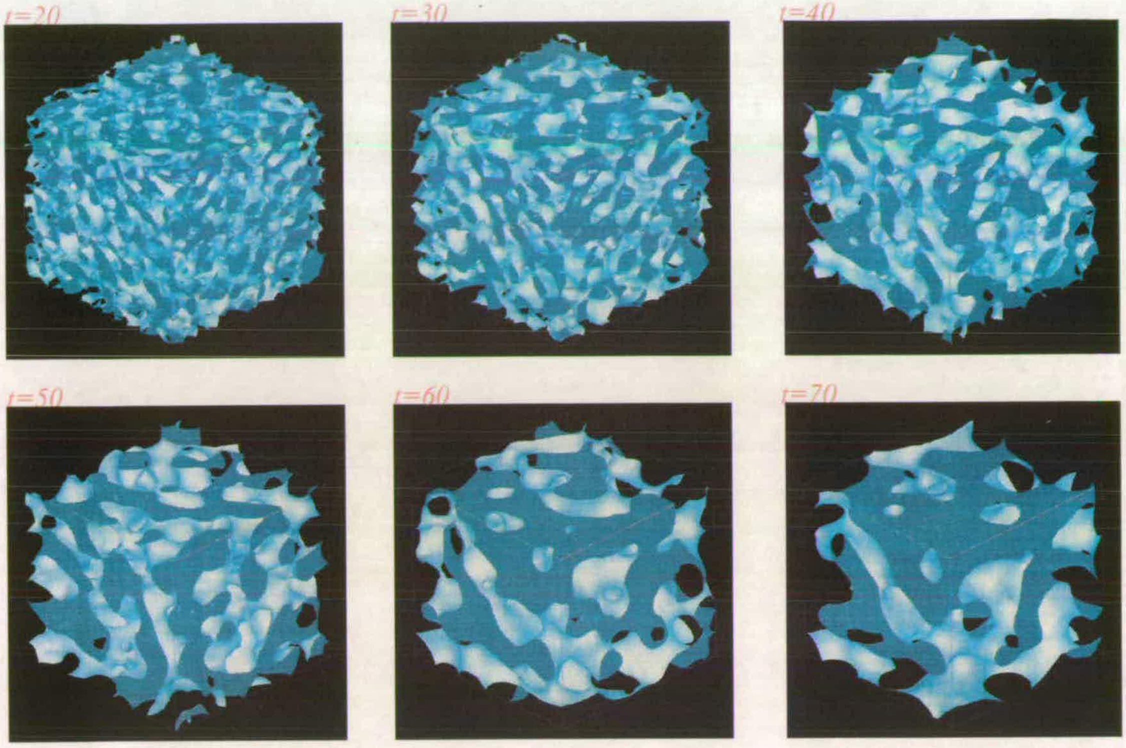

Figure 4.1: A symmetric binary fluid evolving, from a homogeneous phase, towards equilibrium. The fluid has been subjected to a deep quench, well below T_c, into the spinodal region. The blue structure represents the interface separating domains of different ϕ. Interfaces are well formed and so the average domain size is expected to show power law growth. This data is for a low Reynolds number simulation (Re~ 1).

scaling regime, the general form for L is,

$$L \sim t^n \tag{4.1}$$

where n can be one of three values depending on the underlying coarsening mechanism.

4.2 Diffusion based scaling: $n = 1/3$

There are three mechanisms which give rise to an exponent of 1/3. Single particle diffusion has already been introduced (and leads to equation (3.21)); the theory of Lifshitz, Slyozov and Wagner and the notion of droplet coalescence induced by Brownian motion constitute the other two.

4.2.1 Lifshitz, Slyozov and Wagner

In 1961 Lifshitz and Slyozov [60], and independently Wagner [61] (LSW) deduced an exact result for the growth of droplets of a minority phase, in the limit that the minority phase occupies a negligible volume fraction. They looked at a droplet composed of type B particles existing in a *supersaturated broth* of type A particles. If the equilibrium volume fraction is ϕ_1 inside the droplet, and ϕ_2 outside the droplet, supersaturated refers to the situation where the actual volume fraction outside the droplet is $\phi_2 + \Delta$, where $\Delta \ll 1$.

For a spherical droplet with radius L, they were able to show:

$$\frac{dL}{dt} = \frac{2D\xi}{L}\left(\frac{1}{L^*} - \frac{1}{L}\right) \tag{4.2}$$

where D is the diffusion coefficient, ξ is the capillary length (a lengthscale of the order of the interfacial width) and L^* sets the lengthscale for droplet stability. For $L < L^*$ the droplet shrinks; for $L > L^*$ the droplet grows. The constant L^* may be identified as the critical lengthscale at which fluctuations of ϕ become stable in the process of nucleation; its value is given by $L^* = (\phi_1 - \phi_2)2\xi/\Delta$. Essentially, the LSW theory predicts that gradients in chemical potential form, these induce the diffusion of B particles, through the surrounding matrix, from small to large droplets. Taking the average radius to be $L = L^*$, equation (4.2) expresses the growth of average droplet size: $dL/dt \sim 1/L^2$, which implies the $n = 1/3$ growth law, but with a coefficient different from that in equation (2.22).

Experiments have confirmed the LSW growth law, however the predictions of LSW theory for the droplet size distribution are inaccurate. This is believed to be a result of the correlation and screening between droplets, which has an increasing effect as ϕ is increased, and is not accounted for in the theory.

Since LSW assumes a vanishingly small volume fraction of minority phase, it is unlikely to account for the growth seen at the volume fractions used in this thesis (the lowest of which is $\phi = 0.2$). Nevertheless it is important to make the distinction between LSW $n = 1/3$, and the $n = 1/3$ growth encountered in this work.

4.2.2 Brownian Motion Induced Droplet Coalescence

This mechanism applies to off-critical mixtures below the *percolation threshold* [1] and was first proposed by Smoluchowski [63] in the context of coagulation of colloids. It was applied to phase separation by Binder and Stauffer [55] and Siggia [64]. As in the LSW theory, the minority phase exists as droplets, but there is no condition on the degree of saturation in the majority phase. The essential idea is that thermal fluctuations cause the coalescence of droplets through Brownian motion. For this to work, the coalescence process (the amalgamation of two touching droplets to form a single spherical droplet) is assumed to happen on a timescale much faster than the average time between droplet collisions. Scaling is assumed, so there is only a single lengthscale L, which must describe the droplet radius and the average distance between droplets.

The diffusion constant of a droplet of size L is given by the Einstein relation as $D \sim k_B T/(\eta L)$. The time for a droplet to diffuse a distance of order L (and thus to come into contact with another droplet) is $t \sim L^2/D \Rightarrow L \sim (k_B T t/\eta)^{1/3}$. This $t^{1/3}$ growth mechanism has a prefactor different from both equation (2.22), and the LSW prefactor. In figure 4.2 an off-symmetric[2] ($\phi = 0.25$), binary fluid

---

[1] For a mixture to percolate, at least one domain of the minority component must span the system. If $\phi = 0.5$ the mixture must percolate, as ϕ is decreased this becomes less obvious. The value of ϕ at which the system percolates is known as the percolation threshold; its value is not known exactly in 3 dimensions. For a random structure in 3 dimensions, estimates place it at around $\phi_p = 0.15$ [62]. There is no reason to suppose the spinodal network will be vastly different from this.

[2] In this context off-symmetric refers to any volume fraction not equal to 0.5. The thermo-

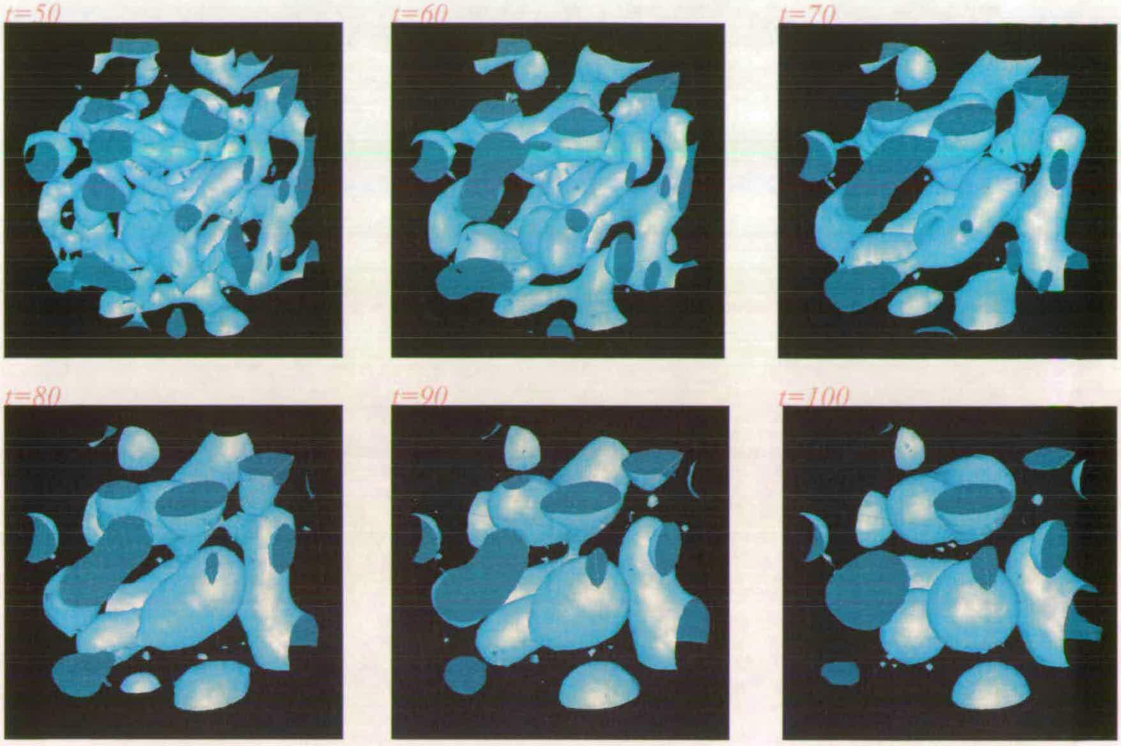

Figure 4.2: An off-critical mixture $\phi = 0.25$. When the domain size exceeds around one third of the box size the spinodal network depercolates, existing instead as droplets. Droplets can only grow when they collide and collisions are induced through Brownian motion giving $n = 1/3$ growth. Simulation details are: $N = 10^6$,$kT = 1.0$,$\gamma = 30$,$\rho = 10$,$\alpha_{AA} = \alpha_{BB} = 20$,$\alpha_{AB} = 100$.

has been quenched into the spinodal region. Initially the system forms the usual bicontinuous network, and growth proceeds via surface tension induced domain coarsening. As domains grow there is a critical length, above which interfacial area would be lower if the domains existed as isolated droplets. When this length is reached the domains depercolate; growth proceeds via Brownian motion.

Two off-critical systems were examined $\phi = 0.25$ and $\phi = 0.2$, again a deep quench into the spinodal region was performed. An estimate of $L(t)$ may be extracted from the system (the exact definition of $L(t)$ will be discussed in Chapter 5). Plotting L as a function of time gives the graphs shown in figure 4.4. For $\phi = 0.25$,

---

dynamics of the two types of particle are still symmetric.

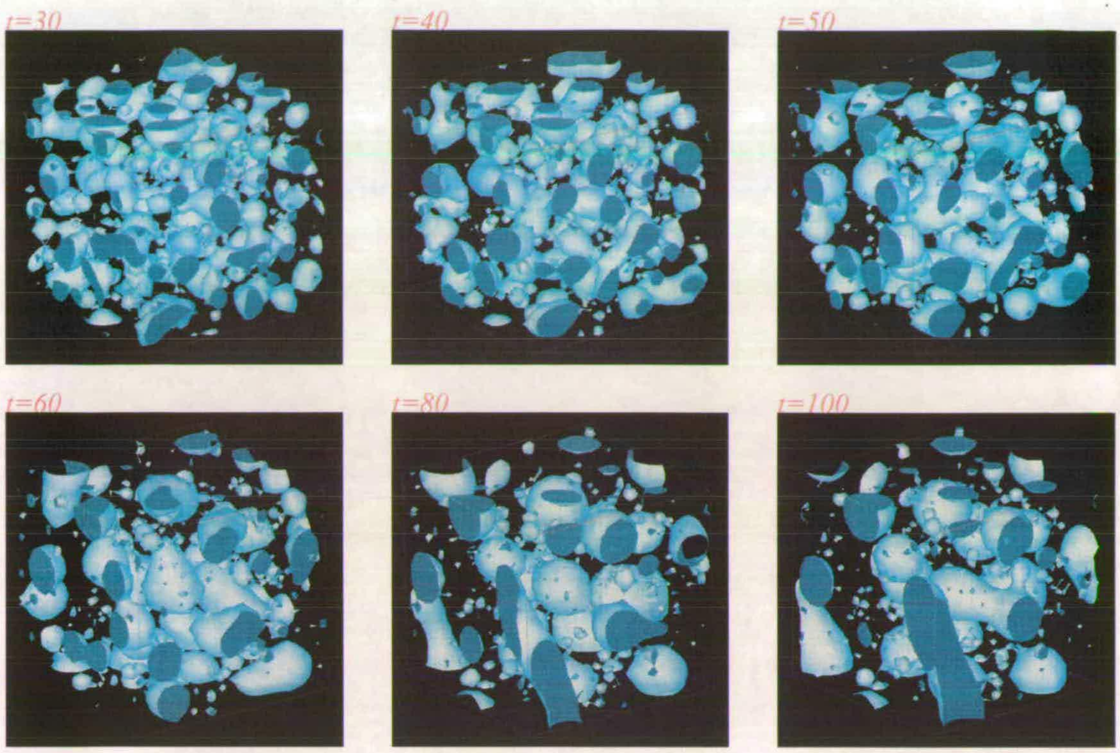

Figure 4.3: An off critical mixture $\phi = 0.20$. At lower volume fractions the minority phase is quick to depercolate. Simulation details are: $N = 10^6$,$kT = 1.0$,$\gamma = 30$,$\rho = 10$,$\alpha_{AA} = \alpha_{BB} = 20$,$\alpha_{AB} = 100$.

most of the separation takes place whilst the minority phase percolates, and so exhibits hydrodynamic growth with $n = 1$. Droplets are formed when L is between one third and one half the size of the system (see figure 4.2). At this lengthscale, finite size effects swamp the nominal growth mechanism and a clear region of $n = 1/3$ is not seen.

In an attempt to capture $n = 1/3$, the volume fraction was reduced to $\phi = 0.2$. For such a small volume fraction the system depercolates almost as soon as interfaces are formed, figure 4.3. For small times, figure 4.4 shows *almost* linear growth for $\phi = 0.2$; at $t \sim 60$ there is a definite crossover to diffusion controlled growth. The inset shows that in this region the power is very close to $n = 1/3$.

It is interesting to note that the onset of finite size effects seems to be delayed in off critical mixtures. In the viscous regime for $\phi = 0.5$, finite size effects

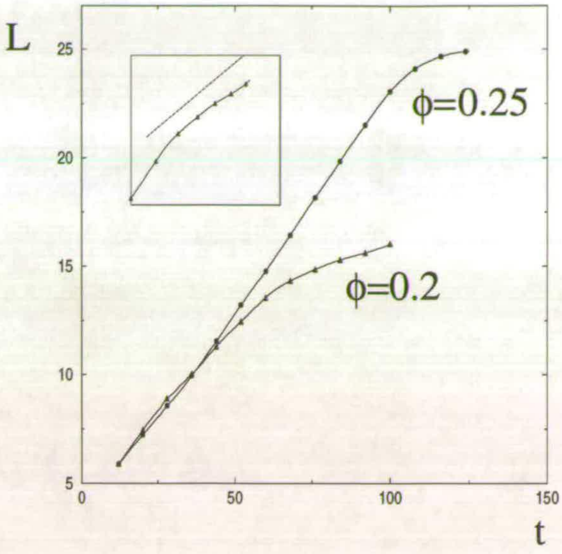

Figure 4.4: Domain growth in off critical systems. The inset shows the final stages of $\phi = 0.2$ on a double logarithmic scale; the dashed line represents $n = 1/3$

become apparent when L is approximately half the box size. In figure 4.4, L reaches around two thirds of the box size before (possibly) being affected (it is also possible that the levelling at the top of the $\phi = 0.25$ graph is simply the system becoming diffusive). Since the levelling off occurs at lengths $L \sim 23$, the curve of the $\phi = 0.2$ graph (which occurs when $L \sim 15$), is unlikely to be a finite size effect.

4.2.3 Single Particle Diffusion

In the case of a deep quench performed on a symmetric mixture, solubility will be small and therefore growth by the LSW mechanism is negligible. Also, both phases will percolate regardless of the size of L; therefore when interfaces have formed the hydrodynamic mechanisms will dominate over Brownian induced motion of the interfaces. There still exists a means for $n = 1/3$ at early times, the essential argument has been given by the dimensional analysis of the previous chapter. Many of the symmetric runs exhibit early stage growth intermediate between $n = 1/3$ and $n = 1$, this is attributed to the interplay of single particle diffusion and viscous hydrodynamics, which will occur when interfaces are just starting to form, that is, before the interfacial profile is fully developed.

4.3 Viscous regime: $n = 1$

For the viscous case the mechanism for flow has been identified by Siggia [64]. Siggia's argument is based on the effect of a Taylor instability on a tube of fluid of a single phase, surrounded by the second phase. Undulations in the radius of this tube, give rise to a pressure gradient along the axis of the tube, this causes fluid to flow from regions of high pressure to regions of low pressure. If the wavelength λ of the undulations is large enough, $\lambda \sim L$, they become unstable; the pressure gradient is large enough to induce a flow which increases the size of the undulation. Such a mechanism is illustrated in figure 4.5 and is sometimes referred to as the *necking down* instability. This mechanism will apply to any random surface with a sufficiently high connectivity; a network which percolates satisfies the connectivity requirement. In spinodal mixtures, a flow from regions of high curvature into regions of low curvature, is seen. For complicated surfaces, there exists the possibility of conflicting messages being sent into the body of the fluid, regarding the direction of flow neccessary to coarsen the mixture (in figure

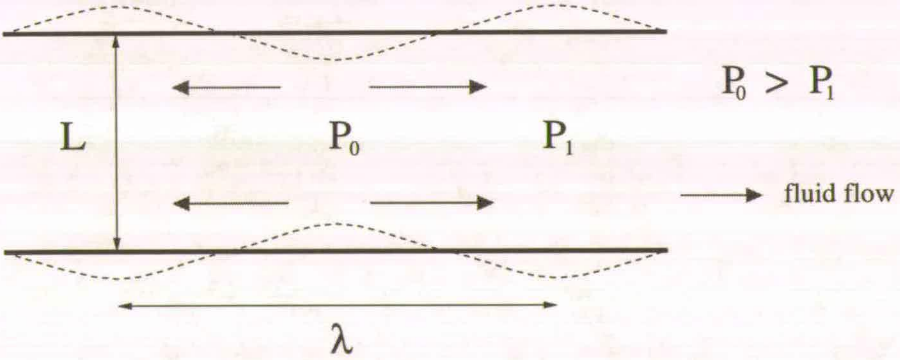

Figure 4.5: The Siggia mechanism for viscous hydrodynamics. Undulations on the surface of a tube give rise to a pressure gradient within the bulk, which in turn causes a flow out of the necks.

4.1, it is easy to imagine two necks in close proximity, having orientation which cause conflicting flow). This will not change the growth exponent, but it will lower the prefactor.

The simulation data of figure 4.6 shows necking down in operation. An interface surrounding a neck has been enlarged, and is showing the expected thinning behaviour; the corresponding velocity map clearly demonstrates a bulk flow of fluid radially out of the neck, from high to low curvature.

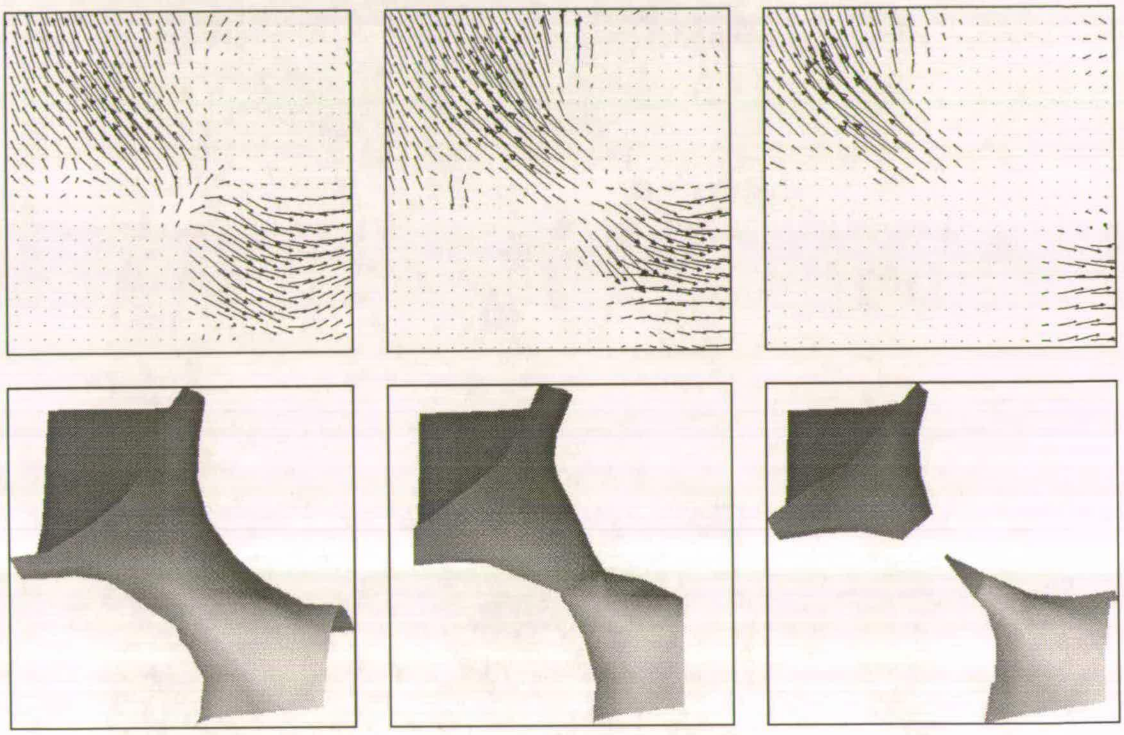

Figure 4.6: A neck breaking (bottom), with the corresponding velocity map (top); data is for a symmetric deep quench, the parameters are those of p30 detailed in Chapter 5.

4.4 Inertial regime: $n = 2/3$

When the domain size is of the order $L \sim \eta^2/\sigma\rho$ the inertial term of equation 3.18 is of similar magnitude to the viscous term. As L grows larger, inertial effects become dominant and the power law should eventually reach the late time asymptote, $L \sim t^{2/3}$.

When inertia is dominant, turbulence may be expected. Indeed the same crossover lengths and times may be obtained by taking the Reynolds number, Re$= Lv\rho/\eta$, setting it equal to unity and using dimensional analysis to arrange for L or t: the inertial regime occurs when Re> 1.

By decreasing the viscosity, η, while keeping ρ constant, the Reynolds number may be increased. Figure 4.7 shows the evolution of the surface at the highest Reynolds numbers considered (remember that Re increases within each run as the lengthscale grows). This should be compared with figure 4.1, which contains the lowest Reynolds numbers. An obvious difference is the rate at which the domains coarsen, decreasing viscosity has increased the particle mobility (recall the prefactor for linear growth in equation (3.22) goes as $1/\eta$). A more subtle difference lies in the topology of the domains, careful examination suggests that for the high Re case, the structure exhibits fewer necks (or handles) than the case for low Re. This hints at a mechanistic difference between the two; possibly the high Re run is starting to be affected by turbulence.

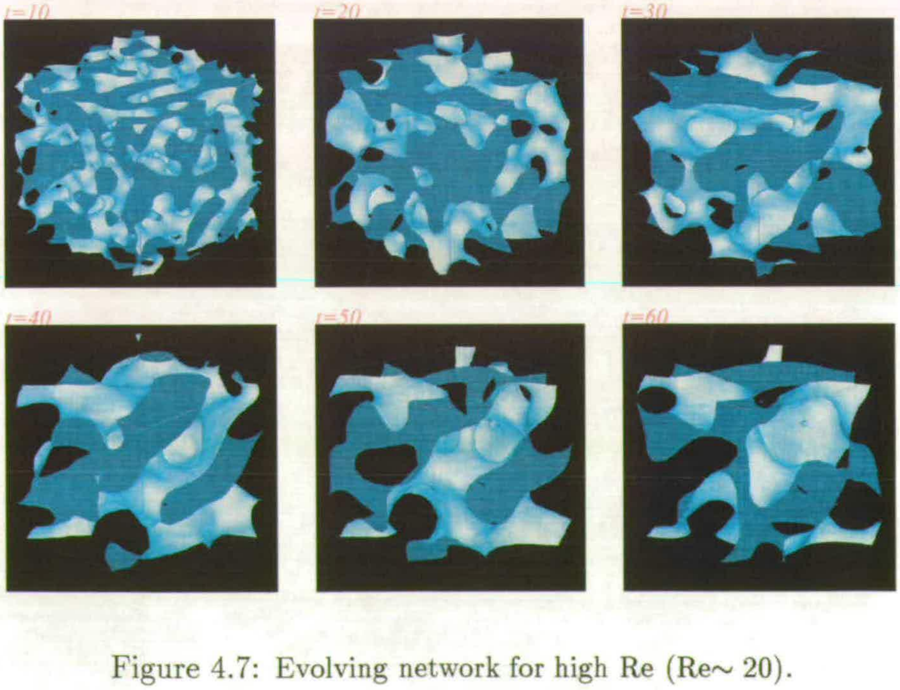

Figure 4.7: Evolving network for high Re (Re~ 20).

Figure 4.8 is a representation of the velocity field of a single species at low (Re $\sim$ 4) and high (Re $\sim$ 20) Reynolds numbers. Streamlines have been drawn using a Runge-Kutta integrating scheme, these streamlines represent the paths that actual particles follow within the structure. Since only one species is shown, there are holes in the map were the second species would be located. In extracting this map a $32 \times 32 \times 32$ grid was used, the velocity of all the particles within a grid box was averaged, this quantity was then further averaged over 200 timesteps. The lengthscale, as measured from the structure factor, is equal to 20 units in each picture (in units of interaction length); however, crucially, there is a marked difference in the velocity maps. At high Reynolds numbers (figure 4.8(b)) the flow is markedly less laminar than at low Reynolds number. For viscous ($n = 1$) scaling, flow must be laminar. The fact that there is a noticeable difference between figure 4.8(a) and (b), suggests that inertial effects are influencing the flow at Re$\sim$20. Experiments on turbulent flows suggest that fully developed turbulence starts to appear at Reynolds numbers, Re$\sim 10^3$ [65–68]; these experiments were carried out on flow within a pipe, but it is not expected that Re for spinodal turbulence would be significantly different. In light of this it is not surprising

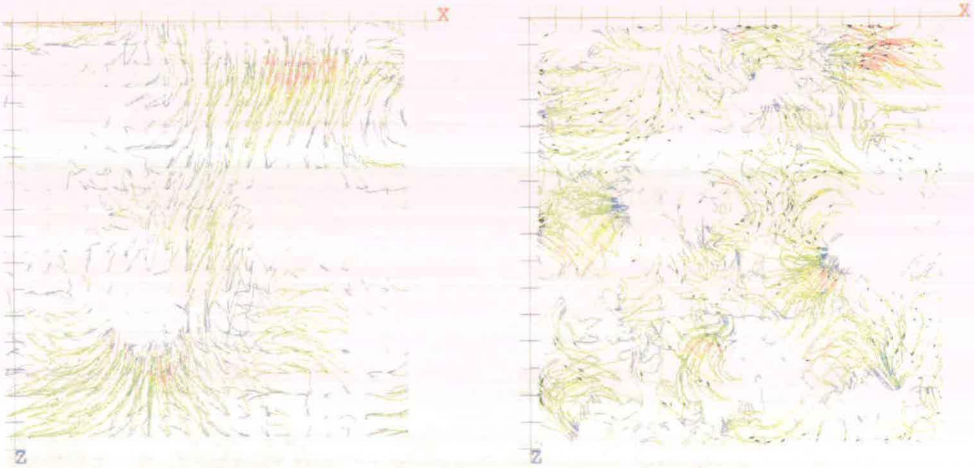

Figure 4.8: Streamlines showing the velocity of a single component. (a) For low Re (~ 4). (b) For high Re (~ 20) the structure is less laminar, an indication that inertial effects are influencing the flow.

that figure 4.8(b) does not show fully developed turbulence.

If Re could be further increased, pushing the system into the inertial regime, the behaviour of the fluid becomes unclear. It is possible that turbulent eddies are formed within the domains: such eddies would offer increased resistance to bulk fluid flow, and therefore slow down the coarsening process. In a recent paper [69] it is argued that at large enough Re, turbulent remixing of the interface will limit the coarsening rate to $n = 1/2$. It should be possible to detect such a mechanism (if present already at Re~ 20) by either looking at the velocity field, or by comparing it with the statistical signatures of a turbulent velocity field, which have been calculated from direct numerical simulation of the Navier Stokes equation. Unfortunately, since the velocity data generated by the current DPD simulations has a large a random component an informative comparison cannot be made. For lattice Boltzmann work on this see [26].

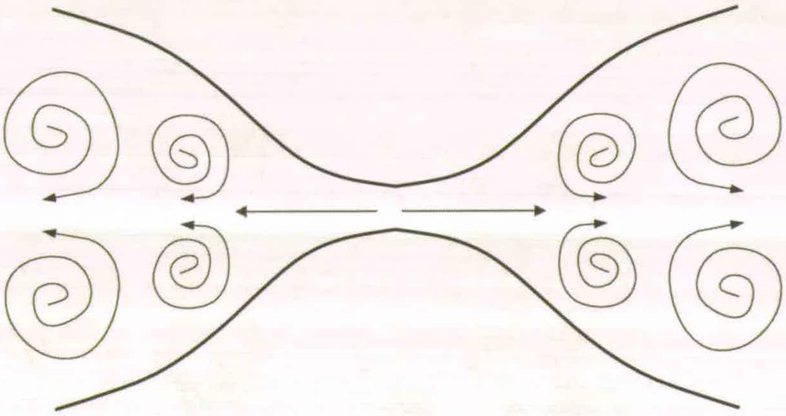

Figure 4.9: Spinodal turbulence: a speculative mechanism for fluid motion in the intertial hydrodynamic regime.

Chapter 5

Qualitative Tests: dynamic scaling

In this chapter the predictions for power law growth in spinodal decomposition of a symmetric binary fluid are rigorously tested. It is found that the scaling hypothesis holds for the structure function over approximately two decades of reduced time. Domain size is shown to increase linearly with time although the prefactor to linear growth apparently does not scale; this may imply a breakdown of the scaling theory presented in Chapter 3. Various explanations for this breakdown are investigated: we argue that molecular physics may remain an important factor even at late times, and show how this may lead to a non-universal prefactor.

In this chapter T stands for the time, previously denoted t. The symbol t will be reserved for a reduced time variable defined below; temperature, when needed, will be called $\mathcal{T}$

5.1 Reduced units

Data taken from simulations is typically quoted in units which are based on parameters specific to the particular technique used. For example, in DPD simulations the cutoff in the interparticle potential can be used to define the unit of length; a physical time unit can be defined by setting the root mean square thermal speed to be $\sqrt{3}$, the mass of a particle defines the mass unit. Using simulation based units is unsatisfactory for two reasons. Firstly, measurements taken from different simulations are expressed in different units and may not be directly compared. Secondly, simulation units will, in general, have no relevance to the underlying physics of the problem.

So what units should be used? The physics of spinodal decomposition involves capillary forces, viscous dissipation and fluid inertia. Assuming the theory of Chapter 3 is complete, no other physics enters the problem and so the only relevant fluid properties are ρ, σ and η. It seems reasonable to try and construct a system of units based around these parameters. This can be done rather easily by combining appropriate powers of ρ, σ and η to form three quantities with the units of length, time and mass

$$L_0 = \frac{\eta^2}{\rho\sigma} \qquad T_0 = \frac{\eta^3}{\rho\sigma^2} \qquad M_0 = \frac{\eta^6}{\rho^2\sigma^3} \tag{5.1}$$

these are the only combinations of ρ, σ and η with the appropriate units[1]. Expressing L and T in terms of L_0 and T_0 allows a direct comparison to be made between the data of any system, regardless of whether it is taken from experiment, simulation or theory. These scalings may be applied to any problem, with the proviso that all the relevant physics enters the problem via ρ, σ and η, as is assumed to be the case for late stage spinodal decomposition.

Note that care must be taken to ensure, L, T, ρ, σ and η are measured in the same units; the dimensions of η are $[\eta] = [M]/[L][T]$, the same $[M]$, $[L]$ and $[T]$ must

---

[1] The mass sale M_0, does not enter into the spinodal problem, it is included here for completeness only.

be used in measuring L, T, ρ and σ. Reduced lengths and reduced times are then defined by $l = L/L_0$, $t = T/T_0$; although these quantities have no dimensions, they are associated with length and time. Remember that in this chapter L and T stand for length and time in DPD units, l and t are in reduced units.

In this notation the Reynolds number (which expresses the ratio of the inertial to viscous force) is written $\mathrm{Re} \equiv Lv\rho/\eta$. The velocity v is some characteristic velocity of the flow such as the rate of domain growth $\dot{L}$, thus $\mathrm{Re} = L\dot{L}\rho/\eta = l\dot{l}$. For the viscous scaling regime, $l = a + bt$ and so $\mathrm{Re} = b^2t$.

5.1.1 Scaling in reduced units

All deeply quenched, incompressible, symmetric binary mixtures undergoing spinodal decomposition contain a growing lengthscale. If such systems are all equivalent at late times[2], the lengthscales may be described by the same master curve when measured in reduced units. This curve has the general form[3]

$$l = a + f(t - t_0) \tag{5.2}$$

the offsets a and t_0 allow for early time diffusive growth; such growth is not allowed for by the definition of L_0 and T_0. To include diffusive growth would require L_0 and T_0 to depend functionally on the transport coefficient λ; these definitions would then become ambiguous since the extra parameter would allow many lengths and many times to be defined.

After crisp interfaces have formed, growth enters one of the hydrodynamic regimes. If the scaling hypothesis is correct then the late time asymptotes of f are,

$$f \rightarrow bt \quad ; \quad t \ll t^* \tag{5.3}$$

$$f \rightarrow ct^{2/3} \quad ; \quad t \gg t^* \tag{5.4}$$

---

[2] *i.e.* all the physics is contained in η, σ and ρ alone

[3] In fact $l - l_0 = f(t)$ might also be chosen. In any linear scaling regime, $f(x) = x$, these are equivalent.

where the amplitudes b and c should be universal, as must the crossover time (defined *e.g.* by the intersection of asymptotes on a log-log plot). Here, the crossover has been defined in terms of a reduced time t^*, in Chapter 3 it was defined as a real length: the two approaches are completely equivalent. These predictions are examined in the following sections, how well they are borne out is a direct reflection of how applicable scaling arguments are to spinodal decomposition.

Lurking within this problem are three dimensionless constants, b, c and t^* the values of which are universal and unknown; scaling arguments and dimensional analysis offer no clue as to their values. Their origin lies in the equations for the magnitude of the forces appearing in the hydrodynamic equations (3.19) and (3.20), together with the form of the driving force. These equations should have prefactors multiplying the right hand side, and it is combinations of these prefactors which gives a, b and t^*. Without these constants, the crossover would be expected to take place at $l = t = 1$ since the scaling length L_0 and time T_0 are the same as the crossover length and time.

The following sections present results taken from simulations performed on fully symmetric, deep-quenched, incompressible binary fluid mixtures. Section 5.2 presents results of small-scale simulations performed on a workstation. Section 5.3 analyses the results of major large-scale simulations performed on a Cray T3D parallel machine.

5.2 Preliminary small-scale Simulations

There are three control parameters for this problem, ρ, σ and η; $k_B\mathcal{T}$ is set to one (this defines the units of energy for the fluid), which is well below the critical temperature for all the parameters used here, Appendix B gives an estimate for $k_B\mathcal{T}_c$. Choosing values for ρ, σ and η is all important in determining whether or not a hydrodynamic regime will be found: the wrong choice may result in diffusion dominating growth up to the finite size cutoff. To narrow down the parameter

identifier	ρ	η	σ	N	γ	AA	AB
S1	3	1.0	2.93	50000	2	20	60
S2	3	1.3	1.67	30000	22	20	40
S3	3	1.5	1.74	50000	30	20	40
S4	3	3.5	2.8	100000	50	20	60

Table 5.1: Physical and simulation parameters used for the initial set of small-scale workstation simulations (N is the number of particles in the simulation). They are based on those presented by [43], viscosity has been increased (by raising γ) in an attempt to induce viscous scaling. Here AA and AB refer to the value of the conservative term in the DPD interaction (this is the α coefficient in equation (1.5)), γ is the dissipative coefficient. DPD units are used here.

space, several small-scale workstation runs were performed, reducing the risk of wasting valuable Cray time. The results from these small-scale simulations are analysed here.

As an initial choice it seemed sensible to use parameters based around those appearing in the original paper on DPD [43]. As demonstrated earlier, there are two hydrodynamic regimes, viscous and inertial, the viscous regime is predicted to occur at smaller lengths and times than the inertial, and should consequently be easier to access. To reduce the danger of inertial effects obscuring a linear regime, the viscosity was increased by increasing the dissipative coefficient γ. The parameters used are given in table 5.1. These parameters exhibit poor scaling, two measurements show this; first the radially averaged structure factor $S(k)$ was calculated (for the definition of $S(k)$ see appendix A). Scaling implies that the evolution in time of $S(k)$ may be described by a universal function $F(kL) = S(k)/L^3$ and a single (growing) lengthscale $L(t)$. We choose to define the lengthscale via the first moment of $S(k)$ as $L = (2\pi)\left(\int kS(k)dk / \int S(k)dk\right)^{-1}$. The best of these preliminary simulations is S4, the results for which are presented in figure 5.1. Figure 5.1(a) shows the growth (in reduced units), clearly growth is still diffusive, as shown by the 1/3 power law; at long times, clear finite size

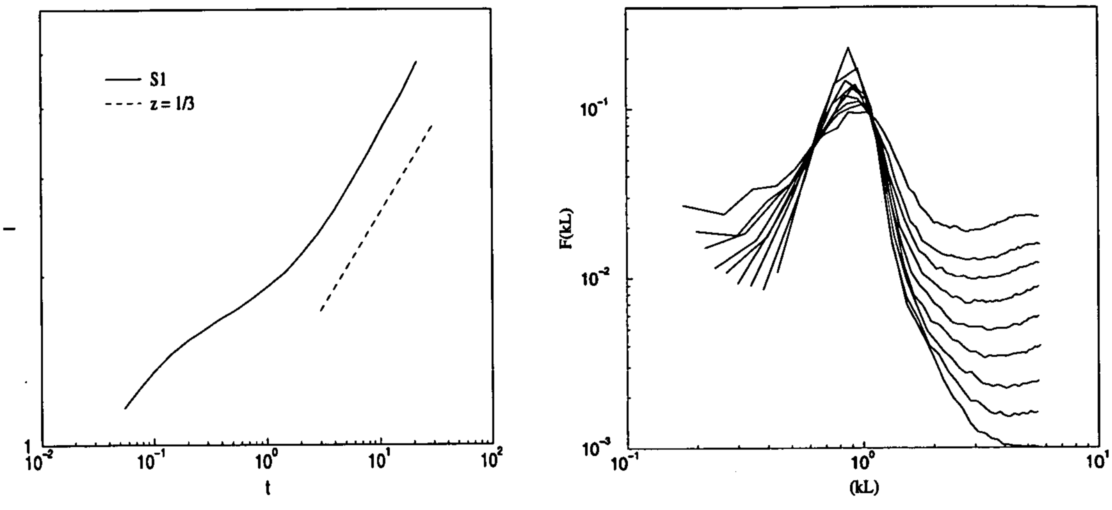

Figure 5.1: Scaling using the parameters of S1. (a) After a short initial transient, the lengthscale increases with a power of 1/3, indicating diffusive growth. The dashed line indicates power law growth with power of 1/3. (b) The structure factor exhibits poor scaling throughout the growth.

effects emerge, these are not plotted. Figure 5.1(b) shows the scaling collapse of $S(k)$. The best collapse occurs around the peak, as it must, but even here it is poor; at large (kL) it is particularly bad, implying that there is another (smaller) lengthscale important in describing the structure.

It would appear that for these parameters diffusion remains an important factor throughout the simulation (note that, in principle any set of parameters will show all three regimes, provided the domain size can grow large enough; problems arise since the finite system size provides an upper limit to l).

So what can be done to improve the choice of parameters? Before moving to a larger system, we decided to broaden the range of the viscous scaling regime even further by increasing the viscosity. The approximate expression for the viscosity, equation (1.11), is linear in γ and quadratic in the density, therefore η will be more effectively increased by increasing ρ. Increasing the density may also have the adverse effect of increasing the effect of inertia; the crossover between viscous and inertial behaviour is predicted to occur at, in DPD units $L^* = \eta^2/\rho\sigma$. For the parameters in table 5.1, $0.11 \leq L^* \leq 1.46$, this appears to suggest that any length greater than 1.46 should enter inertial scaling. However a dimensionless prefactor is involved in the definition of L^*, the value of which is unknown; this prefactor is increasing the actual value of L^* by at least one order of magnitude. This being the case there is no immediate worry that inertial behaviour is affecting growth, so the next set of runs were conducted with increased density $\rho = 10$, the parameters are given in table 5.2. With the exception of S14 all of the curves

identifier	ρ	η	σ	N	γ	AA	AB
S11	10	12.6	41.0	50000	30	20	60
S12	10	7.8	31.6	70000	30	5	100
S13	10	10.8	30.8	100000	40	5	70
S14	10	8.1	23.4	100000	30	20	40

Table 5.2: Physical and simulation parameters chosen for the second batch of small-scale simulations. DPD units are used here.

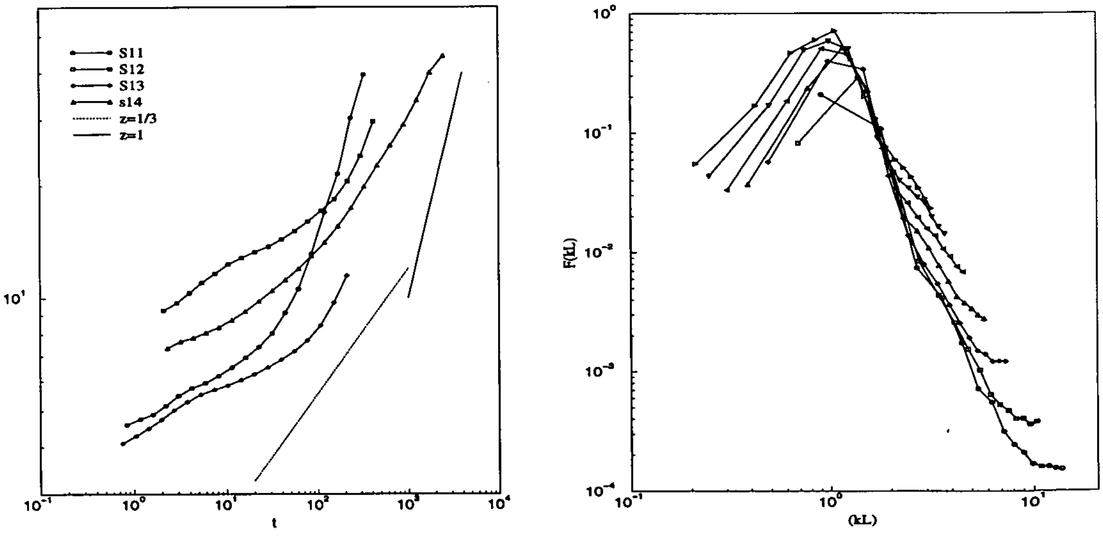

Figure 5.2: Third set of parameters tried. (a) Growth of the lengthscale $l(t)$, all but one of the curves shows an exponent greater than 1/3. (b) Collapse of $S(k)$ for the best linear portion of S11.

in figure 5.2(a) show a growth exponent greater than 1/3. In S14, the diffusion remains important throughout, this is attributed to a low surface tension (relative to the other runs); both of the hydrodynamic regimes require σ, the driving force, to be large. Of the remaining 3 runs, S11 shows the clearest period of linear growth, the structure factor scaling for the linear portion of S11 is given in figure 5.2(b).

The collapse of $S(k)$ is considerably better than that of figure 5.1(b), given this and the linear growth, one may conclude that at the late times S11 is close to, if not already inside the regime of viscous scaling. In the next section the parameters of S11 are applied to large-scale simulations.

5.3 T3D Simulations

The data from S11 showed the longest period of t^1 behaviour, the same parameters were used with an increased surface tension (since this appears to hasten the onset of viscous growth) in the first simulation on the Cray. Domain size showed a clear period of linear growth, extending over roughly 40 reduced time units (see figure 5.3(b) below). Viscosity was then reduced by lowering γ in steps of 5, a final run used $\gamma = 1$. The values $\gamma = 30$ and $\gamma = 1$ define the limits over which γ may be varied. These limits arise from a prohibitively large computation time at high γ (on the serial machine $\gamma = 50$ could be used since computer time was unlimited), and a physical limit on the viscosity at low γ (reducing γ below 1 does not reduce the viscosity, since there is a small but finite contribution to η from the conservative forces [37]); all other parameters where held fixed, a complete list is given in table 5.3. The results from these runs will be shown to call into question commonly held views concerning dynamical scaling; it is therefore appropriate to discuss, and rule out, possible sources of error before proceeding with the analysis.

identifier	η	γ
P30	12.2 ±0.5	30
P25	9.8 ±0.2	25
P20	8.2 ±0.2	20
P15	6.2 ±0.3	15
P10	4.6 ±0.1	10
P5	3.5 ±0.2	5
P1	2.6 ±0.4	1

Table 5.3: For the large-scale runs only the viscosity was allowed to vary. In all runs $\rho = 10$, $\sigma = 50.6 \pm 0.2$, $N = 10^6$, $AA = 20$ and $BB = 100$. The errors are taken from long runs performed purely to measure viscosity or surface tension on a workstation.

5.3.1 Effects of finite system size

There are two distinct types of finite size effects which must be considered. Firstly the motion of a domain sets up a hydrodynamic flow field which propagates throughout the system. After a given time, when the domains have some average size L_H, they will start to be influenced by the flow field set up by their own periodic image; this may influence the subsequent domain growth in an unphysical way. The second effect reflects the fact that the domains cannot grow larger than the system size; in fact, given a conserved order parameter, they cannot grow larger than half the system size[4]. This effect will start to influence growth when L is greater than a structural cutoff length L_S. The lengths L_H and L_S depend on the size of the system, Λ, in some complicated way, and care must be taken that only data with L smaller than both L_H and L_S is used in any analysis.

---

[4] There is an apparent contradiction here since figure 5.3(b) clearly measure L to be well in excess of half the box size. In fact the definition of L used here is only proportional to the *actual* domain size, appendix A shows that for a completely separated system $L \sim \Lambda$, where Λ is the linear extent of the system. Therefore L may be greater than $\Lambda/2$ without violating the structural constraint.

An estimate of L_S may be extracted by examining the effects of halving the system size, this was done using the parameter set of p30 with $\Lambda = 23$ and $\Lambda = 46$ (particle number is increased to keep a constant density). The results are plotted in figure 5.3(a). The two curves do not fall on top of each other exactly, this reflects the system's sensitivity to initial conditions (the initial set of particle positions and velocities, chosen at random). This failure to line up exactly is not important, in the subsequent power law analysis all offsets will be removed: the important quantity is the growth rate, which is given by the gradient of the lines, and is almost identical at early times for both system sizes.

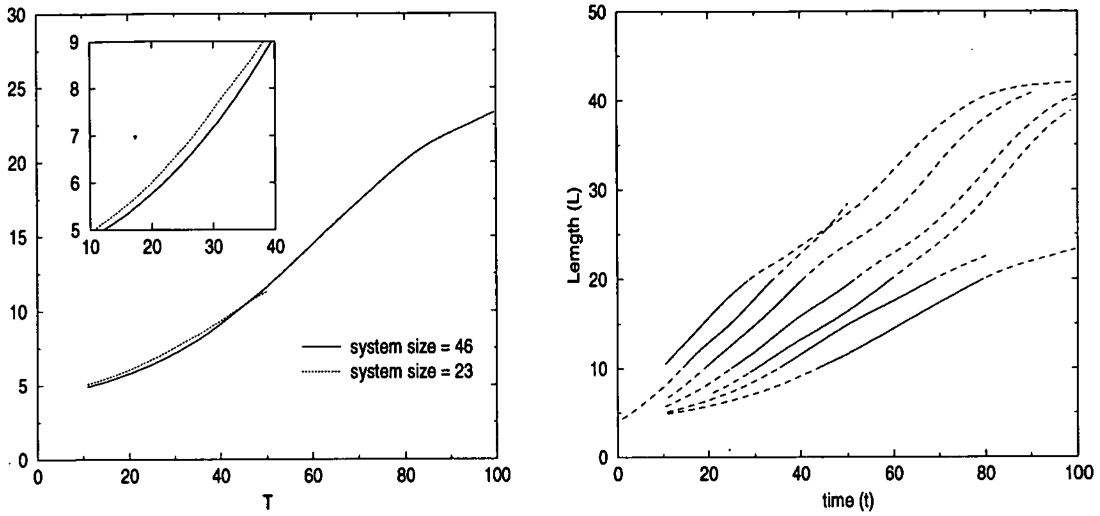

Figure 5.3: (a) Test to see if the growth is sensitive to initial conditions of the velocity. (b) Unscaled DPD data; Lvs.T for viscosities (left to right) $\eta = 2.6, 3.5, 4.6, 6.2, 8.2, 9.8, 12.2$. The datasets for $\eta = 6.2, 9.8$ are averages of two runs.

An estimate of L_S for the smaller system is the length at which the gradients of the two lines deviate. In DPD units this length may be read from figure 5.3(a) as $L_S \sim 10$, doubling this gives the finite size cutoff for the larger system $L_S \sim 20$. Little may be said regarding the value of L_H, doubling Γ may only have a slight effect on L_H. It is, however, encouraging that below L_S the curves show identical growth, this would suggest that any hydrodynamic anomalies arising from finite system size are negligible for $L < L_S$.

5.3.2 Data selection

For all runs conducted at $\Lambda = 46$, data with $L > 20$ may therefore be subject to significant finite size effects and must be excluded from the subsequent analysis. Also excluded is the "early stage", diffusive, portion of each run; this may be judged by eye from the shape of the $L(T)$ plot. (Possible resulting bias is considered below; little would be changed if a sharpness criterion of the observed interfaces was applied instead.)[5]

The datasets for $L(T)$ (DPD units) are presented in figure 5.3(b). Excluded early time data are shown dotted, as is data for $L \geq 20$. Slight wobbles in the fitted parts of the curves represent sampling errors in L arising because L/Λ is not small; these vary between duplicate runs and appear distinct from the direct finite size (saturation) effects arising for $L \geq 20$. Limited computing resources meant that, for each data set at most two runs could be completed (runs p15 and p25 were duplicated and the results averaged). Although this is not necessarily sufficient for good statistical averaging, figures 5.3(a) and 5.4 together with duplicate runs

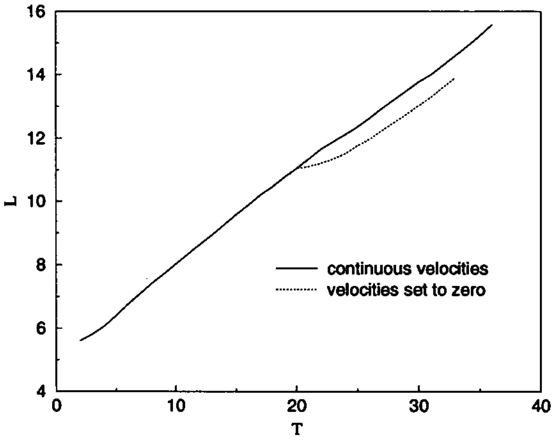

Figure 5.4: Test for the effect of initial velocity; halfway through a simulation, the velocities are set to zero.

---

[5] Note that, since most of the plots in figure 5.3 show upward curvature at early times, the elimination of early time data will bias *downward* any estimate of the quantity $z = d\ln f/d\ln t$ (a true or effective scaling exponent).

for other parameter sets (not shown), show that statistical errors have a small effect on the offset a and negligible effect on the gradient b. The portions of the curves shown solid in figure 5.3(b) were deemed "good" and retained for subsequent analysis.

As a further test of initial conditions, figure 5.4 shows what happens when the velocity of every particle is set to zero at $T = 20$ (the parameters for this run are $N = 50000$, $\rho = 3$, $\gamma = 1$). After a period of ~ 5 time units, the gradient (the velocity of the interfaces) is restored. From this one may conclude that the rate of coarsening is not sensitive to the initial choice of velocities.

5.3.3 Sampling errors in η and σ

The viscosity and surface tension were measured independently in small-scale simulations (N=10000) using the appropriate parameters. To measure viscosity, a single phase fluid is sheared using Lees-Edwards boundary conditions (see Chapter 2), viscosity is then directly related to the off-diagonal components of the pressure tensor [31]. This procedure enables the viscosity to be calculated at every timestep.

Similarly the surface tension may be measured by initialising a system containing a flat interface then extracting the surface tension σ from,

$$\sigma = \frac{1}{2A}(2V_{yy} - V_{xx} - V_{zz}) \tag{5.5}$$

$$V_{\alpha\beta} = \sum_{i=1}^{N}\left(\frac{v_{\alpha i}v_{\beta i}}{N} + \sum_{j\neq i}^{N} F_{\alpha ij}r_{\beta ij}\right) \tag{5.6}$$

again this gives the surface tension at every timestep which fluctuates around a mean value. [6]Here $v_{\alpha i}$ is the component of velocity in the α direction of particle i and $F_{\alpha ij}$ is the difference in the α component of the force between particles i and j, similarly $r_{\beta ij}$ is the difference in the β component of position.

---

[6] In this context σ refers to the surface area not the coefficient of the random term in the DPD equations.

To extract the actual η and σ quoted here, an average was taken over 200 different timesteps, each separated by a period of 50 timesteps (this is sufficient to ensure the readings are uncorrelated), all this after an initial period of 2000 timesteps equilibration. The error on this quantity is calculated as the standard error on the mean $s_m = s/\sqrt{m-1}$, where s is the usual standard deviation and m is the number of independent (uncorrelated) measurements. This gives errors which have, virtually, no effect on the position of the curves.

5.4 Structural scaling

5.4.1 The structure factor

Section 5.2 presented evidence for scaling in the data set S11. Compare the collapse in figure 5.2(b) with that of the large scale runs, shown in figure 5.5. It is clear that the small-scale run does not have the quality of scaling seen in the larger systems, where there is exceedingly good collapse over data which spans 2 decades in reduced time (the small-scale run spans less than half a decade in reduced time). Only the data deemed *good* by the criterion of the previous section appears in the following discussions (this is the solid portions of the curves in figure 5.3(b)). The exact shape for $F(kL)$ constitutes a field of study in itself. Various power laws have been postulated to describe the curve at different values of (kL); at present there is no single coherent theory that explains the entire shape [70,71]. This work falls outside the remit of this thesis, as such it will only be touched upon here.

There is a $(kL)^4$ increase for $(kL) \leq 1$. This has been seen experimentally in polymer blends [72, 73] and is predicted by Furukawa [70]. Furukawa claims that for small (kL), $(kL)^4$ should be seen whenever the effects of surface tension dominate over the thermal noise. Thus the appearance of $(kL)^4$ indicates that the growth has left the early stage diffusive regime and well defined interfaces have

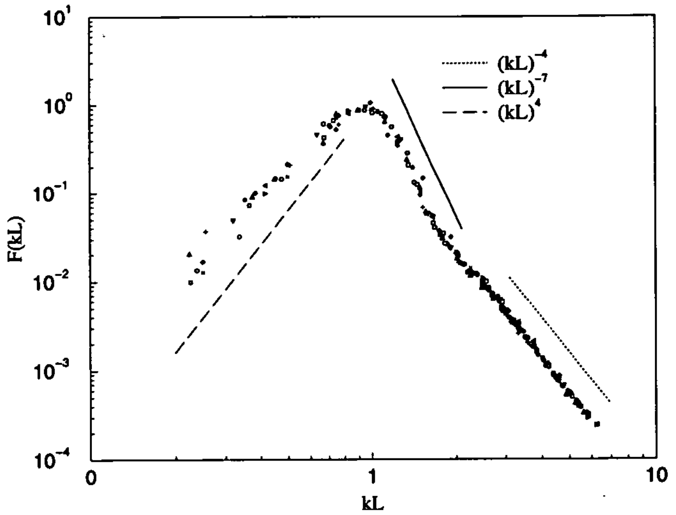

Figure 5.5: Collapse of S(k) in the hydrodynamic scaling regime, data is taken from the large scale runs. For each simulation, two scaled structure factors are plotted; one from the start of linear scaling and from the end of linear scaling. This gives a total of 14 separate data sets, altogether they cover 2 decades of reduced time.

formed. There is a peak at $(kL) = 1$; experiments have reported both $(kL)^{-6}$ and $(kL)^{-7}$ power law behaviour immediately after the peak [71, 72, 74]. Furukawa suggests the actual value to be somewhere between the two: a value closer to $(kL)^{-7}$ is seen here. There is a shoulder at $(kL) = 2$ before the asymptotic $(kL)^{-4}$ Porod tail begins, the presence of this tail indicates well defined interfaces.

For the purposes of this work, the important feature of this graph is the excellent collapse shown by $S(k)$, over 2 decades of reduced time. This allows one to be fairly certain that a single lengthscale, related to the average domain size, is dominating the structure. Power law growth and the existence of viscous and inertial regimes follow from this.

5.4.2 Euler number scaling

As further evidence for scaling, a second quantity associated with the structure, was studied. The Euler number ξ is a topological invariant which may be defined by $\xi = V - E - F$, where V, E and F represent the number of vertices, edges and faces in a discrete triangulation of the structure [75]. The value of ξ is directly proportional to the number of handles, g, within a structure, $\xi = 2(1-g)$. A handle can be thought of as a hole in a 3 dimensional object, see figure 5.6.

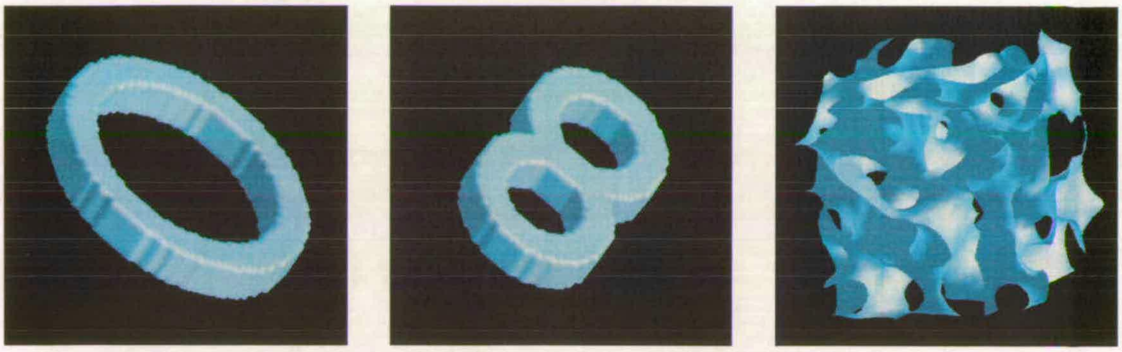

Figure 5.6: What is a handle? (a) a doughnut has a single handle. (b) a figure 8 has two handles. (c) the spinodal network has many handles.

Multiplying ξ by $(L/\Lambda)^3$, where Λ is the system size and L is the dominant length (in DPD units), should give a constant throughout the separation. Note that the structure need not be the same in the inertial and viscous regimes, therefore this constant would be expected to drift in the vicinity of a crossover.

To test Euler number scaling, a different characteristic length was chosen from that used in the scaling of the structure factor. The length used here is obtained from the interfacial area, making this test completely independent of the structural test based around $S(k)$. The quantity which is plotted is then

$$\xi_0 = \frac{\xi V^2}{A^3}$$

where V is the total system volume and A is the area of the interface. As can be seen from figure 5.7, the Euler number is approximately constant over the 2 decades studied. The noise in figure 5.7 is much more severe than that in the scaling of the structure factor. If the system were larger then more handles would be present and the self-averaging would be better; indeed the noise increases with time for each data set, since the number of handles is decreasing. Due to the noise

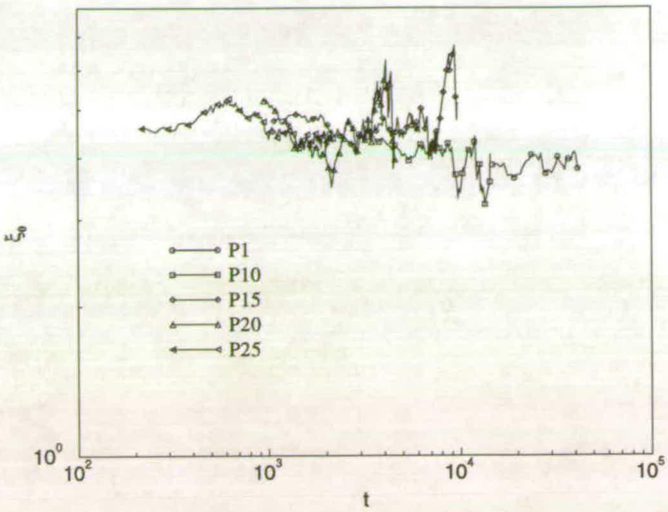

Figure 5.7: The Euler number, scaled by interfacial area as a function of time, ξ_0 is approximately constant over two decades in reduced time. This constitutes evidence for scaling which is independent of arguments based on the collapse of $S(k)$.

in figure 5.7 a firm conclusion cannot be made regarding the scaling of ξ; at best one may conclude that the behaviour of ξ is consistent with that expected from arguments based on scaling. Scaling allows ξ to be non-constant but only in a crossover regime, such as would occur between viscous and inertial scaling. It is possible that our data is in such a crossover and that ξ is slowly varying.

5.5 The Domain Velocity b

Having established good evidence that the structure factor does scale, the massive time range of the data allows a rigorous examination of the scaling predictions for growth of the length scale $l(t)$.

In the viscous regime (equation 5.3), the predicted scaling reduces to $l(t) = a + bt$ where a is a non-universal constant relating to interface formation. This linear law has been reported by several groups [25,76,77] (see also [14,33,78]) but only in two recent cases [34,79] were reliable σ and η values obtained, which are required to find b.[7] In both of these, the offset a was significant, and the linear regime (straight part of the curve at late times) spanned much less than a decade. In reduced units, the data of Ref. [79] describes times in the range $1 \leq t \leq 3$ with a value of $b = 0.3$. However the MD data of Laradji et al [34] has $60 \leq t \leq 140$ and $b = 0.13$.[8]

The disagreement over the value of b (see also [25]) cannot simply be brushed aside, for if dynamical scaling (eq.5.2) applies, and both simulations [34,79] are (as claimed) in the viscous regime (eq.5.3), then these two b values should both be the same. One possible difference is that Ref. [79] describes a relatively compressible fluid. This objection does not apply to the DPD simulations described here for which the relevant ratio (Mach number/Reynolds number) remains small (see Chapter 1). It is thus premature to conclude that any universal regime of viscous hydrodynamic scaling has yet been observed in computer simulations. Analysis of the parallel runs presented here clarifies this important issue by vastly extending the range of timescales explored: the timescales probed here are $750 \leq t \leq 45,000$.

With such a large range of times one might expect that at large time the growth will cross into inertial behaviour, $n = 2/3$. As mentioned earlier, the method of data extraction used here may bias downward any estimate of the scaling exponent. Despite this, only for the two smallest viscosity runs is there appreciable direct evidence for an exponent $n < 1$ as predicted for $t \gg t^*$, see table 5.5.[9] For these runs a fit to eq.5.2 with $f = bt^z$ in fact gives $z = 0.97$ and $z = 0.99$ whereas all the other viscosities give $1.001 \leq z \leq 1.046$. This reduction in z at low viscosities could reasonably be ascribed to statistical sampling errors. The absence of any *a priori* estimate of the statistical errors precludes an accurate

---

[7] In addition to the datasets analysed here, [34] gives several smaller ones from which we have not attempted to extract b values.

[8] In [34, 79] the lengthscale is taken to be the first zero of the pair correlation function. This measure is directly proportional to the measure used here; using a DPD data set the constant of proportionality may be found, thus the data may be compared.

[9] Subsequent LB work [26] indeed shows that t^* is very large.

identifier	η	b	$\hat{\sigma}$
p30	12.2	0.065	0.68
p25	9.8	0.059	0.28
p20	8.2	0.054	1.12
p15	6.2	0.048	0.83
p10	4.6	0.041	3.37
p05	3.5	0.035	5.35
p01	2.6	0.028	10.57

Table 5.4: Values of b and the associated error $\hat{\sigma}$ for a fit to $l = bt$, offsets a have been removed.

identifier	η	b	z	$\hat{\sigma}$
p30	12.2	0.051	1.046	0.34
p25	9.8	0.056	1.004	0.21
p20	8.2	0.054	1.001	1.11
p15	6.2	0.044	1.017	0.38
p10	4.6	0.038	1.009	2.63
p05	3.5	0.046	0.967	6.88
p01	2.6	0.030	0.990	8.92

Table 5.5: Fitting to $l = bt^z$, both offsets have been removed, $\hat{\sigma}$ is the standard deviation of the fit to the actual data averaged over data points.

χ^2 test and the calculation of a goodness of fit factor. In this situation, a good estimate of the quality of the fit is provided by the standard deviation of the data from the fit, this value is denoted $\hat{\sigma}$ in table 5.4, table 5.5 and table 5.6.

Figure 5.8(a) shows fits to $f = bt$ (the fitting parameters are given in table 5.4), the deviations from the data are invisible on this scale. In figure 5.8(b) the data of [34, 79] has been included. Despite showing an excellent fit to $n = 1$ (for all but one of the lines shown), it would be wrong to interpret this data (nor that of [34, 79]) as support for a universal viscous hydrodynamic scaling, equation (5.3). Figure 5.9 shows the fitted b coefficients against the mean time $\bar{t}$, defined by the middle of the fitted section of each run. Obviously, b is not constant as required for scaling, rather, it drifts *systematically* toward smaller values at later times $\bar{t}$, a trend representable empirically as a weak power law, $b \simeq \bar{t}^{-0.236}$.

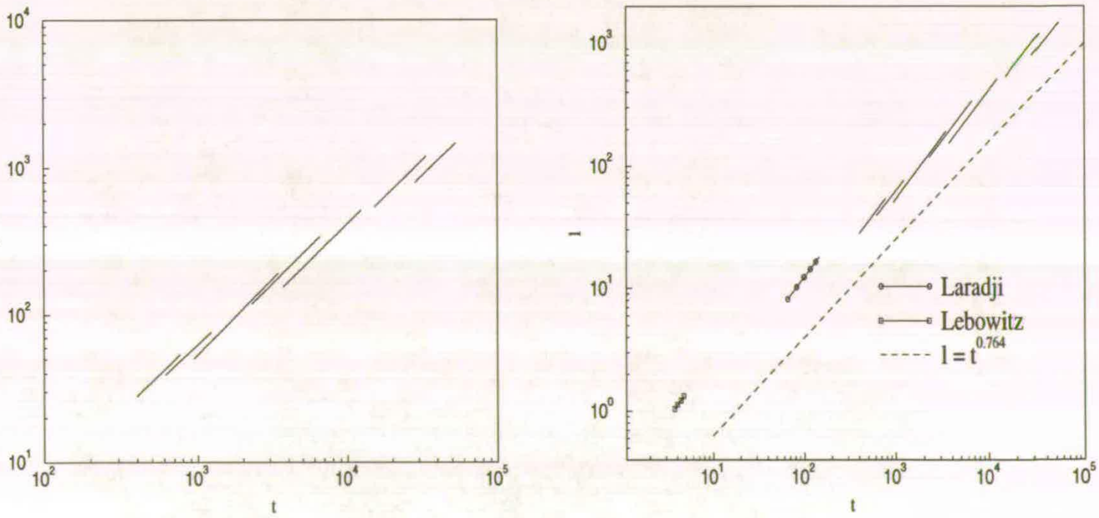

Figure 5.8: (a) The DPD data; from right to left $\eta = 2.6, 3.5, 4.6, 6.2, 8.2, 9.8, 12.2$. The datasets for $\eta = 6.2, 9.8$ are averages of two runs. (b) DPD plus the data of Lebowitz [79] and Laradji [34]. All data has been fitted to a power of 1. Scaling predicts these curves to be colinear; instead there is a systematic drift from left to right as η decreases. This drift would be explained if the real power law was $t^{0.764}$ instead of t^1.

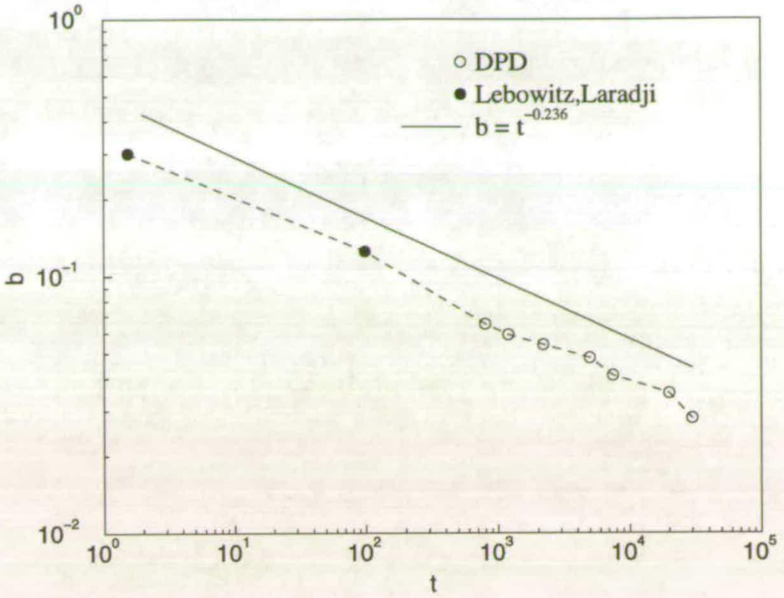

Figure 5.9: log-log plot of resulting growth velocities b against the midpoint of each time $\bar{t}$ for each run. This graph demonstrates that the drift of b is compatible with a power law dependence on $\bar{t}$.

5.6 Interpretation

So, the conundrum is this: if dynamic scaling is true then the value of b should be the same for all runs in the viscous regime. Analysis of the data strongly suggests it is taken from the viscous regime, however the value of b is not constant, it shows a systematic drift with changing viscosity. The following section examines possible ways out of this paradox. Two plausible possibilities exist, *either* the growth is linear; this means b must also be a function of t and b is then non-universal, in violation of the scaling arguments of Chapter 3. Alternatively b is a universal constant and the power is less than one *i.e.* $l \sim t^{0.764}$.

There are other interpretations; conceivably, all the data presented here could be in an (extremely) long crossover regime between viscous and inertial scaling. No predictions exist for domain growth in such a crossover regime, it is therefore possible that a non-universal b and/or a changing exponent may arise. Only by extending the range of lengths and times explored can this hypothesis be ruled out.

Alternatively the whole idea of dynamical scaling for this system could be deeply flawed. This requires that dynamical scaling be cast aside and would be premature since, as is now shown, the impasse may be safely negotiated within the framework of dynamical scaling.

5.6.1 Intermediate power law

Clearly, one would expect to measure $b \sim \bar{t}^{-0.236}$ if in fact one had $f = ct^z$ with $z \simeq 0.764$ (see figure 5.8(b)). No theory predicting this value of n exists in the literature, so it would presumably have to be interpreted as an intermediate, *effective* exponent arising in the crossover region between equations (5.3) and (5.4). Although possible, at least two arguments counter this interpretation. Firstly, the "crossover", if this is indeed what is being seen, must be exceptionally broad. Figure 5.8(b) shows that a single effective exponent governs the entire range of data shown: any "crossover" region covers *four decades* in time[10]. The second reason to doubt this explanation is that for all of the DPD datasets shown in figure 5.8, a fit to $f = b(t - t_0)^z$ yields values of z that are not close to 0.764, but close to (and usually slightly larger than 1.0). Table 5.5 shows parameters obtained by doing this. First the offsets a and t_0 are removed (judged from the criteria of section 5.3.1), then a non-linear curve fitting routine taken from a standard source [80] is used. Clearly the fitted powers are all closer to 1 than 0.764.

To be absolutely certain, a final fit to $n = 0.764$ was performed, the results are shown in table 5.6. Comparing the errors obtained from a fit to $n = 1$ (table 5.4) shows that linear growth with a changing velocity provides a *much* better fit to the raw data than a single prefactor with less than linear scaling.

---

[10] Very recent Lattice Boltzman simulations cast doubt on the validity of the data of Lebowitz and Laradji [26]. Ruling out this data still leaves a crossover lasting two decades.

None of these simulations provides significant evidence of a crossover to an inertial regime; not even that of the lowest viscosity ($\eta = 2.6$). This run covers $20,000 \leq t \leq 45,000$, implying that t^* (the crossover between equations (5.3) and equation (5.4)) is at least as large.

identifier	η	b	$\hat{\sigma}$
p30	12.2	0.231	3.9
p25	9.8	0.249	3.8
p20	8.2	0.243	8.0
p15	6.2	0.241	11.9
p10	4.6	0.257	25.2
p05	3.5	0.253	34.9
p01	2.6	0.247	61.6

Table 5.6: Fitting to $l = bt^{0.764}$, offsets have been removed.

A less extreme number is obtained if one quotes instead the equivalent Reynolds number $\mathrm{Re}^* \simeq b^2 t^*$. (This relation applies because in linear scaling, we have Re $= bl \simeq b^2 t$.) For the middle of the low viscosity run, Re is about 20, so Re^* need not be much larger than this. Given the smallness of the apparent b values, the largeness of t^* follows, as does the failure to observe a clear inertial scaling regime (equation (5.4)) in previous simulations [34].

One must conclude that appealing to an intermediate power, which might exist within an extended crossover region, is an unsatisfactory basis for explaining the data presented above. The question then arises – might there be some other physics, playing a role in spinodal decomposition at late times, which could lead to a violation of the dynamical scaling hypothesis itself? To answer this question it is neccessary to examine all possible sources of differences between each run.

5.6.2 Weak dependence on initial conditions

One possibility is that the late-stage coarsening velocity b depends upon initial conditions, inherited from the non-universal early time dynamics. (For related ideas see [81].) This information would have to reside in either the velocity field itself, or in subtle details of the density distribution. The first of these has been tested numerically by re-initialising the fluid velocity during a late-stage run; no significant effect on b was observed, see figure 5.4. It seems reasonable to assume that the variation in the density field between runs is pretty random and small, it is hard to imagine how this could lead to the systematic drift in b which is observed. Indeed for the two sets of parameters for which duplicate runs were performed, the difference in b is negligible. In fact, within these duplicate runs, the only differences occurred at late times where the self-averaging of the system is bound to be poorer due to a smaller number of domains. One may conclude that explanations based around initial conditions are unlikely.

5.6.3 Influence of a molecular lengthscale

A more plausible mechanism for the observed non-universality of the velocity b could arise from the direct intrusion of physics that the dynamical scaling hypothesis excludes. Thermodynamics (*e.g.* finite temperature or compressibility) cannot be solely responsible, since all the DPD runs have the same conservative forces, thus they are *identical* thermodynamically. Perhaps the most interesting possibility is that late-stage spinodal decomposition involves a molecular (or, in simulations, discretization) lengthscale which could enter during topological reconnection or "pinch-off" events. In such events, without which coarsening of a bicontinuous structure cannot proceed, a fluid neck contracts to (formally) zero width in finite time.

Recent work on a closely related problem (disconnection of a single fluid domain *in vacuo*) suggests that pinch-off processes need not violate dynamical scaling [82, 83]: the asymptotic behaviour both before and after the pinch have a universal description in l, t variables (measured from the pinch-off event itself). According to this work, molecular physics intervenes only briefly at pinch-off, and is forgotten soon after. It is not yet known whether similar universality can be recovered for fluid-fluid pinch-offs [82,83], but crucially, even in the fluid-vacuum case, such universality is *only* expected for large values of the dimensionless quantity

$$\lambda = L_0/h = \eta^2/(\rho\sigma h) \tag{5.7}$$

where h is a molecular (or discretization) length [82, 83]. For the fluid/vacuum case, Eggers [82, 83] argues that λ is large enough for some fluids ($\simeq 10^7$ for glycerol) but not others ($\simeq 20$ for water), to recover universal behaviour.

If similar ideas govern the fluid-fluid case, and if pinch-off physics remains a controlling factor in late stage coarsening, then a violation of dynamical scaling could be expected for many real fluids. The same applies for any simulation in which λ is not very large. Taking $h = 1$ (for these simulations, the cutoff in the inter-particle potential is 1, so $h = 1$ is a molecular lengthscale) gives values for λ, for the DPD runs, in the range $\lambda = 0.28$ at $\eta = 12.2$ (so that $\bar{t} = 800$) to $\lambda = 0.014$ at $\eta = 2.6$ (so that $\bar{t} = 30000$). The systematic dependence of b on $\bar{t}$ reported above can, for these DPD runs, equally well be expressed as a dependence on λ. The latter would permit an extended form of dynamical scaling, with $f(t)$ replaced by $f(\lambda, t)$ in equation 5.2; at present this cannot be distinguished from a $\bar{t}$ dependence, because the variations made through η affect $\bar{t}$ and λ similarly. A dependence of b on $\bar{t}$ could be distinguished from one on λ by doing larger simulations, systematically varying the particle density, or by using different simulation methods to address the same range of t. (The latter is work in progress [26].) No direct comparison with [34,79] can be made, since the definition of h must depend on the simulation method; but taking h as the mean interparticle spacing, one can estimate that $\lambda \simeq 1.7$ for the data of Ref. [34] and $\lambda \simeq 50$ for that of Ref. [79].

5.6.4 Dangerous finite-size effects

It is possible that our criterion for the onset of finite-size effects is not stringent enough (recall that data with $L > \Lambda/2$ was discarded). If this were the case then all the fits presented here would be doubtful, and the possibilty of a universal b within a linear scaling law would be recovered.

Only by increasing the range of lengths and time explored could this question be resolved. Within the DPD framework and with the computing power available, we cannot extend the range presented here. It is up to other simulation methods or subsequent users of this DPD code on a larger machine to extend our data. The most encouraging extension, so far, has been Lattice Boltzmann [26].

5.7 Conclusion

We have put forward four possible explanations for the drift of b. The first relies upon a huge crossover period, spanning 4 decades in reduced time[11], which has its own power law intermediate between viscous and inertial: this seems unlikely on two counts, one—crossovers are seldom so protracted, and two—all the fits performed here favoured a linear power with a drift in b.

The second explanation assumes that statistical errors are to blame, this is always a possibility in any situation where measurements are performed on a thermodynamically small system. However, statistical errors are random in nature, it would be a rather large coincidence if they gave rise to the systematic variation seen here.

Thirdly, there is the possibility of a second, microscopic, lengthscale remaining important and influencing the growth at late stages. In the context of the data shown above this explanation is perhaps the most plausible, especially when one

---

[11] or two decades if the data of Lebowitz and Laradji proves to be unreliable

considers how little the separation between domain size L and interface width actually is.

Finally, the possibility that finite-size effects are influencing our data has to be acknowledged, but we cannot test this on the current machines.

Chapter 6

Surfactants

In Chapter 2 it was shown how the basic DPD model may be extended to simulate dimers in solution. In this chapter the extended code is used to study a dense solution of an amphiphilic species. By varying the volume fraction of amphiphile and the temperature, three distinct phases are identified. Attention is focussed on the smectic (lamellar) mesophase with results for the evolution of a polydomain with and without an external shear flow.

In certain circumstances, it is shown that shear induces a curvature into the smectic layers which fold in upon themselves to form multi-layered cylinders. The tendancy for smectic layers to buckle, after a temperature quench, is observed and identified with the Helfrich instability. Also explored are the effects of shear flow on the isotropic—lamellar phase boundary.

6.1 Introduction to surfactant mesophases

As stated in Chapter 1, when surfactants are placed in solution they will self-assemble into aggregates. The exact form which these aggregates take depends on parameters such as temperature, salinity, external flow, size and concentration of surfactant. The lamellar structure has already been identified in Chapter

1. At low concentration surfactants pack to form micelles—spherical aggregates in which the hydrophobic groups are contained within the centres of spheres; increasing the concentration, a hexagonal phase forms wherein the surfactants exist as cylinders, again with the hydrophobic groups pointing inwards, these cylinders have hexagonal packing. Between the hexagonal and lamellar phases a cubic phase has been seen [3], here the surfactants form a bicontinuous network which spans the system.

6.1.1 Defect structures

The topology of the structures which are formed when an isotropic phase, containing an amphiphilic species, is quenched into a lamellar[1] phase shows several interesting features. For example, the evolution of a lamellar phase can show slow dynamics, typically associated with the sluggish motion of topological defects such as dislocations, domain walls or focal domains. Very often a "polydomain" or "powder" mesostructure is observed, in which patches of well-ordered layers have different orientations; this texture may continue to evolve by the slow migration of the domain walls and any other defects that are present. Applying a shear, even a relatively weak one, can lead to strong changes in the organisation of the defects and domains [84]. This, in turn, affects the rheology and transport properties of the material which are of primary interest in many industrial applications.

6.1.2 Simulation methods

Various simulation methodologies have been used to address the phase equilibria and dynamics of amphiphiles in solution. These range from phenomenological free energy approaches [85] (akin to the Landau free energy approach presented in the context of phase separation in Chapter 3), through Monte Carlo lattice

---

[1] A schematic diagram of the lamellar phase is given in Chapter 1.

models [3] to first principle molecular dynamics [86]. However, the complexity of these systems has meant that few of these methods have been successful in reproducing the coarsening or flow of an ordered phase, such as a smectic, in three dimensions. As discussed in Chapter 1, a lattice gas model, which includes amphiphiles, has been developed and produced extremely encouraging results in two dimensions [16–18].

Any meaningful study must respect the presence of hydrodynamic interactions. These interactions, described in Chapter 1, have their origin in the conservation of momentum; in a liquid crystalline phase the hydrodynamical equations which result, such as the Leslie-Ericksen equations for smectics [87], are extremely complex even for a single species system. For lyotropic (solvent-based) smectics, such as amphiphilic bilayers in solution, the situation is even worse. Although progress has been made solving the hydrodynamic equations perturbatively, for example to study the dynamic structure factor, $S(\mathbf{k},t)$, of a lamellar monodomain [88], there has been little progress so far in numerical modelling of smectic hydrodynamics by conventional continuum mechanical schemes (e.g. finite element) as routinely used for Navier Stokes problems[2].

This impasse can be negotiated in principle by molecular dynamics (MD). The MD technique for a simple fluid has been described in Chapter 1; incorporating a dimer model into MD may be achieved using the constraint techniques described in Chapter 2. Although MD ensures correct hydrodynamics, it is limited to computationally short times and small lengths (see Chapter 1); as yet the computational power is not available to allow a meaningful MD study of the hydrodynamics of bulk smectics.

Since DPD models the solution at a mesoscopic level, and incorporates hydrodynamics, it offers the possibility of realistic simulations over extended time and length scales. For mesophases, an added attraction of the DPD technique over

---

[2] Integration of the Cahn-Hilliard equation and Boundary Integral Methods, both described in Chapter 1, are examples of finite element analysis applied to two phase flows.

continuum methods is that defects, such as domain walls, are included implicitly in the algorithm, whereas these have to be treated as singularities in continuum hydrodynamics. This work is among the first mesoscale modelling of amphiphilic mesophases with full hydrodynamics in three dimensions.

In Section 6.4 the formation and coarsening of a smectic phase after a temperature quench is presented. Then in Section 6.5, results are given for the formation of a smectic under flow (with an otherwise similar temperature quench), also studied is the orientation and reorganization of a large length-scale domain structure, formed without shear, when a shear is subsequently switched on. It is shown (Section 6.9) that interesting layered structures may develop when a shearing force is applied to a lamellar polydomain. Section 6.5.2 examines the effects of a temperature quench on a lamellar phase. Finally in section 6.5.3, the effect of shear on the isotropic to lamellar transition is looked at.

6.2 Minimal amphiphiles in DPD

Amphiphiles will be modelled as dimerized DPD particles (type A and type B) constrained to lie at fixed separation, these particles are in a solvent of monomers (type C). The exact details of the constraining method were given in Chapter 2. For simplicity we take the the A-A, B-B and C-C interactions to be the same (though different from A-B, B-C and A-C). With suitable energy parameters, it is found (in Section 6.3) that this minimal model gives a reasonable phase diagram—in fact, one very similar to a wide range of nonionic surfactants such as $C_{12}E_6$ (albeit without a consolution region in the micellar phase).

It is not necessarily obvious that the dimer model is adequate for successfully reproducing surfactant behaviour. For example, in most lattice approaches it is found that to reproduce the phase equilibria of real surfactants (such as members of the nonionic series C_nE_m, where C and E represent alkyl and ethoxy groups) a larger entity containing several monomers (for example A_2B_3) is required [3].

However, the soft interactions in DPD are intended to reflect some degree of prior coarse graining. Indeed, Groot et al [89] show that much of the phenomenology of block copolymer mesophases (which in reality is observed only for fairly long chains) already appears in DPD for quite small "molecules" such as A_3B_7. Therefore a minimal, dimer model of amphiphiles in solution is worth exploring. Note that we consider only relatively concentrated systems ($0.08 \leq \phi \leq 1.0$, where ϕ is a concentration variable defined by $\phi = n_A + n_B - n_C$); not addressed are the somewhat delicate effects (critical micellization, etc.) that arise at much lower concentrations. It is not clear that the minimal dimer model would give as good a representation of the latter phenomena as it apparently does for mesophase formation.

In previous Chapters, a scaling analysis was presented which involved expressing lengths and times in reduced units based on viscosity, surface tension and density. No such scaling arguments apply to the results in this Chapter; here the units used are based on the DPD algorithm (these are the units, not reduced, in Chapter 5). The length unit is given by the range of the conservative potential, r_c. A physical time unit can be defined for each temperature by setting the root mean square thermal speed to be $\sqrt{3}$. This is tantamount to keeping the temperature fixed and varying the energy parameters instead (see [36]); however, for phase diagram work it is more usual to retain temperature as a variable. For this study the interaction parameters are held constant at $\alpha_{AA} = \alpha_{BB} = \alpha_{CC} = 25$, $\alpha_{AB} = 30$, $\alpha_{AC} = 0$, $\alpha_{BC} = 50$. The overall scale of these is arbitrary; this choice gives phase diagram features lying in a convenient temperature range around $kT \simeq 1$. Unlike spinodal decomposition, a high viscosity and a high surface tension are not required, therefore a high density is not needed and $\rho = 6$ is used throughout this chapter.

These choices leave three physical control parameters: the temperature or thermal energy kT, a composition variable ϕ and the viscosity (or, for a smectic, viscosities) of the fluid; for this Chapter, γ was chosen as $= 5.625$ throughout (corresponds to $\eta = 2.5 \pm 0.2$). Results were taken both from workstation runs

($N = 6000$) and from major runs on the T3D, for which $N = 100\,000$. The former were found adequate for getting a reasonably accurate phase diagram. Two slightly different integration routines were used: the parallel code retains the Euler integrator, introduced in Chapter 1, with a timestep of 0.01. On the serial machine a Verlet type integrator was used [36] with a timestep of 0.05.[3] For a monomeric fluid, this choice gives measured temperatures within 2 percent of the nominal value set by the fluctuation-dissipation theorem, which offers a good compromise between absolute accuracy and computer time.

A comparison between serial and Cray runs, performed on the same system, revealed a small yet significant shift in the position of the isotropic to lamellar phase boundary. Upon investigation it was found that the Verlet integrator, although superior at reproducing the correct translational temperature, was consistently over-estimating the temperature of the rotational degrees of freedom. This was not pursued further, but may lead to small inaccuracies in the phase boundaries, which are already influenced by finite size effects. Instead, the parallel computing resources were devoted to the study of dynamical effects.

6.3 Phase diagram

The simulated phase diagram[4] is shown pictorially in figure 6.1(a). Here we have an array of points indicating the observed state of organization at various compositions ϕ and temperatures T. The state of organization was found by direct visualizations of the configuration such as those shown for five particular parameter sets. For these visualisations, an isosurface was calculated based on the density of tail (type B) particles, this was performed using the *vtk* visualization package [90].

---

[3] For a critical discussion of the integration techniques which may be applied to velocity dependent forces see [44].

[4] This work was carried out in collaboration with Maarten Hagen *et al.* at Unilever Research Port Sunlight [2].

These simulations are relatively small, and some finite size effects do remain. For example in a hexagonal phase, there will be a tendency for the direction of the cylinders to be inclined at a definite angle with respect to the simulation box so as to get a good match between the favoured repeat distance of the two-dimensional hexagonal packing and the periodicity imposed by the simulation. Because a perfect match cannot be achieved (and because a good match is easier to arrange for lamellae than cylinders) there will be some shift in the phase boundaries on moving to a larger system where the mismatch is less. Also, in a few cases there are signs of trapped defects which make unambiguous phase assignments difficult. Nonetheless, the probable location of the boundaries between isotropic, hexagonal and lamellar phases have been deduced from these simulations. A cubic phase, which should perhaps exist between the hexagonal and the lamellar regions at low T, was not seen, although a careful search was undertaken. The resulting phase diagram may be compared with figure 6.1(b) which shows a classical phase diagram for the nonionic surfactant $C_{12}E_6$ taken from [91] (see also [92]). Given the crudeness of the model, this agreement can be considered reassuring. The main omission is the absence of a two phase region at high temperatures in the low density regime; but since the model has no hydrogen bonding, nor any other attractive forces, this is inevitable.

Note that, since a binary system is being considered, the phase boundaries between the various phases should in general be accompanied by miscibility gaps of finite width – for example, one should find a region of ϕ within which lamellar and liquid states coexist. However, it is not surprising that such macroscopic demixing is not observed in simulations of this size, which may not be big enough to contain a well-developed interface between two bulk phases. In any case, for many surfactants, the relevant miscibility gaps are found experimentally to be very narrow; they are not shown at all on many published experimental phase diagrams, including that of figure 6.1(b). This accords with the fact that the various transitions are not strongly first order: there are strong changes in symmetry between the phases, but the difference in local structure either side of the

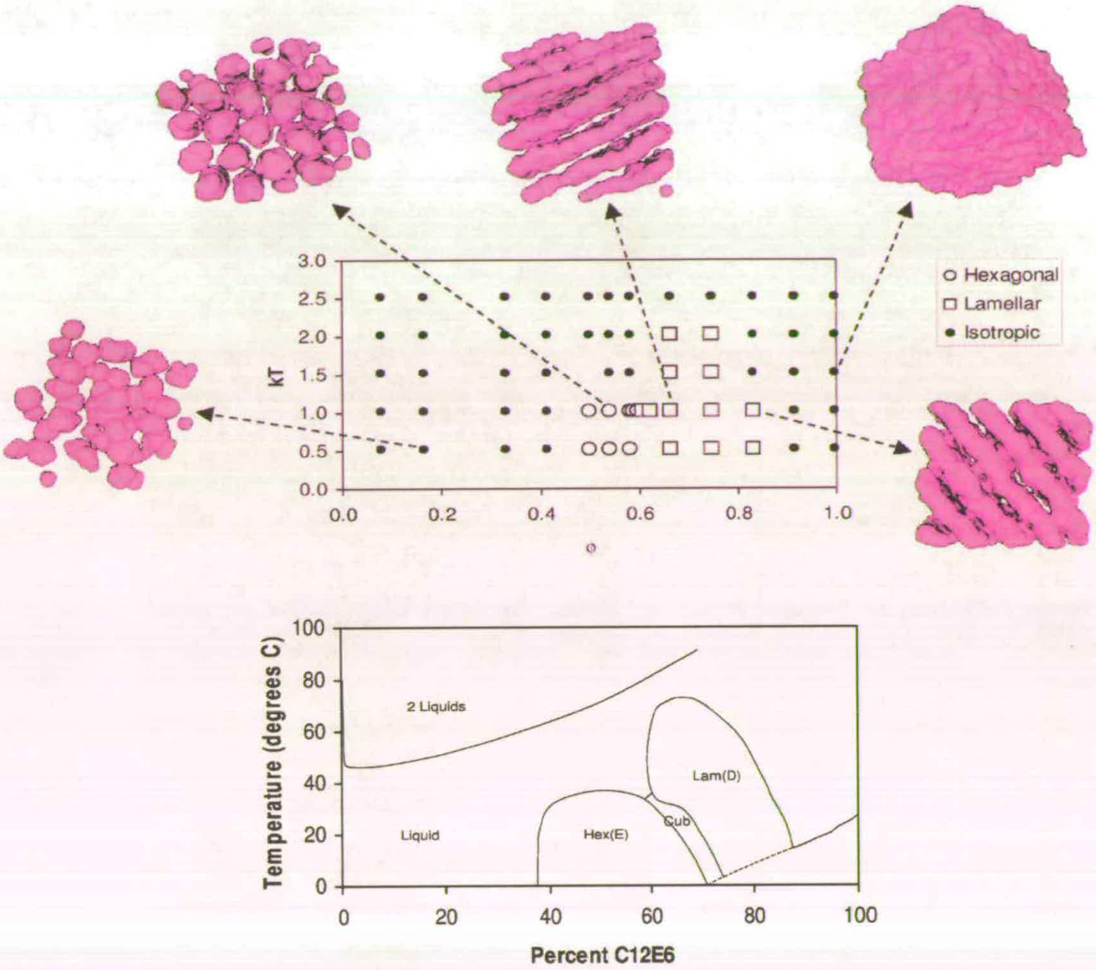

Figure 6.1: (a) top: Phase diagram for DPD dimers. Energy parameters and composition variable are defined in the text. (b) bottom: Experimental phase diagram for a nonionic surfactant, from [91].

phase boundary is not that great.

6.4 Formation of lamellar domains after quench

The dynamic evolution of a quench into a lamellar phase with $\phi = 0.83$, $kT = 1.0$ is investigated here. The initial condition was a random arrangement of dimers and monomers. This was done for a system with $N = 100\,000$ on the

Cray. To monitor the onset of ordering the time evolution of the static structure factor was studied; this is defined as the Fourier transform of the pair correlator $\langle\rho(\mathbf{r})\rho(\mathbf{0})\rangle - \langle\rho\rangle^2$ where ρ is a suitably chosen combination of local densities n_i. For this study we chose $\rho = n_A + n_B - n_C$; the angle averaged structure factor $S(k)$ is normalized so that $S(k \to \infty) = 1$. Obviously, the precise form of $S(k)$ depends on the particular "contrast" selected - in particular, the relative intensities of the various peaks depends on this[5]. The above choice, in which the contrast is between the solvent (C) and the remainder, gives a large value of the first peak in the structure factor. Figure 6.2 shows a comparison of the different definitions considered; the position of the peaks does not vary, however the intensity does. For the choice $\rho = n_B - n_A - n_c$ a secondary peak is not seen at all, and scattering off dimer midpoints does not give a third peak.

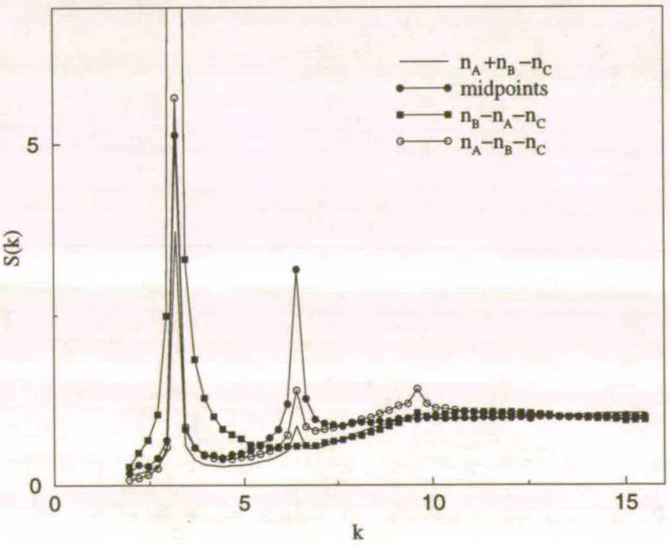

Figure 6.2: The Fourier transform of the pair correlator $\langle\rho(\mathbf{r})\rho(\mathbf{0})\rangle - \langle\rho\rangle^2$, in a phase with smectic ordering, for four different contrasts. The intensity of the peaks depends on the contrast chose, but crucially the position of the peaks does not vary. In the following work, the definition $\rho = n_A + n_B - n_C$ is used.

---

[5] If one considers the scattering object to be a bilayer rather than particles then $S(k)$ becomes the product of a structure factor for the smectic and a form factor for the bilayer. The latter, though not the former, strongly depends on the contrast chosen.

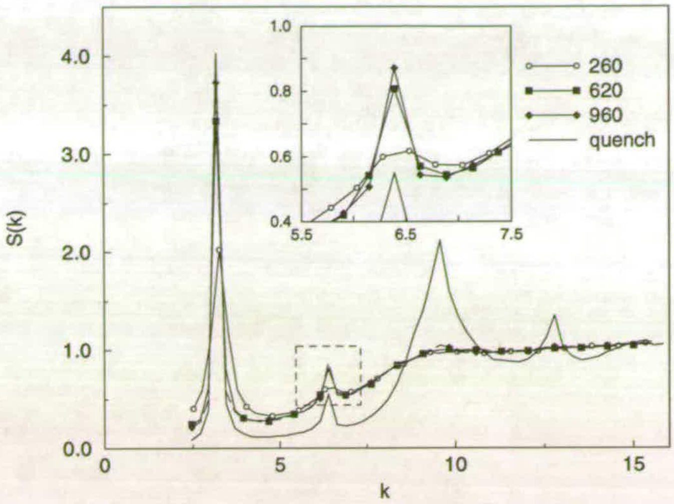

Figure 6.3: Time evolution of the angle averaged structure factor for a quench into the lamellar phase at $kT = 1$. As the layering increases with time, second and third harmonics develop. A final curve (marked "quench") follows a subsequent quench to $kT = 10^{-4}$.

The time evolution of $S(k)$ for a quench into the lamellar phase is shown in figure 6.3; a strong peak corresponding to the repeat distance of the bilayers (at $k = k_{max} = 3.2$) is clearly seen. By time $t = 960$ (DPD units) the structure has almost ceased to evolve; a second harmonic (see inset) is by then clearly visible as well. At this stage a further quench was performed to a very low temperature $kT = 10^{-4}$, and the simulation run on for 200 timesteps (20 DPD time units as defined at the pre-quench temperature). This has the effect of dramatically sharpening the interfacial structure, and was done primarily as an aid to visualization. But note that after this final quench one can detect (even in the angle-averaged $S(k)$) three subsidiary peaks at harmonics of the fundamental smectic periodicity. In principle an analysis of the lineshapes of such harmonics could allow determination of the elastic constants of the smectic phase [88]. However, since the system is not fully equilibrated at its final low temperature ($kT = 10^{-4}$) we do not attempt this.

For real-space visualizations of these datasets, the interface between media is defined by a zero-set of the density difference $n_B - n_A - n_C$. These are specified on a coarse-grained 32^3 grid and the surface plotted using standard interpolation software within the AVS visualisation package. Again there is a degree of choice as to the particular combination of n's used; by trying all possible contrasts, it was found that using $n_B - n_A - n_C$ revealed the clearest structure. Figure 6.4(a) shows the resulting polydomain texture in real space for a time $t = 320$ DPD units after the initial quench. This is compared with the same texture after a period of further evolution followed by a final deep quench. Even at the original quench temperature ($kT = 1.0$) the simulation at this point has almost stopped evolving—it may not be possible for this structure to coarsen further (under periodic boundary conditions) at any significant rate. Figure 6.5 shows the angle-resolved data for this system; the colour reflects the value of $S(k)$ at each point in the (k_x, k_z) plane, red for high and blue for low. It shows that the structure factor remains fairly isotropic until quite late times, consistent with the presence of a polydomain texture.

There are now visible just two large smectic domains connected by a topologically nontrivial domain wall. The large scale topology of this structure is already present at the original simulation temperature and the final quench to $kT = 10^{-4}$ merely serves to sharpen the interfaces. Inspection of the figure 6.4(b) shows an apparent density of "necks" (defects connecting one layer to the next) along some but not all faces of the simulation cell; these are probably an artifact of the visualization software (which does not respect the periodic boundary conditions), and indeed far fewer necks are seen well within the cell. A cut-out taken from the centre of one of the two large domains is shown in figure 6.6; it shows good smectic ordering with a slight twist (and almost no neck defects). Close-ups of the domain wall structure are also presented in figure 6.6; the visualization method is as in figure 6.1.

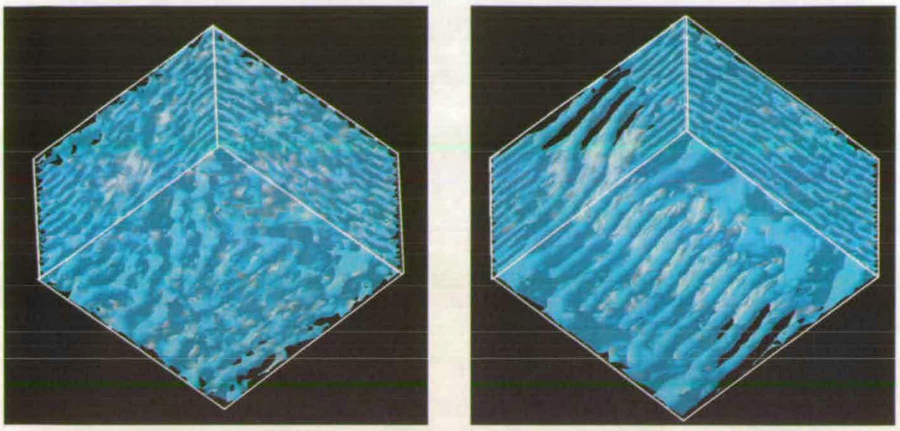

Figure 6.4: A quench from random initial particle positions to $kT = 1.0$ in a system with $\phi = 0.83$. Left: (a) the early time structure has many domains. Right: (b) the late time structure (right) has two. The late time structure has been subjected to a brief further quench to $kT = 10^{-4}$; this is intended to improve the visualisation by sharpening the interfaces.

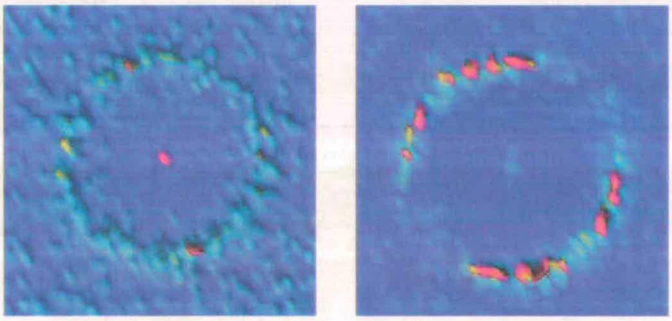

Figure 6.5: At early time (left) $S(k)$ is radially symmetric, this is expected if the system is composed of many domains each having a different orientation. At late time (right), $S(k)$ is not isotropic indicating a preferred layer orientation.

6.5 Flow effects

Two exploratory investigations of flow effects were made using a larger system size on the Cray. In the first, the formation of a lamellar mesophase under ambient shearing was studied: a system of volume fraction $\phi = 0.7$ was quenched into the lamellar phase ($kT = 1.0$), while a steady shear was maintained. The shear rate

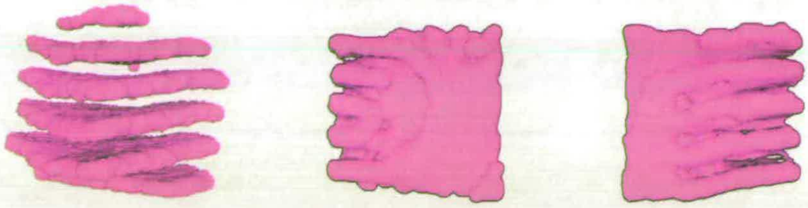

Figure 6.6: Features of the bidomain sample: A well-ordered lamellar section and two parts of the domain wall.

was 0.01 in DPD units, which is small compared to the local collision rates for particles but large compared to the relaxation time for a defect texture of the type shown in figure 6.4 above. Under these conditions, smectic order was rather quickly achieved, leading to a good monodomain sample by about $t = 200$ DPD units; see figure 6.7. The layer normals are perpendicular to the velocity direction (which is unavoidable in a lamellar phase under steady shear) and almost, but not quite, aligned with the velocity gradient. Note that in principle the layer normals could point anywhere on a circle in the velocity gradient/neutral plane, although most theoretical treatments predict one extreme or the other [93, 94].

Once a good monodomain was formed, the shearing was then stopped and the structure allowed to relax for a further long period (500 DPD units) before the structure factor for the whole sample was determined. This structure should thus be an equilibrium monodomain (with the proviso that relaxation of the smectic repeat distance may not be possible even in this time period; the mean layer spacing could still be perturbed by the preceding flow). The resulting angle-resolved structure factor is shown in figure 6.7 for the velocity gradient/neutral plane in reciprocal space. (Note that no further quench was needed in this case; kT is still 1.0.) This shows extremely good ordering with four orders of scattering peak; an angle-average of this structure factor (not shown) is very similar to the $t = 960$ curve shown in figure 6.3. The slight misalignment of the layer normals with the velocity gradient direction is visible in the figure.

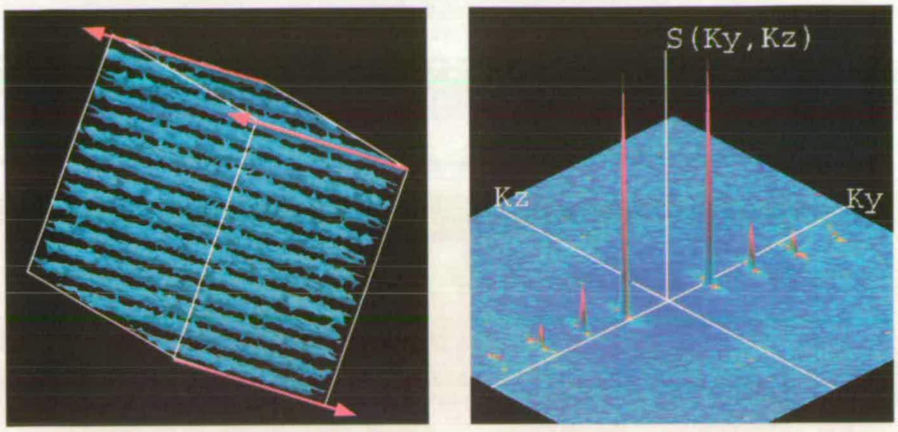

Figure 6.7: Left: A monodomain created by shearing the sample from the outset. Right: resulting angle-resolved structure factor $S(k_y, k_z)$ with y, z respectively the velocity gradient and neutral directions.

In the second T3D run, the effect of shear on a pre-existing lamellar texture was investigated. The bidomain structure already shown in figure 6.4(b) (but at the original quench temperature of $kT = 1.0$) was subjected to a shear rate of 0.04 in DPD units. By $t = 200$, this too was converted into a well-ordered monodomain sample, very similar to that shown in figure 6.7(a). As before, the layer normals must be perpendicular to the velocity gradient; however unlike figure 6.7(a) the layer normals were in this case oriented at roughly 35° between the velocity gradient and neutral directions. Figure 6.8 shows the real space structure and the angle resolved structure factor. The system is clearly lamellar, although the layers are not as well organised as in figure 6.7; if this system were run on longer it is believed that the layers would become more organised.

It was confirmed, in several smaller workstation runs, that formation of smectic and hexagonal mesophases proceeded rather quickly whenever a relatively small shear rate was maintained after the initial quench. This concurs with widespread experience in the processing of block copolymers, for example [95]. In some cases however, especially at higher shear rates, the structures formed are somewhat perturbed.

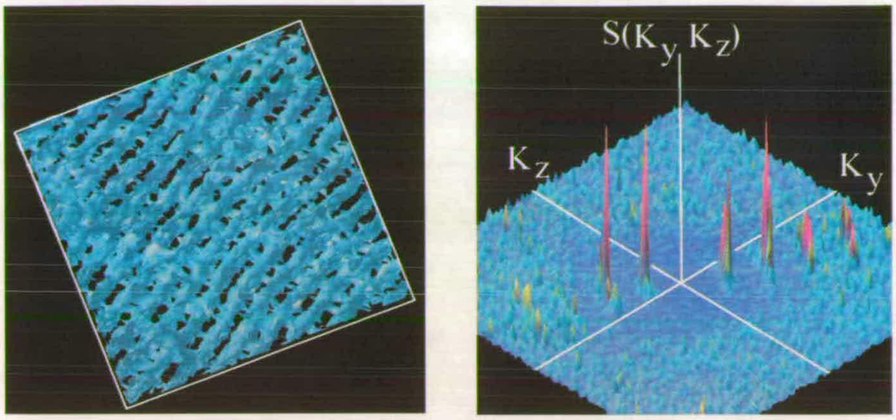

Figure 6.8: Left: A monodomain created by shearing the bidomain structure of figure 6.4, streamlines are coming out of the page. Right: resulting angle-resolved structure factor $S(k_y, k_z)$ with y, z respectively the velocity gradient and neutral directions.

In an additional simulation, a polydomain was sheared using a low shear rate, this was performed on the Cray with $N = 100\,000$. Here the volume fraction was $\phi = 0.6$, after 500 time units a polydomain (similar to figure 6.4(a)) had formed, this was then sheared for 700 time units at a shear rate of 0.01 forming a monodomain. With the shear switched off, the system was allowed to evolve for 1000 time units; even after such a long time period the monodomain remained intact. Although not conclusive, this represents good evidence that polydomains would like to become monodomains but are frustrated by the slow dynamics of defects.

6.5.1 Multilayer cylinders

It is known experimentally that, under sustained steady shear, a lamellar phase can develop an organized texture comprising concentric multilamellar polyhedra (the onion texture [96]) or, in thermotropics, long multilamellar prisms [97]. In practice these arise at very large length scales (microns) and therefore cannot really be expected in even the largest simulations performed here. However, in one simulation, evidence was seen that the system would like to develop a prism structure.

The parameters for this simulation were $\phi = 0.6$, $k_B T = 0.5$ and $N = 10^5$, inspection of figure 6.1 shows that these parameters are in the middle of the lamellar phase. After 550 time units the system organises itself into a polydomain structure (figure 6.9(a)), further evolution is then governed by the dynamics of defects and is thus very slow, it is expected that given unlimited time a single monodomain would form. Remember the system in figure 6.4 formed a similar structure at early times, this structure then re-organised itself into just two domains. Here a lower temperature was used, and so the ability of the system to remove defects through thermal agitation is reduced. In the absence of flow, one would not expect the system presently being considered to reorganise itself into a monodomain on observable timescales.

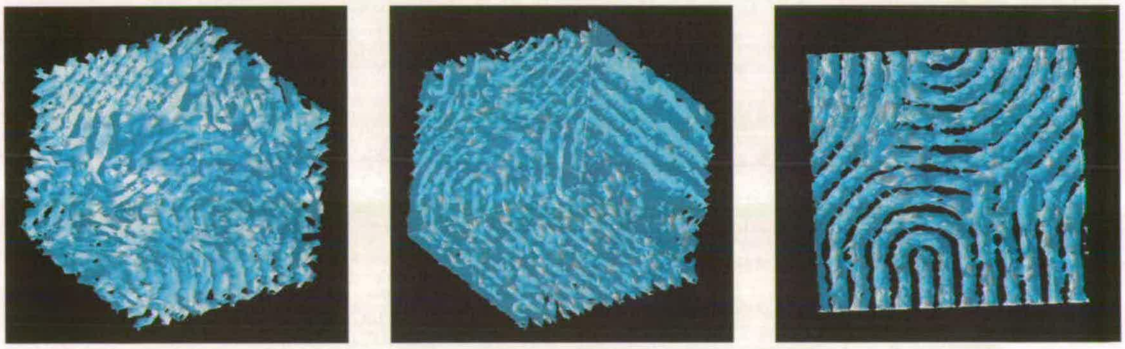

Figure 6.9: (a) After 550 time units the system has formed a polydomain structure. (b) Shearing the system for a further 650 time units gives a layered, tubular structure, the orientation of this picture is the same as in (a). (c) The same structure as (b), viewed *head on* with the streamlines running into the page.

Once the polydomain had formed, the system was sheared for a further 650 time units with shear rate $\dot{\gamma} = 0.04$. Figure 6.9(b) and (c) show the structure that was formed. The shear flow has had two effects; layers have been orientated and a curvature has been induced. The resulting configuration comprises a series of interlocking cylindrical layers. As in figure 6.7, the layer normals are perpendicular to the velocity gradient, this time they are also perpendicular to both the velocity direction and the velocity. If indeed the system is trying to form the multilamellar cylinders seen in experiment [97], figure 6.9 shows that only one cylinder can fit in the box. In figure 6.10, the periodic images have been placed side by side.

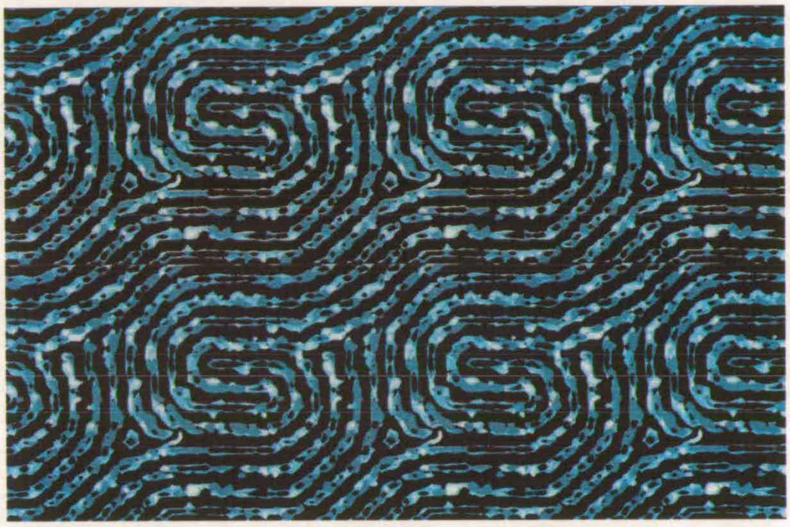

Figure 6.10: To construct this image, figure 6.9(c) has been tiled, the periodic images being placed next to one another.

Clearly the structure in figure 6.10 spans the periodic boundaries, and is certainly heavily affected by finite size effects[6]. Nevertheless, this is the first occasion that a simulation technique has been able to show the formation of such complicated structures. How the system forms these cylinders, and even why it would want to, is poorly understood. Simulation offers the unique opportunity of a close quarters examination of the mechanism by which these structures form. However, this is left for future work.

---

[6] Using the same code, it would be possible to double the system size ($\sim \times 10$ more particles). However, to gain quantitative results free from finite size effects the simulation would have to contain many cylinders, this would require a more powerful machine.

6.5.2 Helfrich buckling

A monodomain will organise itself such that the equilibrium distance between the layers, d_0, is constant for all layers. Upon increasing the temperature, one would expect the system to expand and the layer spacing to increase. Similarly decreasing the temperature will reduce d_0. If the temperature of a system with fixed volume is lowered, d can be decreased if the layers buckle [87]. This kind of response to a temperature change, first recognised by Helfrich in the context of liquid crystals [98], is shown schematically in figure 6.11.

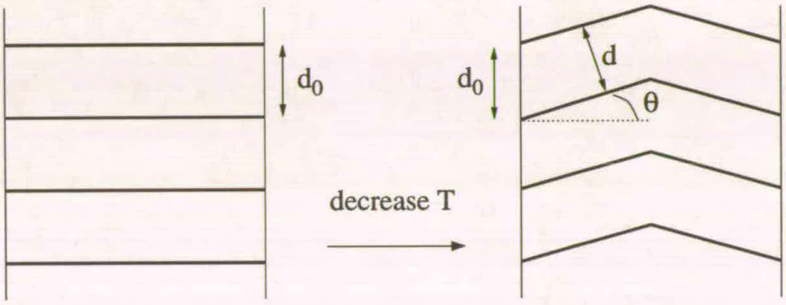

Figure 6.11: For a fixed volume and a fixed number of layers, the layer spacing, d, may be reduced if the layers buckle.

The new layer spacing is given by $d = d_0 \cos\theta$. Figure 6.12 shows the results of cooling two completely aligned configurations; the pictures are orientated looking perpendicular to the layer normals. In figure 6.12(a) the quench is from $kT = 1.5$ to $kT = 0.1$, in 6.12(b) it is from $kT = 1.5$ to $kT = 0.01$. In both systems a clear bend has developed at the lower temperature, consistent with the above argument. Using a ruler and a protractor the layer spacings before and after the quench, d_0 and d, were measured, along with the bend angle θ. In both cases there is a reduction in layer spacing, figure 6.12(a) has a reduction of $\sim 4\%$ and an associated $\theta \sim 21^o$, figure 6.12(b) has a change in layer spacing of $\sim 8\%$ and $\theta \sim 24^o$. Both of these are consistent with $d = d_0 \cos\theta$. Even though figure 6.12(b) represents a quench ten times lower than figure 6.12(a), the resulting bend is not significantly greater.

There are other mechanisms by which the system can respond to a decrease in the equilibrium layer spacing. Individual layers may elastically expand: compared to the energy required to bend a layer, the energy needed to expand each individual layer is large and this expansion is unstable to the buckling mechanism described above. If the number of layers present were to increase, the layer spacing would decrease. Nucleation of an extra layer requires amphiphiles to move at rightangles to the existing layers and *hop into* the spaces between. This process, known as permeation, will occur although not within the timescales of these simulations.

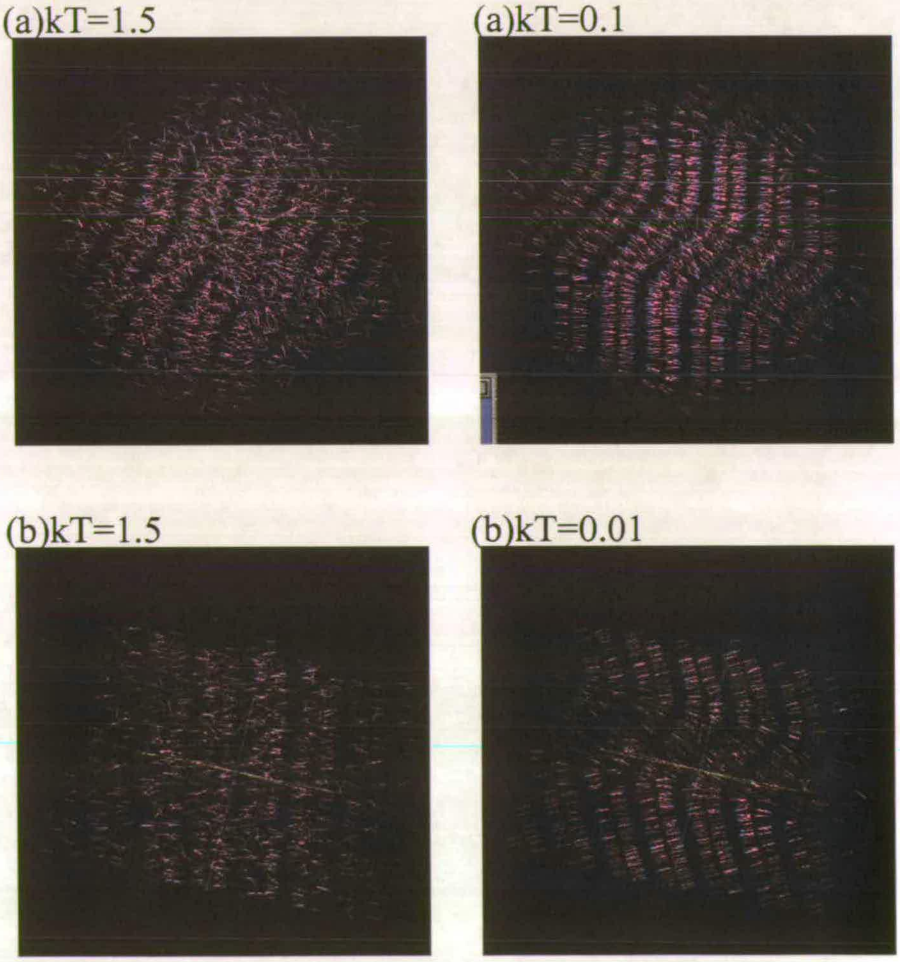

Figure 6.12: Individual dimers are plotted. In (a) and (b) a lamellar configuration is quenched and a distinct bend develops. The presence of the bend indicates that the equilibrium layer spacing has reduced due to the drop in temperature.

6.5.3 Effect of shear on the isotropic-to-lamellar phase boundary.

It has been demonstrated how, for suitable values of the control parameters kT and ϕ, a transition from an isotropic phase to a lamellar phase can be induced. In this section, the influence of a shear flow on this transition is examined. Experimental studies have shown a strong effect of shear; in some cases even gentle shaking of a test tube containing an isotropic phase induces a birefringent state, presumably lamellar, which persists for several seconds [99–103].

In an attempt to reproduce such behaviour, simulations were carried out wherein both the temperature and the shear rate were systematically varied. To allow a wider range of parameter variation a small system size was used, $N = 6000$ and $\rho = 6$, the thermodynamic parameters are the same as Section 6.5 and Section 6.3[7]. The surfactant concentration was constant throughout, $\phi = 0.7$. Figure 6.13 shows the amount of layering (measured as the height of the first peak of the radially averaged structure factor) within the system as a function of temperature for six different shear rates. At each shear rate, the temperature was lowered through the transition temperature and into the lamellar phase; the resulting (highly aligned) structure was then melted by increasing the temperature again. Each temperature was allowed to run for 200 time units. Since the isotropic to lamellar transition is a (weakly) first order transition [93, 104], the amount of alignment is expected to show a degree of hysteresis.

The transition temperature (T_c) for all but two of the shear rates is around $T_c = 1.55$, (shear rates of 0.3 and 0.4 gives T_c greater than this). These values are taken from the midpoint between the two branches of each curve. It should be noted that, at zero shear rate, T_c from figure 6.13 is lower than the value for T_c presented in the phase diagram figure 6.1. As stated in section 6.3, the Verlet integrator, used to produce the phase diagram, does not produce an accurate

---

[7] These simulations were performed as the Cray, as such they retain the Euler integrator.

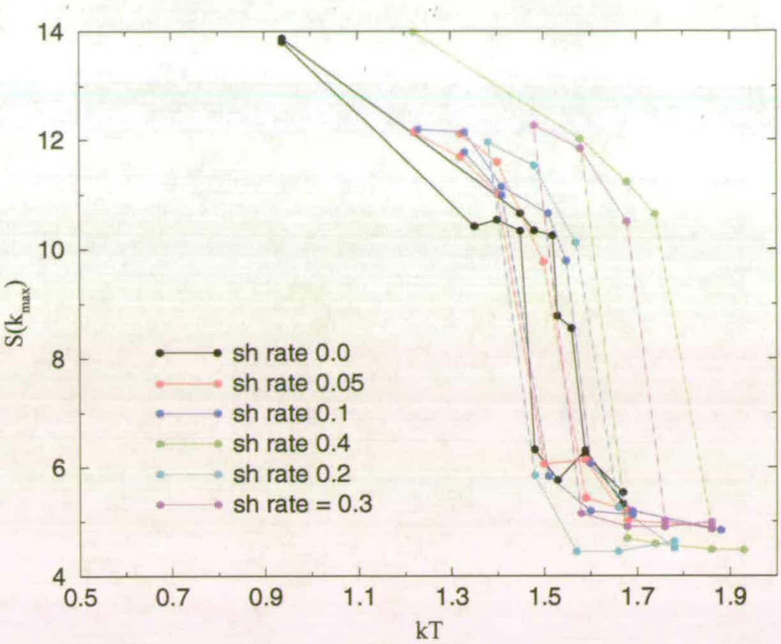

Figure 6.13: Hysteresis curves showing the effect of a shear flow on the ordering process. The maximum value of $S(k)$ is plotted as a function of temperature for six shear rates.

rotational temperature; this may be the cause.

A mean field analysis (which ignores fluctuations) predicts a second order transition, at a temperature T_c^{MFT} say. Incorporating fluctuations [104] into the theory, drives the transition first order and lowers the temperature of the transition to T_c^{FLUCT}; a consequence of first order transitions is the presence of hysteresis. When shear is added to the system, rotational symmetry is broken; fluctuations which would give rise to layering in directions inclined to the flow (in which lamellar order is prohibited) are eliminated. Thus the presence of shear suppresses fluctuations. At high enough shear rates, the suppression is great enough that the mean field result is recovered, causing reduced hysteresis and a higher transition temperature. Hence for $T_c^{MFT} < T < T_c^{FLUCT}$, the system is isotropic at low shear rate but lamellar at high shear rate—hence a shear-induced phase transition is predicted [93].

Figure 6.13 shows little discernible change in the value of T_c for the shear rates

0.05, 0.1 and 0.2, but for the two largest shear rate there is a definite increase in T_c as theory demands. However, at the higher shear rates the transition is still strongly first order, indeed the distance between the branches appears to have increased. Only for a shear rate of 0.05 is there any evidence of the branches coming closer. The failure to observe the expected lessening of hysteresis may be a consequence of a finite runtime. The points on figure 6.13 are assumed to be in (dynamic) equilibrium, this is a big assumption. It is quite possible that 200 time units is not long enough to achieve a steady state.

Chapter 7

Conclusion

There have been three main strands to this thesis: developing an extended parallel DPD code, testing the predictions of scaling analysis as applied to spinodal decomposition in a deeply quenched homogeneous binary fluid and exploring some of the properties of a simple DPD model of a surfactant solution. In this chapter, the conclusions from each of these threads will be drawn together.

The development of a scalable parallel code, capable of handling simulation sizes in excess of $N = 10^6$ has allowed us to access hydrodynamic regimes in three dimensional fluids. In the context of spinodal decomposition, viscous hydrodynamics leads to a linear growth law for domain size. A crucial prediction of the scaling analysis which yields this result is that the prefactor to linear growth must remain constant throughout the linear regime. The parallel code allowed a rigorous examination of these predictions. Linear growth was observed, however the prefactor was seen to drift systematically with increasing viscosity.

We have put forward four possible explanations for the drift of the prefactor. The first relies upon a huge crossover period, spanning 4 decades in reduced time[1], which has its own power law intermediate between viscous and inertial: this seems unlikely on two counts, one—crossovers are seldom so protracted, and two—all

---

[1] or two decades if the data of Lebowitz and Laradji proves to be unreliable

the fits performed here favoured a linear power with a drift in prefactor.

The second explanation assumes that statistical errors are to blame, this is always a possibility in any situation where measurements are performed on a thermodynamically small system. However, statistical errors are random in nature, it would be a rather large coincidence if they gave rise to the systematic variation seen here.

Thirdly, there is the possibility of a second, microscopic, lengthscale remaining important and influencing the growth at late stages. In the context of the data shown above this explanation is perhaps the most plausible, especially when one considers how little the separation between domain size L and interface width actually is.

Finally, the possibility that finite-size effects are influencing our data has to be acknowledged, but we cannot test this on the current machines.

The final block of work undertaken comprised a study of the behaviour of surfactant solutions; both with and without the presence of an external flow field. Simulating surfactant solutions in three dimensions is a challenge for any simulation technique. We have shown how the DPD algorithm produces a phase diagram containing several of the features seen in real systems; further, we have reproduced, for the first time in a simulation, realistic flow behaviour in lamellar systems. Given a larger machine, it will be possible to extend the work presented here. The formation of true multi-layer cylinders, the beginning of which was seen in section 6.5.1 should be well within reach; the closely related problem of onion formation may then be tackled. A small extension of the code used here would allow the inclusion of nonminimal amphiphiles, this opens the door to the study of relatively dilute surfactant solutions and/or ternary mixtures. Perhaps a more challenging use would be to study the physics of the interface between 100% surfactant 100% monomer interface. Experiments on such systems are producing unexpected and interesting results which are only poorly understood [105].

In conclusion it is the author's belief that to access physically interesting length and time scales in complex fluids, a mesoscopic modelling technique must be used. The DPD method has proved successful in reproducing meaningful behaviour on a scale not previously accessible to simulation. The off lattice nature of DPD combined with the relative ease with which new model features may be incorporated, should ensure DPD's status as one of the premier mesoscopic modelling techniques for the foreseeable future.

Appendix A

Structure factor

For a binary fluid, the difference between the densities of the two components may be used to define an order parameter ϕ. Defining $\rho_A(\mathbf{r},t)$ to be the local density of a single component at position $\mathbf{r}$ and at time t, the order parameter is written as $\phi(\mathbf{r},t) = \rho_A(\mathbf{r},t) - \rho_B(\mathbf{r},t)$. (Such expressions sometimes appear normalised by the total density $\rho_A(\mathbf{r},t) + \rho_B(\mathbf{r},t)$, doing this would not effect the lengthscale defined by equation (A.1).) Thus $\phi(\mathbf{r},t)$ is a scalar variable dependent on position and time; the value of ϕ indicates the degree of local separation.

Since the order parameter has been defined as a density difference, its Fourier transform is immediately identified as the quantity measured in light scattering experiments known as the structure factor. In such experiments, light is scattered off inhomogeneities in the refractive index, which, for a binary fluid system, are primarily caused by inhomogeneities in the density difference.

$$S(\mathbf{k}) = \langle [\rho_{\mathbf{A}}(\mathbf{k}) - \rho_{\mathbf{B}}(\mathbf{k})] \, [\rho_{\mathbf{A}}(-\mathbf{k}) - \rho_{\mathbf{B}}(-\mathbf{k})] \rangle$$

The value of the structure factor, $S(k_x, k_y, k_z)$, is proportional to the amount of mean-square density fluctuations having k-space components (k_x, k_y, k_z). For an isotropic structure, such as the network formed in spinodal decomposition, $S(\mathbf{k})$ will be radially symmetric, thus it may be radially averaged to give $S(k)$ without loss of information.

Lengthscales may be defined from the moments of $S(k)$, these lengthscales will be proportional to the size of structure within the system. Any moment will do, but for simplicity, and to allow comparison with other authors, the first moment is used here:

$$\begin{aligned} \langle k \rangle_{S(k)} &= \frac{\int k S(k) dk}{\int S(k) dk} \\ L(t) &= \frac{2\pi}{\langle k \rangle_{S(k)}} \end{aligned} \tag{A.1}$$

How does this lengthscale actually relate to the average domain size? A heuristic argument is given. Consider figure A.1; the system shown is completely separated so the average domain size is roughly $\Lambda/2$. But the order parameter varies with a wavelength Λ, thus $S(k)$ will be sharply peaked at k-vectors corresponding to Λ. So the actual length extracted is roughly equal to double the spatial extent of a single domain. In analysing the results for spinodal decomposition (Chapter 5), a finite size cutoff was imposed at $L \sim \Lambda/2$; data above this was discarded. In terms of the actual domain size, this amounts to a finite size cutoff equal to $\sim \Lambda/4$.

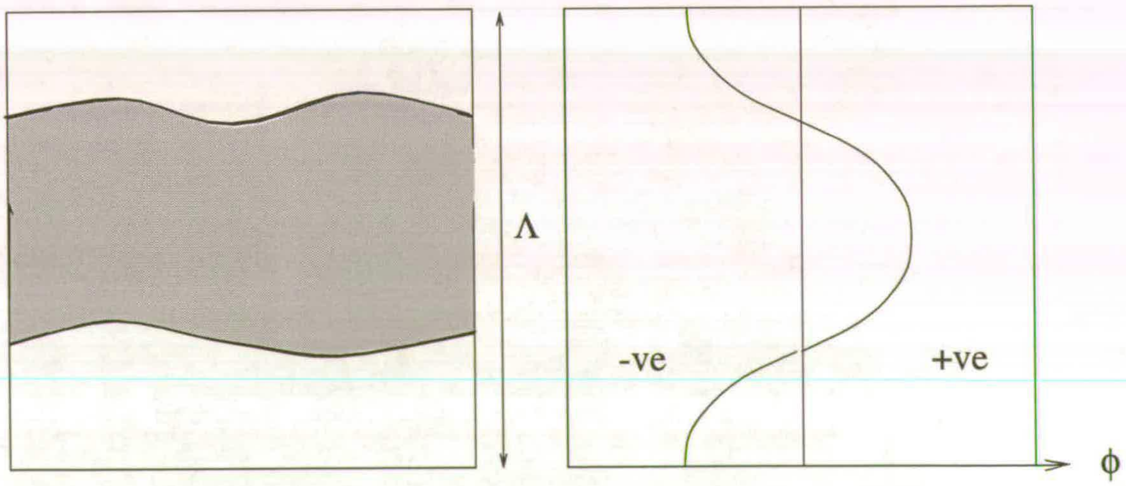

Figure A.1: When the system is completely separated the actual domain size is roughly $\Lambda/2$ (left), however the order parameter is correlated over distances of Λ (right).

Appendix B

Estimate of T_C using Mean Field Theory

Here, an expression for the free energy of a binary DPD fluid is derived using mean field theory. By considering the stability of the free energy, an upper bound on the critical temperature is found. An approximation to the actual free energy is,

$$F' = F_0 + \langle U - U_0 \rangle_0 \tag{B.1}$$

where F_0 is the free energy of a reference system, U is the actual energy of the DPD system and U_0 is the actual energy of the reference system, $\langle \ldots \rangle_0$ denotes an ensemble average over the reference system. (The Gibbs-Bogoliubov-Feynmann bound [106] tells us that the real free energy of the DPD system will always be less than or equal to F'.) Writing the average in equation (B.1) explicitly,

$$F' = F_0 + \frac{\int_{-\infty}^{\infty} da_1 \ldots da_{N_A} db_1 \ldots db_{N_B} \, (U - U_0) \exp[-\beta U_0]}{\int_{-\infty}^{\infty} da_1 \ldots da_{N_A} db_1 \ldots db_{N_B} \exp[-\beta U_0]} \tag{B.2}$$

the integral is over the position and velocity of every particle. (Equation (B.2) uses a compact notation in which the integration over the six components of position and velocity of a single type A particle is denoted by da_i.) N_A and N_B are the number of particles of type A and type B. The reference system is chosen to be the ideal gas, for which the kinetic energy contributions to $(U - U_0)$ cancel by equipartition; the only other contribution to $(U - U_0)$ comes from the DPD interactions,

$$U - U_0 = \sum_{ij} u_{ij}(r_{ij}). \tag{B.3}$$

Here $u_{ij} = u_{aa}$, u_{bb} or u_{ab} according to whether particles i,j are of type A or B. For every A particle there are $N_A - 1$ other A particles, so the number of BB and AA interactions is,

$$\begin{array}{ll} \dfrac{N_A(N_A-1)}{2} & \text{AA interactions} \\ \dfrac{N_B(N_B-1)}{2} & \text{BB interactions} \end{array}$$

in the same vein, the number of AB interactions is given by $N_A N_B$. Equation (B.2) may be expanded into terms containing interactions of a single type;

$$\begin{aligned} F' = F_0 \quad &+ \quad \frac{N_A(N_A-1)}{2Z_{MF}} \int \exp[-\beta U_0] u_{aa}(a_{12}) da_1 \ldots da_{N_A} db_1 \ldots db_{N_B} \\ &+ \quad \frac{N_B(N_B-1)}{2Z_{MF}} \int \exp[-\beta U_0] u_{bb}(b_{12}) da_1 \ldots da_{N_A} db_1 \ldots db_{N_B} \\ &+ \quad \frac{N_A N_B}{Z_{MF}} \int \exp[-\beta U_0] u_{ab}(a_1 - b_1) da_1 \ldots da_{N_A} db_1 \ldots db_{N_B} \end{aligned} \tag{B.4}$$

where a_{12} is equal to $a_1 - a_2$. Z_{MF} is the partition function of the reference system (given by the denominator of the second term on the right hand side of equation (B.2)). This, rather cumbersome equation, can be written in terms of a two particle joint probability distribution,

$\rho^{(1,1,N)}(a_1, b_1) \equiv$ probability of finding one A particle at a_1, one B particle at b_1

and so,

$$\rho^{(2,0,N)}(a_1, a_2) = N_A(N_A - 1) \frac{\int da_3 \ldots da_{N_A} db_1 \ldots db_{N_B} \exp[-\beta U_0]}{\int da_1 \ldots da_{N_A} db_1 \ldots db_{N_B} \exp[-\beta U_0]}$$

the prefactor $N_A(N_A - 1)$ corrects for indistinguishability. These may be normalised by dividing by the particle density, $\rho_A = N_A/V$;

$$g_{aa}(a_1, a_2) = \frac{\rho^{(2,0,N)}(a_1, a_2)}{\rho_A^2} \quad \text{and} \quad g_{ab}(a_1, b_1) = \frac{\rho^{(1,1,N)}(a_1, b_1)}{\rho_A \rho_B}.$$

Substituting for $\rho^{(2,0,N)}(a_1,a_2)$, $\rho^{(1,1,N)}(a_1,b_1)$ and $\rho^{(0,2,N)}(b_1,b_2)$ into equation (B.4) gives

$$\begin{aligned} F' = F_0 \quad &+ \quad \frac{1}{2}\rho_A^2 \int da_1 da_2 u_{aa}(a_1 - a_2) g_{aa}(a_1, a_2) \\ &+ \quad \frac{1}{2}\rho_B^2 \int db_1 db_2 u_{bb}(b_1 - b_2) g_{bb}(b_1, b_2) \\ &+ \quad \rho_A \rho_B \int da_1 db_1 u_{ab}(a_1 - b_1) g_{ab}(a_1, b_1). \end{aligned}$$

Now the ideal gas is introduced as the reference state. Defining, $x = N_A/N$, the free energy of an ideal gas is given by,

$$\frac{\beta F_0}{N} = \ln\rho - 1 + x\ln x + (1-x)\ln(1-x)$$

and so,

$$\begin{aligned} \frac{\beta F}{N} \leq \frac{\beta F'}{N} = \ln\rho - 1 + x\ln x \quad &+ \quad (1-x)\ln(1-x) \\ &+ \quad \frac{\rho}{2k_b T}\left[x^2 \int dr u_{aa}(r) g_{aa}(r)\right. \\ &+ \quad (1-x)^2 \int dr u_{bb}(r) g_{bb}(r) \\ &+ \quad \left. x(1-x)\int dr u_{ab}(r) g_{ab}(r)\right]. \end{aligned} \tag{B.5}$$

In an ideal gas $g_{aa} = g_{bb} = g_{ab} = 1$, and for a binary, symmetric DPD fluid the interactions are given by,

$$u_{aa} = u_{bb} = \frac{1}{2}\alpha_{AA}(1-r)^2, \qquad u_{ab} = \frac{1}{2}\alpha_{AB}(1-r)^2.$$

Performing the integrations in equation (B.5) gives an approximation to the DPD free energy,

$$\begin{aligned} f = \frac{\beta F'}{N} = \quad &\ln \quad \rho - 1 + x\ln x + (1-x)\ln(1-x) \\ &+ \quad \frac{\rho}{2k_B T}\left[x^2\alpha_{AA}\frac{2\pi}{30} + (1-x)^2\alpha_{BB}\frac{2\pi}{30} + 2x(1-x)\alpha_{AB}\frac{2\pi}{30}\right] \end{aligned}$$

Recalling the discussion in section 1 of Chapter 3, the system will be stable if the second derivative of f is positive,

$$\frac{\partial^2 f}{\partial x^2} = \frac{1}{x} + \frac{1}{1-x} + \frac{\rho}{2k_B T}\left[\alpha_{AA}\frac{4\pi}{30} + \alpha_{BB}\frac{4\pi}{30} - \alpha_{AB}\frac{8\pi}{30}\right] \tag{B.6}$$

with the critical point occurring at $\partial^2 f/\partial x^2 = \partial f/\partial x = 0$. By symmetry x may be set to 1/2, which gives the final expression for the critical temperature.

$$\begin{aligned} 1 &= \frac{2\rho}{k_B T_c} x(1-x)\frac{2\pi}{30}\left[\alpha_{AB} - \alpha_{AA}\right] && \text{(B.7)} \\ \Rightarrow k_B T_c &= \rho x(1-x)\frac{4\pi}{30}\left[\alpha_{AB} - \alpha_{AA}\right]. && \text{(B.8)} \end{aligned}$$

$$\boxed{k_B T_c = \frac{\rho\pi}{30}\left(\alpha_{AB} - \alpha_{AA}\right)}$$

Appendix C

Early time Cahn-Hilliard behaviour

At the earliest stages of separation, before even the diffusive regime, the evolution is described by linearised Cahn-Hilliard theory, eq(2.13). As stated in chapter 3, Cahn-Hilliard theory makes the assumption that the separation can be treated as a perturbation about the homogeneous state. It can therefore only ever be accurate at the very earliest times. In only one simulation was Cahn-Hilliard like behaviour directly observed, see figure C.1. This simulation had a low viscosity $\eta = 3.0$, a low density $\rho = 3$ and a very low surface tension $\sigma = 0.75$, (the repulsion parameters are $AA = 25$, $AB = 32$). With such a small repulsion between species, all the separation processes are slowed down; all other simulations have a much greater tendency to separate and the Cahn-Hilliard regime is over before it can be seen.

Reproducing Cahn-Hilliard behaviour is reassuring, in that it shows the DPD model is qualitatively correct at early times. However it reveals nothing about the late time hydrodynamic regimes and adds nothing to the analysis of Chapters 4 and 5.

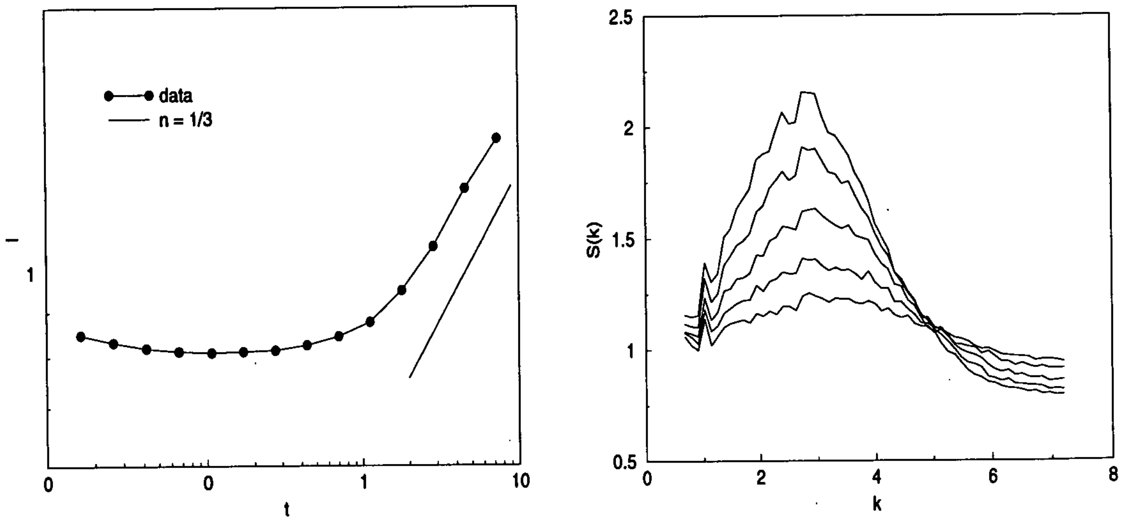

Figure C.1: Early time Cahn-Hilliard type behaviour.

Appendix D

Code Extracts

In total the code comprises 7225 lines of code, of this about 25% is related to message passing between processors. The major differences between a parallel DPD code and a parallel MD code arise due to the presence of a random term in the DPD force. An extract from the code is presented here, it is hoped this will shed light on the random force problem and how it is resolved. Also contained here are a few of the aspects relating to implementation of Lees Edwards sliding boundary conditions.

A single timestep has the following structure;

- increment timestep counter
- call plcfor
- integrate forces to update velocities and positions
- modify forces according to constraints (dimers only)
- calculate and output observables

The subroutine **`plcfor()`** is called once per timestep, its main function is to control the communications neccessary to calculate the correct force, in addition it also calls the routine which sets up the linked lists. We will proceed by breaking the routine into three sections, (lines preceded by *** are comments).

```
      subroutine plcfor()
      include 'type.inc'

***Exchange particle data in -/+ y directions.
***nbeads is the number of particles stored on this processor
***nlimit = nbeads plus particles in the halo, nlimit increases with
***each boundary exchange.
***Lees Edwards boundary conditions for upper and lower processor slabs.
      nlimit=nbeads
      if (idy.eq.0) then
         call Lees_Edwards_Lower1(nlimit,1,nbeads)
      elseif (idy.eq.npy-1) then
         call Lees_Edwards_Upper1(nlimit,1,nbeads)
      else
         begin=0.d0
         final=rcut
         call export(nlimit,2,map(3),begin,final, sidey)
         begin=sidey-rcut
         final=sidey
         call export(nlimit,2,map(4),begin,final,-sidey)
      end if

***Exchange particle data in -/+ x directions.
      begin=0.d0
      final=rcut
      call export(nlimit,1,map(1),begin,final, sidex)
      begin=sidex-rcut
      final=sidex
      call export(nlimit,1,map(2),begin,final,-sidex)

***Exchange particle data in -/+ z directions.
      begin=0.d0
      final=rcut
      call export(nlimit,3,map(5),begin,final, sidez)
```

```
      begin=sidez-rcut
      final=sidez
      call export(nlimit,3,map(6),begin,final,-sidez)
```

All the type declarations are included in `type.inc`, parameters are passed by means of common blocks, these would normally appear immediately after the `include` statement, but have been omitted for clarity.

An initial set of communication routines sets up the halos around each processor, these halos are exactly one interaction radius thick and ensure each processor has enough information to perform the force calculation. Routines `Lees-Edwards-Lower1()` and `Lees-Edwards-Upper1()` are called by processors in the lower and upper slabs only (lower and upper as measured in the shear gradient direction); these processors are passing particles over the sheared boundaries, thus the communication routines have the additional task of calculating which processors to communicate with. Note that, in addition to communicating with each other, the upper and lower slabs must also communicate with processors in the *bulk* of the domain. To avoid deadlock, all communications are *blocking*; which means for every send and receive operation, execution on both processors will not proceed until the communication is successfully completed. Now the linked lists and forces may be calculated:

```
***Construct linked lists.
      call parlnk(1,nlimit,rcut,sidex,sidey,sidez,
     &            lct,link,xxx,yyy,zzz)

***Calculate pair forces.
      call DPD_forces()

***Calculate the inverse lab(), to identification of particles.
      do i=1,nlimit
 if(lab(i).ne.0) then
   ilab(lab(i)) = i
 else
```

```
  ilab(lab(i)) = 0
end if
      end do
      call barrier()
```

Calculating `ilab()` greatly speeds up the second round of communications. In this second round, the random component of the DPD force will be sent back *per particle*, it is essential that this component is added to the correct particle. `ilab()` identifies the position of individual particles within the processors local array, thus a search for the correct particle can be avoided. In the final section of code the random forces are returned.

```
***Now transfer the random forces.
***Second exchanges must be done in reverse order or the receiving processor
***will not recognise the incoming particle. Transfer_flag() is the
***additional boolean neccessary to avoid sending the same particle twice
***(see text).
***nlimit is now decreasing with each exchange.
***Exchange particle data in -/+ z directions.
      do i = 1, nlimit
         transfer_flag(i) = .FALSE.
      enddo
      begin=-rcut
      final=0.d0
      call DPD_export2(nlimit,3,map(5),begin,final,nbeads)
      begin=sidez
      final=sidez+rcut
      call DPD_export2(nlimit,3,map(6),begin,final,nbeads)

***Exchange particle data in -/+ x directions.
      begin=-rcut
      final=0.d0
      call DPD_export2(nlimit,1,map(1),begin,final,nbeads)
      begin=sidex
      final=sidex+rcut
      call DPD_export2(nlimit,1,map(2),begin,final,nbeads)
```

```
***Exchange particle data in -/+ y directions.
***Note these are the same routines used in the first exchange, but a control
***flag (the second argument) is changed.
      if(idy.eq.npy-1) then
         call Lees_Edwards_Upper1(nlimit,0,nbeads)
      elseif(idy.eq.0) then
         call Lees_Edwards_Lower1(nlimit,0,nbeads)
      else
         begin=-rcut
         final=0.d0
         call DPD_export2(nlimit,2,map(3),begin,final,nbeads)
         begin=sidey
         final=sidey+rcut
         call DPD_export2(nlimit,2,map(4),begin,final,nbeads)
      end if

***Add the random component onto the other forces (nbeads is the number of
***particles stored on this processor).
      do i=1,nbeads
         fxx(i) = fxx(i) + D_fxx(i)
         fyy(i) = fyy(i) + D_fyy(i)
         fzz(i) = fzz(i) + D_fzz(i)
      end do

      return
      end
```

Here the random components have been successfully returned to the correct processor and added to the other forces. A subtlety arises with the Lees Edwards boundary conditions: in the shear velocity (x)-direction processor domains no longer line up exactly, this creates the possibility for particles which lie on the edge of domains to be passed back to the correct processor, but by two different routes. This would result in the random force being calculated twice, and an error. Figure D.1 illustrates the problem. A boolean variable, `transfer-flag()`, is

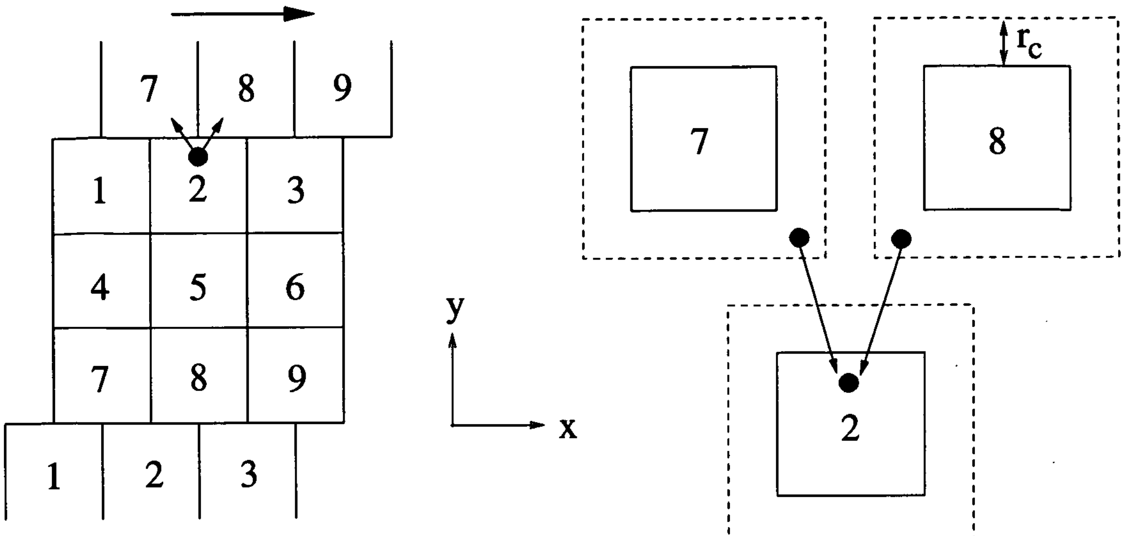

Figure D.1: Left: (a) the domain decomposition, with shear, the marked particle will be transferred over the sheared boundaries to lie in the halos of processors 7 and 8. Right: (b) when the random forces are passed back, unless precautions are taken, both 7 and 8 will send the particle back to processor 2.

used to solve this problem: particle `i` is only transferred over the sheared boundaries if `transfer-flag(i)` is `.FALSE.`, once a particle has been transferred over processors in the shear velocity direction (the x-direction), `transfer-flag(i)` is set to `.TRUE.`.[1]

---

[1] In the z-direction, processor domains always remain perfectly aligned and the problem does not occur.

Bibliography

[1] S.I. Jury, P. Bladon, S. Krishna, and M.E. Cates. *Phys. Rev. E.*, 59, 1999.

[2] S.I. Jury, P. Bladon, M.E. Cates, S. Krishna, M.J. Haagen, J.N. Ruddock, and P.B. Warren. *PCCP*, 1(9), 1999.

[3] R.G. Larson. *J. Physique II*, 6:1441, 1996.

[4] J.M. Seddon. *Biochim. Biophys. Acta.*, 1:1031, 1990.

[5] J-F. Berret, D.C. Roux, G. Porte, and P. Lindner. *Europhys. Lett.*, 32:137, 1995.

[6] D. Sappelt and J. Jackle. *Europhys. Letts.*, 37:13, 1997.

[7] A. Chakrabarti, R. Toral, and J.D. Gunton. *Phys. Rev. B*, 39:4386, 1989.

[8] E.T. Gawlinski, J. Vinals, and J.D. Gunton. *Phys. Rev. B*, 39:7266, 1989.

[9] J.E. Farrel and O.T. Valls. *Phys. Rev. B*, 43:630, 1991.

[10] O.T. Valls and J.E. Farrell. *Phys. Rev. E*, 47:R36, 1993.

[11] Y. Wu, F.J. Alexander, T. Lookman, and S. Chen. *Phys. Rev. Letts.*, 74:3852, 1995.

[12] Y. Lookman, T.and Wu, F.J. Alexander, and S. Chen. *Phys. Rev. E*, 53:5513, 1996.

[13] J. Olson and D.H. Rothman. *J. Stat. Phys.*, 52:1119, 1988.

[14] C. Appert, J.F. Olson, D.H. Rothman, and S. Zaleski. *J. Stat. Phys.*, 81:181, 1995.

[15] S. Bastea and J.E. Lebowitz. *Phys. Rev. E*, 52:3821, 1995.

[16] A.N. Emerton, P.V. Coveney, and B.M. Boghosian. *Phys. Rev. E.*, 55:708, 1997.

[17] A.N. Emerton, F.J. Weig, P.V. Coveney, and B.M. Boghosian. *J. Phys. Cond. Mat.*, 9:8893, 1997.

[18] F.J. Weig, P.V. Coveney, and B.M. Boghosian. *Phys. Rev. E.*, 56:6877, 1997.

[19] F.J. Higuera, S. Succi, and R. Benzi. *Europhys. Lett.*, 9:345, 1989.

[20] A.K. Gunstensen, D.H. Rothman, S. Zaleski, and G. Zanetti. *Phys. Rev. A*, 43:4320, 1991.

[21] A.J. Wagner and J.M. Yeomans. *Phys. Rev. Lett.*, 80:1429, 1998.

[22] A.J. Wagner and J.M. Yeomans. *Int. J. Mod. Phys. C*, 1998. recieved July 1998.

[23] E. Osborn, W.R.and Orlandini, M.R. Swift, J.M. Yeomans, and J.R. Banavar. *Phys. Rev. Lett.*, 75:4031, 1995.

[24] M.R. Swift, E. Orlandini, W.R. Osborn, and J.M. Yeomans. *Phys. Rev. E*, 54, 1996.

[25] F.J. Alexander, S. Chen, and D.W. Grunau. *Phys. Rev. B*, 48:634, 1993.

[26] V. Kendon, P. Bladon, J-C. Desplat, and M.E. Cates. *cond/mat*, 1999. http://xxx.soton.ac.uk/abs/cond-mat/9902346.

[27] S. Chen and T. Lookman. *J. Stat. Phys.*, 81:223, 1995.

[28] O. Theissen, G Gomper, and D.M.. Kroll. *Europhys. Letts.*, 42:419, 1998.

[29] W.T. Tai and D.K.P Yue. *Ann. Rev. Fluid Mech*, 28:249, 1996.

[30] M. Tjahjadi, H.A. Stone, and J.M. Ottino. *J. Fluid Mech*, 232:191, 1991.

[31] M.P. Allen and D.J. Tildesley. *Computer Simulation of Liquids.* Clarendon, Oxford, 1987.

[32] E. Velasco and S. Toxvaerd. *J. Condens. Matt.*, 6:A205, 1994.

[33] W. Ma, A. Maritan, J.R. Banavar, and J. Koplik. *Phys. Rev. A*, 45:R5347, 1992.

[34] M. Laradji, S. Toxvaerd, and O.G. Mouritsen. *Phys. Rev. Lett.*, 77:2253, 1996.

[35] P. Español and P.B. Warren. *Europhys. Lett.*, 30:191, 1995.

[36] R.D. Groot and P.B. Warren. *J. Chem. Phys.*, 170:4423, 1997.

[37] C.A. Marsh. *Theoretical Aspects of Dissipative Particle Dynamics.* PhD thesis, Univeristy of Oxford, 1998.

[38] P.V. Coveney and P. Español. *J. Phys. A.*, 30:779, 1997.

[39] P.V. Coveney and K.E. Novik. *Phys. Rev. E*, 54:5134, 1996.

[40] P.V. Coveney and K.E. Novik. *Phys. Rev. E*, 55:3124, 1997.

[41] E.S. Boek, P.V. Coveney, and H.N.W. Lekkerkerker. *J. Phys. Cond. Mat.*, 8:9509, 1996.

[42] E.S. Boek, P.V. Coveney, H.N.W. Lekkerkerker, and P.V.D. Schoot. *Phys. Rev. E*, 55:3124, 1997.

[43] P.J. Hoogerbrugge and J.M.V.A. Koelman. *Europhys. Lett.*, 19:155, 1992.

[44] K.E Novik and P.V.. Coveney. *J. Chem. Phys.*, 109:7667, 1998.

[45] D.J. Tritton. *Physical Fluid Dynamics.* Clarendon Press, Oxford, second edition, 1988.

[46] A.W. Lees and S.F. Edwards. *J. Phys. Chem.*, 5:1921, 1972.

[47] M. Parrinello and A. Rahman. *J. Chem. Phys.*, 80:860, 1982.

[48] C.A. Marsh, G. Backx, and M.H. Ernst. *Phys. Rev. E*, 56:1676, 1997.

[49] C.A. Marsh, G. Backx, and M.H. Ernst. *Europhys. Lett.*, 38:411, 1997.

[50] V.I. Gorentsveig, P. Fratzl, and J.L. Lebowitz. *Phys. Rev. B Cond. Mat.*, 55:2912, 1997.

[51] H.E. Cook. *Acta Metall.*, 18:297, 1970.

[52] J.S. Langer, M. Bar-on, and H.D. Miller. *Phys. Rev. A*, 11:1417, 1975.

[53] K. Kawasaki and T. Ohta. *Prog. Theor. Phys.*, 59:362, 1978.

[54] H. Furukawa. *Adv. Phys.*, 43:357, 1994.

[55] K. Binder and D. Stauffer. *Phys. Rev. Lett.*, 33:1006, 1974.

[56] G.F. Mazenko. *Phys. Rev. Lett.*, 63:1605, 1989.

[57] G.F. Mazenko. *Phys. Rev. B*, 42:4487, 1990.

[58] G.F. Mazenko. *Phys. Rev. B*, 43:5747, 1991.

[59] A.J. Bray. *Adv. Phys.*, 43:357, 1994.

[60] I.M. Lifshitz and V.V. Slyozov. *Phys. Chem. Solids*, 19:35, 1961.

[61] C. Wagner. *Z. Elektrochem.*, 65:581, 1961.

[62] D. Stauffer and A. Aharony. *Introduction to percolation theory.* Taylor and Francis, London, 1994.

[63] M von Smoluchowski. *Z. Phys. Chem.*, 92:129, 1917.

[64] E.D. Siggia. *Phys. Rev. A.*, 20:595, 1979.

[65] B.R. Manson, D.F. Young, and T.H. Okiishi. *Fundamentals of Fluid Mechanics.* John Wiley and Sons Inc., New York, 1990.

[66] A. Schiller. In *Proc. 3rd Int. Congress for Applied Mechanics*, volume 1, page 226, Stockholm, 1930.

[67] O. Reynolds. *Phil. Trans. R. Soc. London*, 174:935, 1883.

[68] V.C. Patel and M.R. Head. *J. Fluid Mech.*, 38:181, 1969.

[69] M. Grant and K.R. Elder. *Phys. Rev. Lett.*, 82:14, 1999.

[70] H. Furukawa. *J. of Phys. Soc. of Jap.*, 58:216, 1989.

[71] K. Kubota, N. Kuwahara, H Eda, and M. Sakazume. *Phys. Rev. A*, 45:R3377, 1992.

[72] T Hashimoto. *Physica A*, 214:261, 1994.

[73] F.S. Bates. *J. Chem Phys*, 91:3258, 1989.

[74] S.H. Chen, D. Lombardo, F. Mallamace, N. Micali, S. Trusso, and C. Vasi. *Progr. Colloid Polym. Sci.*, 93:311, 1993.

[75] C. Nash and S. Sen. *Topology and Geometry for Physicists.* Academic Press, London, 1992.

[76] T. Koga and K. Kawasaki. *Phys. Rev. A*, 44:R817, 1991.

[77] S. Puri and B. Dünweg. *Phys. Rev. A*, 45:R6977, 1992.

[78] A. Shinozaki and Y. Oono. *Phys. Rev. Lett.*, 66:173, 1991.

[79] S. Bastea and J.L. Lebowitz. *Phys. Rev. Lett.*, 78:3499, 1997.

[80] W.H. Press, S.A. Teukolsky, W.T. Vetterling, and B.P. Flannery. *Numerical Recipes.* Cambridge university Press, 1993.

[81] J. Kurchan and L. Latoux. *J. Phys. A*, 29:1929, 1996.

[82] J. Eggers. *Rev. Mod. Phys.*, 69:865, 1997.

[83] J. Eggers. *Phys. Rev. Lett.*, 71:3458, 1993.

[84] R.G. Larson and P.T. Mather. In T.C.B. McLeish, editor, *Theoretical Challenges in the Dynamics of Complex Fluids*, volume 339. Kluwer, 1997.

[85] G Gompper and M. Schick. *Self-Assembling Amphiphilic Systems.* Academic Press, New York, 1994.

[86] B. Smit, K. Esselink, P.A.J. Hilbers, N.M. van Os, and I. Szleifer. *Langmuir*, 9:9, 1993.

[87] P.G. de Gennes and J. Prost. *The Physics of Liquid Crystals.* Oxford, 1993.

[88] F. Nallet, D. Roux, and J. Prost. *J. Physique*, 50:3147, 1989.

[89] R.D. Groot and T.J. Madden. *J. Chem. Phys.*, 108:875, 1998.

[90] W. Schroeder, K. Martin, and B. Lorensen. *The Visualisation Toolkit.* Prentice Hall, 1996.

[91] D.J. Mitchell, G.J.T. Tiddy, L. Waring, T. Bostock, and M.P. McDonald. *J. Chem. Soc. Faraday Trans. 1*, 79:975, 1983.

[92] R.G. Laughlin. *The Aqueous Phase Behaviour of Surfactants.* Academic Press, New York, 1994.

[93] M.E. Cates and S.T. Milner. *Phys. Rev. Lett.*, 62:1856, 1989.

[94] C.R. Safinya and R.F. Bruinsma. *Phys. Rev. A*, 43:5377, 1991.

[95] G.H. Fredrickson and F.S. Bates. *Ann. Rev. Mater. Sci.*, 26:501, 1996.

[96] O. Diat, D. Roux, and F. Nallet. *J. Physique II*, 3:1427, 1993.

[97] P. Panizza, P. Archambault, and D. Roux. *J. Physique II*, 5:303, 1995.

[98] W. Helfrich. *Appl. Phys. Lett.*, 17:531, 1970.

[99] D. Roux. *Phys. Rev. Lett.*, 60:363, 1988.

[100] R.G. Laughlin. In G.H. Brown, editor, *Advances in Liquid Crystals.* New York, 1978.

[101] C.R. Safinya, D. Roux, G.S. Smith, S.K. Sinha, P. Dimon, N.A. Clark, and A.M. Bellocq. *Phys. Rev. Lett.*, 57:2718, 1987.

[102] J.C. Lang and R.D. Morgan. *J. Chem. Phys.*, 73:5849, 1980.

[103] M.E. Cates, D. Roux, D. Andelman, S.T. Milner, and S.A. Safran. *Europhys. Lett.*, 5:733, 1988.

[104] S. Brazovskii. *Zh. Eksp. Teor. Fiz.*, 68:175, 1975.

[105] M. Buchanan, J. Arrault, and M.E. Cates. *Langmuir*, 14:7371, 1998.

[106] R.P. Feynman. *Lectures in Statistical Physics.* Reading Mass., 1972.

Acknowledgements

I would like to thank my two supervisors Peter Bladon and Mike Cates; without their help none of this would have been possible. Thanks also to Stuart Pawley for persuading me this was a worthwhile project in the first place.

I have enjoyed two visits to the Port Sunlight laboratories of Unilever, thanks to Patrick Warren for hospitality during these visits and for many useful discussions. Thanks also to Noel Ruddock for help with debugging the code and to Marten Hagen for collaboration with the surfactants chapter.

This work has been funded by an EPSRC studentship, I also greatfully acknowledge the CASE award from Unilever research (UK).

Thanks to all the boys and girls of the condensed matter group. I have enjoyed my time as a Phd student, I thank you all for creating the relaxed and friendly atmosphere which exists within the group. May I wish the best of luck to the E=M.C.C.; I look forward to donning the shirt with pride for many years to come.

A warm smile and a big kiss to Kerstin, for making life fun.

Finally, my parents—for their continuing support in all the half-witted ventures I've embarked upon over the years. Some day (soon?) I'll take you out for a curry!